Probabilistic Markov Chain Model of Photonic Crystal Surface Emitting Lasers

Jingzhao Liu

James Watt School of Engineering

College of Science and Engineering

University of Glasgow

Submitted in fulfilment of requirements for the degree of Doctor of Philosophy (Ph.D.)

Dec 2025

Abstract

Semiconductor lasers face a fundamental trade-off between high output power and high-quality single-lobe beams. Photonic crystal surface-emitting lasers (PCSELs) have emerged as a promising platform that overcomes this limitation by enabling scalable, single-mode, vertical emission. However, their design is hindered by complex interactions between microscopic scattering and macroscopic losses—especially in-plane loss ($\alpha_{//}$), which is critical yet difficult to measure experimentally.

This thesis introduces a computationally efficient Probabilistic Markov Chain (PMC) model to bridge microscopic physics and device performance. By treating light propagation as a stochastic process, the model translates coupling coefficients into directional scattering probabilities, enabling rapid simulation of finite-sized PCSELs without directly solving Maxwell's equations.

The PMC model is quantitatively and qualitatively validated by predicting the performance (e.g. loss, slope efficiency and near-field pattern) of PCSEL devices (GaN-based PCSEL, GaAs-based PCSEL and InP-based PCSEL) from references and against experimental PCSEL and resonator-embedded PCSEL (REPCSEL) data. The predicted result has excellent agreements (e.g. < 1 cm^{-1} difference in loss) with those reported in references and experimental. Through parametric studies, it quantifies the impact of in-plane coupling and integrated mirrors on $\alpha_{//}$ and mode control. Furthermore, the model reveals an interdependence between in-plane and internal loss in designs with unpumped boundaries, challenging conventional design assumptions. Finally, three novel high-efficiency PCSEL architectures are proposed and evaluated—incorporating butt-coupled passive sections, selective area intermixing, and dual contacts—to minimize parasitic losses and maximize power conversion efficiency.

In summary, this work establishes the PMC model as a versatile design tool that provides fundamental insight into PCSEL loss mechanisms and opens new pathways toward high-performance, scalable semiconductor lasers.

Acknowledgment

The completion of this doctoral dissertation would not have been possible without the support, guidance, and encouragement of many individuals to whom I wish to express my deepest gratitude.

First and foremost, I offer my sincerest gratitude to my supervisors, Professor Richard Hogg and Professor Stephen Sweeney. I have been extraordinarily fortunate to have two mentors who not only provided me with brilliant academic guidance but also fostered a supportive and stimulating research environment. Professor Hogg's profound insight and unwavering commitment to scientific excellence have been a constant source of inspiration. His meticulous attention to detail and invaluable feedback have profoundly shaped this work. I am equally indebted to Professor Sweeney for his endless patience, immense knowledge, and steadfast encouragement during the most challenging phases of my research. His optimistic outlook and sage advice kept me motivated and focused. I could not have imagined having better advisors and mentors for my PhD study.

My heartfelt thanks also go to all my colleagues and lab mates at the University of Glasgow. Our stimulating discussions, both academic and casual, have made this journey enjoyable and memorable. I am particularly grateful to Mr Xingyu Zhao, Dr Zijun Bian, Mr Connor Munro, Dr Aye Su Mon Kyaw, and Dr Danqi Lei for their collaboration, shared wisdom, and the camaraderie that turned our workspace into a second home. A special note of thanks is due to the senior members of our group, Dr Daehyun Kim, Dr Adam McKenzie, Dr Katherine Rae, Dr Ben King, Dr Dominic Duffy, and Dr Igor Marko, whose pioneering work laid the foundation for my research and who were always generous with their time and expertise.

Finally, and most importantly, I wish to express my profound appreciation to my family. To my parents, Zhihe Liu and Xiaoping Geng, thank you for your unconditional love, endless sacrifices, and for instilling in me the values of perseverance and education. Your unwavering belief in me has been my greatest strength.

This thesis is as much a result of their collective contributions as it is of my own efforts.

Contents

List of figures

List of Publications

[1]. **J. Liu**, X. Zhao, D. Kim, J. R. Orchard, D. T. D. Childs, R. J. E. Taylor, P. Harvey, S. J. Sweeney and R. A. Hogg, "Exploring high efficiency PCSELs using probabilistic Markov chain model" Nov 2025 submitted to IEEE JSTQE.

[2]. X. Zhao, **J. Liu**, Z. Bian, K. Ben D. Kim, S. J. S. Sweeney, and R. A. Hogg, "Spatially Resolved Band-Structure for the Quantitative Analysis of PCSELs" Dec 2025 submitted to IEEE JSTQE.

[3]. **J. Liu**, X. Zhao, Z. Bian, P. Harvey, S. Watson, S. J. Sweeney, and R. A. Hogg, "Interdependence of parasitic losses in photonic crystal surface emitting lasers," *AIP Advances*, vol. 15, no. 4, p. 045321, Apr. 2025, doi: 10.1063/5.0252646.

[4]. Z. Bian, X. Zhao, **J. Liu** *et al.*, "Resonator embedded photonic crystal surface emitting lasers," *npj Nanophoton.*, vol. 1, p. 13, 2024, doi: 10.31038/s44310-024-00014-9.

[5]. **J. Liu**, Y. Gao, P. Ivanov, P. Harvey, and R. Hogg, "Probabilistic Markov chain modeling of photonic crystal surface emitting lasers," *Appl. Phys. Lett.*, vol. 123, no. 26, p. 261107, Dec. 2023, doi: 10.1063/5.0168073.

Conference Presentations and Posters

Presentations

[1]. **J. Liu**, Z. Bian, X. Zhao, S. J. Sweeney, and R. A. Hogg, "Optimization of pumping geometry of photonic crystal surface emitting lasers," in *Proc. SPIE Phys. Simul. Optoelectron. Devices XXXIII*, vol. 13360, Mar. 2025, Art. no. 1336004, doi: 10.1117/12.3042883.

[2]. **J. Liu**, D. Kim, Z. Bian, J. Feng, Y. Gao, and R. A. Hogg, "Convergence criteria for Markov chain modelling of photonic crystal surface emitting lasers," in *Proc. SPIE Photonics West*, 2023, doi: 10.1117/12.2649077.

[3]. X. Y. Zhao, A. F. McKenzie, C. W. Munro, S. L. Bayliss, K. J. Rae, D.-H. Kim, D. A. MacLaren, R. A. Hogg, and **J. Liu**, "2D selective area growth for photonic crystal surface emitting lasers," in *Proc. SPIE Novel In-Plane Semiconductor Lasers XXII*, vol. PC12440, Mar. 2023, Art. no. PC1244006, doi: 10.1117/12.2650317.

[4]. Z. Bian, X. Zhao, K. J. Rae, A. S. M. Kyaw, D. Kim, A. F. McKenzie, B. C. King, **J. Liu**, S. Thoms, P. Reynolds, N. D. Gerrard, J. Grant, J. R. Orchard, C. H. Hill, C. W. Munro, P. Ivanov, D. T. D. Childs, R. J. E. Taylor and R. A. Hogg, "Resonator embedded photonic crystal surface emitting lasers," in *Proc. 28th Int. Semiconductor Laser Conf. (ISLC)*, Matsue, Japan, 2022, pp. 1-2, doi: 10.23919/ISLC52947.2022.9943455.

[5]. A. S. M. Kyaw, B. C. King, A. F. McKenzie, N. D. Gerrard, Z. Bian, D. Kim, **J. Liu**, X. Zhao, K. Nishi, K. Takemasa, M. Sugawara, D. T. D. Childs, C. H. Hill, R. J. E. Taylor and R. A. Hogg., "Epitaxially regrown quantum dot photonic crystal surface emitting laser," in *Proc. 28th Int.*

Semiconductor Laser Conf. (ISLC), Matsue, Japan, 2022, pp. 1-2, doi: 10.23919/ISLC52947.2022.9943442.

[6]. B. Saleeb-Mousa, D. Spence, M. Haji, **J. Liu**, S. Watson, R. A. Hogg, A. O'Dowd, C. Hill, D. T. D. Childs, and R. J. E. Taylor, "Spectral linewidth of photonic crystal surface emitting lasers," in *Proc. 28th Int. Semiconductor Laser Conf. (ISLC)*, Matsue, Japan, 2022, pp. 1-2, doi: 10.23919/ISLC52947.2022.9943393.

Posters

[1]. **J. Liu**, X. Zhao, D. Kim, J. R. Orchard, D. T. D. Childs, R. J. E. Taylor, P. Harvey, S. J. Sweeney and R. A. Hogg, "Exploring high efficiency PCSELs using probabilistic Markov chain model" in International PCSEL workshop 2025, Glasgow, UK, 2025

[2]. **J. Liu**, D. Kim, Z. Bian, J. Feng, Y. Gao, P. Ivanov, P. Harvey, S. J. Sweeney, and R. A. Hogg, "Probabilistic Markov chain modelling of PCSEL losses", in International PCSEL workshop 2024, Birmingham, UK, 2024

[3]. **J. Liu**, Y. Gao, P. Ivanov, P. Harvey, S. J. Sweeney, and R. A. Hogg, "Probabilistic Markov chains modelling for photonic crystal surface emitting lasers (PCSELs)" in ESLW 2023, Glasgow, UK, 2023

Chapter 1: Introduction

The pursuit of high-performance semiconductor lasers has been a driving force in photonics research for decades, enabling revolutions in telecommunications, data storage, sensing, and displays. [1] From the early Fabry-Perot (F-P) lasers to the highly refined distributed feedback (DFB) lasers [2-3] and vertical cavity surface emitting lasers (VCSELs) [4-5], each generation has brought improvements in efficiency, beam quality, and functionality. However, a fundamental challenge has persisted: the inherent trade-off between high output power and a high-quality, single-lobe output beam. Conventional edge-emitting lasers can achieve high power but typically exhibit poor beam quality due to multi-mode operation and high beam asymmetry, [6] while VCSELs offer excellent beam quality but have historically been limited in their single-mode output power. [7]

The photonic crystal surface-emitting laser (PCSEL) has emerged as a groundbreaking platform that uniquely addresses this challenge. By leveraging a two-dimensional (2D) resonant cavity within a photonic crystal (PC) slab, the PCSEL inherently produces a high-power, single-mode, large-area and vertically emitting beam. This is achieved through a coherent 2D resonance that allows the device area to be scaled up to increase power without degrading the beam quality, a feat difficult to accomplish with traditional laser architectures. This combination of high power and high beam quality makes the PCSEL an exceptionally promising light source for next-generation applications such as light detection and ranging (LiDAR), free-space optical communication, photonic computing, and industrial processing. [8]

Despite their significant advantages, the design and optimization of PCSELs present unique complexities. The device performance is governed by the intricate interplay between microscopic scattering events at the level of individual PC atoms and macroscopic device-level parameters such as threshold gain and slope efficiency. The key among these macroscopic parameters is the in-plane loss ($\alpha_{//}$), which represents optical power leaking laterally out of the PC cavity and constitutes a major parasitic loss that limits slope efficiency and increases the threshold current. Unlike mirror loss (α_m) in F-P lasers, $\alpha_{//}$ is exceptionally difficult to measure experimentally, creating a critical gap in the design feedback loop. Traditional simulation methods, such as rigorous coupled-wave analysis (RCWA) or 3D finite-difference time-domain (FDTD) simulations, while powerful, are computationally intensive and often too complex for rapid, parametric exploration of device designs.

This thesis introduces and validates a novel, computationally efficient simulation tool, the Probabilistic Markov Chain (PMC) model, to bridge the critical gap between microscopic physics and macroscopic device performance. The core innovation of the PMC model is its treatment of light propagation within the PCSEL as a stochastic process. It translates physically meaningful coupling coefficients (κ_{1D}, κ_{2D}, $\kappa_{\perp}$, κ_i) into probabilities of optical power scattering between discrete directional states (North, South, East, West, Vertical) at each PC atom. This approach bypasses the need to solve Maxwell's equations directly, instead using a statistical framework to model power flow, loss, and emission in finite-sized devices.

Chapter 2 reviews the background knowledge, from key semiconductor definitions, basic theory, to device development. Then the main research target, PCSEL lasing theory, characterization, and existing simulation methods are described.

The thesis is structured to systematically establish the PMC model, validate it against experimental data, and then deploy it to explore and propose novel PCSEL designs for enhanced performance. **Chapter 3** provides a detailed description of the PMC model's fundamentals, including its algorithm, state definitions, and the crucial convergence criteria necessary for obtaining accurate results. Initial validation is performed by successfully predicting the performance of a standard PCSEL and a Resonator Embedded PCSEL (REPCSEL).

Chapter 4 utilizes the PMC model to conduct a comprehensive parameter study. It investigates the influence of in-plane coupling coefficients on $\alpha_{//}$ and explores the integration of in-plane mirrors, demonstrating their profound effect on reducing in-plane loss and enabling mode selection, as exemplified by the REPCSEL design.

Chapter 5 addresses a common design practice: the use of an unpumped PC boundary to reduce $\alpha_{//}$. The PMC model reveals a previously unexplored interdependence between in-plane and internal loss (α_i) due to self-absorption in the unpumped quantum wells. This finding challenges the conventional wisdom that simply widening the unpumped boundary is a straightforward path to loss reduction, introducing the concept of a total "parasitic loss."

Finally, **Chapter 6** leverages the insights from previous chapters to propose and theoretically evaluate three novel, high-efficiency PCSEL designs that aim to overcome the limitations of the absorptive boundary. These designs—incorporating butt-coupled passive sections, selective area intermixing, and a dual-contact scheme—are compared systematically using the PMC model, with their potential for maximizing power conversion efficiency (PCE) critically

assessed.

In summary, this thesis presents the development and application of the PMC model not merely as a simulation tool, but as a versatile and powerful design engine for PCSELs. It provides fundamental insights into loss mechanisms and pioneers new architectural pathways towards realizing the full potential of photonic crystal surface-emitting lasers.

References

[1]. R. N. Hall, G. E. Fenner, J. D. Kingsley, T. J. Soltys, and R. O. Carlson, "Coherent light emission from GaAs junctions," *Phys. Rev. Lett.*, vol. 9, no. 9, pp. 366–368, Nov. 1962.

[2]. H. Kogelnik and C. V. Shank, "Coupled-wave theory of distributed feedback lasers," *J. Appl. Phys.*, vol. 43, no. 5, pp. 2327–2335, May 1972, doi: 10.1063/1.1661499.

[3]. K. Aiki *et al.*, "GaAs-GaAlAs distributed-feedback diode lasers with separate optical and carrier confinement," *Appl. Phys. Lett.*, vol. 27, no. 3, pp. 145–146, Aug. 1975, doi: 10.1063/1.88386.

[4]. H. Soda, K. Iga, C. Kitahara, and Y. Suematsu, "GaInAsP/InP surface emitting injection lasers," *Jpn. J. Appl. Phys.*, vol. 18, no. 12, pp. 2329–2330, Dec. 1979, doi: 10.1143/JJAP.18.2329.

[5]. F. Koyama, S. Kinoshita, and K. Iga, "Room-temperature continuous wave lasing characteristics of a GaAs vertical cavity surface-emitting laser," *Appl. Phys. Lett.*, vol. 55, no. 3, pp. 221–222, Jul. 1989, doi: 10.1063/1.101913.

[6]. G. Morthier and P. Vankwikelberge, *Handbook of Distributed Feedback Laser Diodes*, 2nd ed. Norwood, MA, USA: Artech House, 2013.

[7]. K. Iga, "Vertical-cavity surface-emitting laser: Its conception and evolution," *Jpn. J. Appl. Phys.*, vol. 47, no. 1, pp. 1–10, Jan. 2008, doi: 10.1143/JJAP.47.1.

[8]. S. Noda *et al.*, "High-power and high-beam-quality photonic-crystal surface-emitting lasers: A tutorial," *Adv. Opt. Photon.*, vol. 15, no. 4, pp. 977–1032, 2023, doi: 10.1364/AOP.502863.

Chapter 2: Background, Gaps in Knowledge and Contribution to the Field.

2.1 Introduction

Semiconductor lasers have been related to the recent development of human society serving over a wide range of fields, such as data- and telecommunications and optical storage. Their outstanding characteristics are wide wavelength accessibility [1-6] and modulation speed [7-8]. Lasing in semiconductors is realized by combining stimulated emission with a resonator. The emission area is limited by single lateral mode, because of which the brightness of semiconductor lasers is much less than that of bulky lasers such as gas and solid-state lasers. Simply increasing the emission area will cause parasitic lateral-mode oscillations, which may result in reduced beam quality. [9-10] Another cause of unstable oscillation are the thermal effects in resonators under continuous-wave operation [11-12].

To realize single-mode, high-brightness and narrow beam divergence all in one laser, a new class of semiconductor laser, the photonic crystal surface emitting laser (PCSEL) has been demonstrated. [13-14] PCSELs utilize a 2-dimentional distributed Bragg reflector (DBR) as the resonator to realize a large emission area with an emission direction perpendicular to the gain and feedback plane.

In this chapter, the basic principles of lasing in semiconductor lasers are discussed. The discussion is then expanded to PCSELs. Based on which, new theory and corresponding characteristics of PCSELs are introduced. For further study, this new theory, commonly used simulation methods and their algorithms are briefly explained and commented on. Finally, the design process is analysed and a new design process to speed up the evolution of PCSEL design is proposed. This new simulation method, the probabilistic Markov chain (PMC) model is introduced.

2.2 Semiconductor Laser Diodes

The Schrödinger and Hamiltonian formulations describe physical phenomenon at the quantum level. The correct way to explain the anomalies arising in the classical description of heat radiation from the ‘black-body’ was formally shown by Max Planck with a quantum description. The most directly and explicit application of such quantum phenomenon is the ‘photoelectric effect’ explained by Albert Einstein.

At the quantum level, there are discrete values of the energy fluctuations of particles. Figure 2.1 plots a schematic of how electrons may receive or lose energy, and transition between energy E1 and E2, between which has a value of:

$$\Delta E = E_2 - E_1 \qquad equation2.1$$

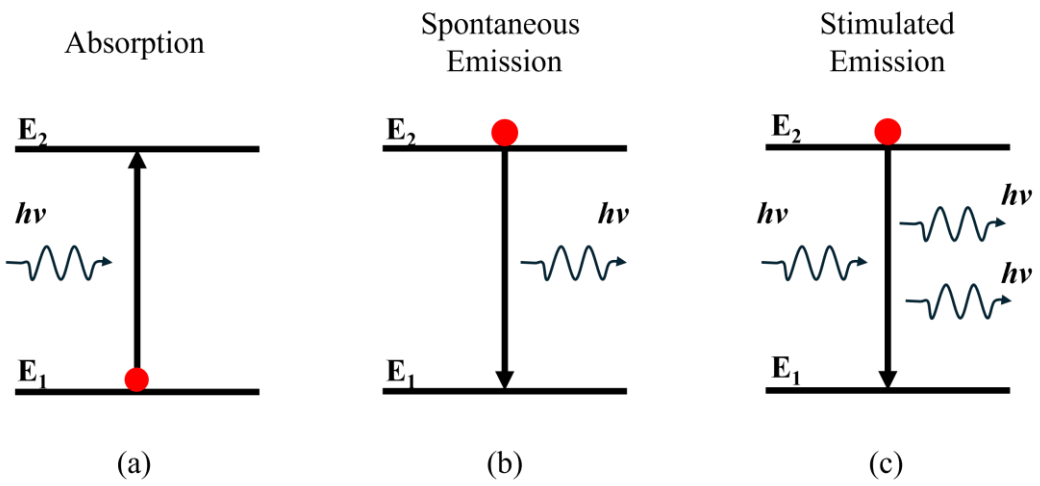

Figure 2.1: Schematic of electronic light-matter interactions behaviour (a) Absorption. (b) Spontaneous emission. (c) Stimulated emission.

Figure 2.1 (a) schematically shows photon absorption, when an electron receives energy (ΔE) due to photon annihilation, allowing it to be promoted from E_1 to E_2. Figure 2.1 (b) schematically shows the process where an electron transitions from E_2 to E_1 by itself and emits a photon with energy of ΔE. Figure 2.1 (c) shows another kind of emission proposed by Einstein, stimulated emission. The energy gap ΔE is decided by equation:

$$\Delta E = hv \qquad \text{equation2.2}$$

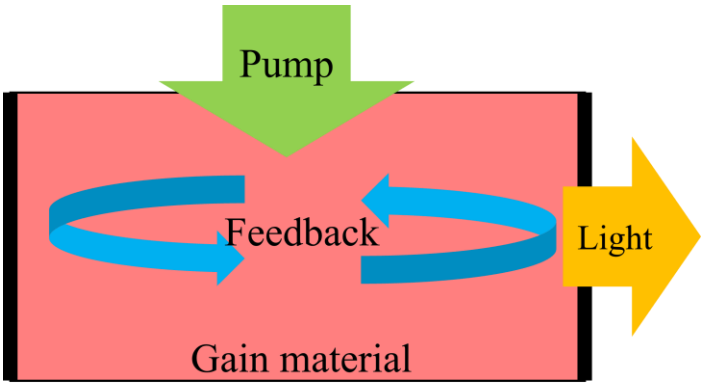

Figure 2.2: Schematic of a laser in basic design.

where h is a Plank constant, v describes the frequency of the emit photon when the electron

falls from E_2 to E_1, not by itself but triggered by an input photon with the same frequency. [15] It was noted that, for stimulated emission, not only the frequency of emitting photons is the same, but also all other features, such as phase, polarization, and direction of emission.

Lasers use stimulated emission to generate coherent radiation. However, normally the three phenomena mentioned in figure 2.1 may occur at the same time. To enhance the stimulated emission rate, high electron populations at higher energy levels are needed. To describe the circumstances when net stimulated emission is larger than zero, a gain, g is defined. Figure 2.2 shows a very basic design of a laser device aimed at enhancing gain. There are three elements to reach that goal, a gain material, pumping process and feedback element. There are multiple choices of gain material, such as gas [16], solid state [17], or semiconductor [18]. Pumping processes provide external energy and increases the high energy electron population, which termed inversion when the population of high energy states exceeds the lower energy population. The feedback element forces the radiation pass through the gain material to have phase matching, with out of phase light being destructively interfered.

2.3 Electromagnetic Theory for Semiconductor Lasers

The stimulated emission rate is proportional to the photon density, which means to reach better performance, a laser device needs a high population inversion, high levels of confinement of the light in a smaller volume. However, to meet both requirements, a very high drive current will be limited in a small area, which may result in an impractically high temperature caused by non-radiative transitions and free carrier losses which give rise to self-heating. A large lateral dimension also leads to higher probability of multi-mode operation or a large divergence angle of the output beam. The typical optical gain materials of semiconductors have higher refractive indices, because of which the electromagnetic field tends to be localized in the direction of epitaxial growth.

To allow in-plane optical localisation, several designs of semiconductor laser device have introduced lateral confinement, such as ridge waveguide lasers, and buried heterostructure lasers.

Figure 2.3 presents schematic diagrams of different laser configurations. As the simplest ridge-waveguide structure, the Fabry–Perot (FP) laser, illustrated in Figure 2.3(a), places the gain medium between two parallel mirror facets. Optical feedback occurs along the ridge direction, and light is emitted through a cleaved facet of the semiconductor crystal that is perpendicular to the ridge. This design enabled the first demonstration of coherent light

emission from a semiconductor. Owing to its straightforward fabrication and ability to deliver high output power, the FP laser retains a notable presence in certain market applications today. It should be noted, however, that an FP laser typically operates on multiple longitudinal modes, resulting in poor spectral purity (broad linewidth) and significant wavelength drift with variations in temperature and current. Furthermore, its output beam is often elliptical and astigmatic. These limit the applicable scope of FP lasers.

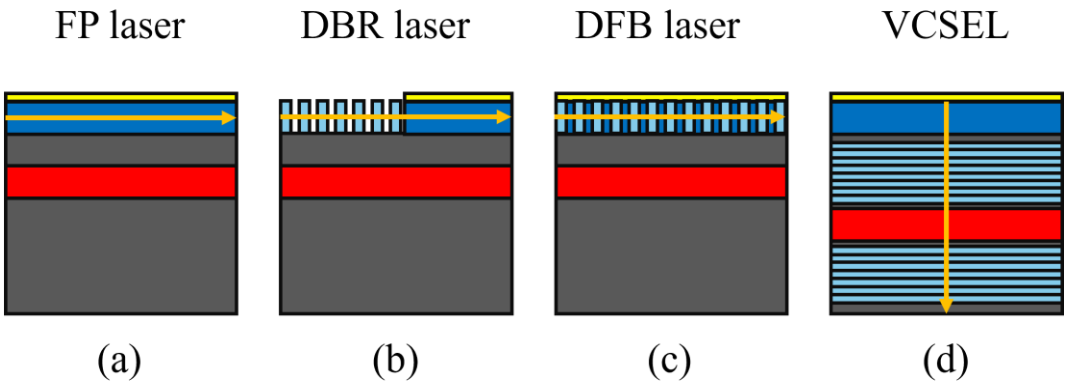

Figure 2.3: Schematic of different configurations of laser. (a) FP laser. (b) DBR laser. (c) DFB laser. (d) VCSEL

Figure 2.3(b) shows the distributed Bragg reflector (DBR) laser, which addresses the multi-mode limitation of the FP laser by introducing a wavelength-selective element into the cavity. This is achieved by replacing one or both of the FP laser's facet mirrors with Bragg reflectors—periodic structures that provide frequency selectivity through carefully designed layer widths and spacings. The use of Bragg mirrors represents a major advance toward single-mode operation, as they stabilize the output wavelength and significantly narrow the linewidth compared to FP lasers. However, the spatial separation between the gain section and the grating region complicates fabrication and current injection. Moreover, device performance is sensitive to fabrication tolerances due to the complexity of the grating structure.

Figure 2.3(c) illustrates the distributed feedback (DFB) laser, in which the Bragg grating is no longer merely a mirror at the cavity ends but is embedded directly into or adjacent to the gain region along its entire length. The DFB laser marks the ultimate refinement of in-plane single-mode lasers, offering exceptional single-mode stability, very narrow linewidth, and strong resistance to mode hopping under changes in temperature or current. Nevertheless, its output beam from the cleaved facet remains asymmetric, making DFB lasers less suitable for many free-space applications that require high spatial beam quality.

Figure 2.3(d) presents a schematic of a vertical cavity surface emitting laser (VCSEL). This structure achieves single-mode operation by sandwiching the gain medium between two DBR mirrors in the epitaxial (vertical) direction. As the schematic illustrates, the optical cavity is oriented vertically, enabling surface-normal emission. Single-mode operation is realized by restricting higher-order spatial modes through careful control of the device's aperture size. Additionally, the vertical integration of gain, feedback, and emission allows for high die density and eliminates the need for facet cleaving, significantly simplifying wafer-scale testing and packaging. However, these advantages introduce distinct challenges: high-power operation is constrained by the limited single-aperture size, while heat dissipation poses a significant difficulty due to the compact vertical structure. Although the architecture removes the requirement for cleaved facets, it imposes stringent demands on epitaxial growth to achieve the necessary high-reflectivity DBR mirrors.

It is important to note that, throughout the development of semiconductor lasers, the in-plane (co-axial) devices illustrated in Figure 2.3 have individually achieved high power, single-mode operation, wavelength selectivity, or narrow beam divergence. However, integrating all these desirable characteristics into a single in-plane laser structure has proven challenging.

2.4 Photonic Crystal Surface Emitting Lasers

Since the theory of periodic structure studied and reported by Léon Brillouin, Felix Bloch, and William Bragg, the application of it, the Bragg grating, benefits many optical fields, especially the development of semiconductor lasers. However, there is still room for improvement for conventional classes of semiconductor lasers, such as in realizing high brightness, narrow beam divergence and single-mode operation in one device.

The idea of one-dimensional (1D) photonic crystal (PC) was proposed by Lord Rayleigh in 1887, and expanded to 2D and 3D in the following century through studying the inhibition of spontaneous emission [19] and photon localization [20]. With the study and application development in PCs, the theory of periodic structure is also receiving more attention and massive development, and promotes the development of multiple optical applications, such as PC fibres, PC waveguides, and the key study object of this thesis, photonic crystal surface emitting lasers (PCSELs). PCSELs were reported in 1999 independently by Noda *et al.* and Meier *et al*., and named after its core requirement, a coherent 2D resonator realized by PC. [21-22]

2.4.1 Bragg Condition

The Bragg condition describes the situation that incident electromagnetic waves with wavelength, λ are constructively diffracted with an incident angle, θ by the lattice structure of the target material with a particular lattice dimension. The behaviour is described as:

$$2a \sin\theta = n\lambda \qquad \text{equation2.3}$$

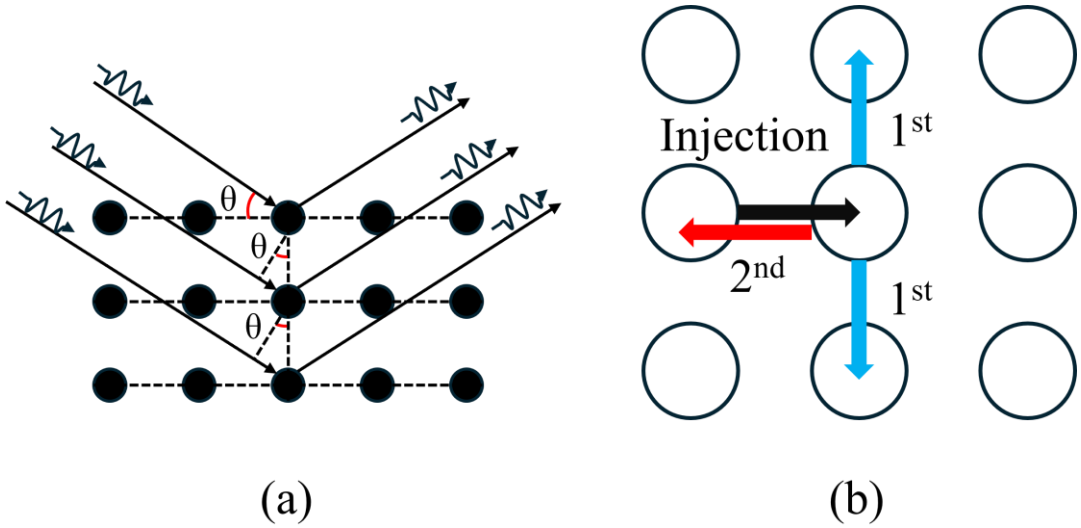

Figure 2.4: Schematic of (a) Bragg condition. (b) in-plane coupling of 2D PC with a square lattice.

a is the lattice constant of the wave injected lattice structure. n is an integer refers to the order of this optical behaviour. Figure 2.4 (a) shows the schematic of condition for constructive interference.

The PC is essentially a realization of a 2D Bragg grating. A schematic of a square lattice with a circular PCs design is shown in figure 2.4 (b). If the design meets the requirements in equation 2.2, two behaviours of in-plane light propagation will occur. When interaction with PCs, the light may be scattered to an orthogonal direction (θ = ±90°), which is due to 1st order Bragg condition, named also 2D coupling. Or, due to 2nd order Bragg condition, the light may be scattered backwards (θ = 180°), along with keeping the (unscattered) transition direction (θ = 0°) the behaviours are called 1D coupling.

2.4.2 Coupling Coefficients

As discussed above, 1D coupling and 2D coupling constitute the in-plane coupling behaviour of light in a PC. To describe the in-plane coupling in a square lattice PC, coupled-wave theory (CWT) was proposed by Sakai *et al.* [23-24]. The theory assumes a square lattice with circular (in x and y direction) holes in which the z direction is uniform, and describes the magnetic field in TE mode as:

$$\frac{\partial}{\partial \mathrm{x}}\left\{\frac{1}{k^2}\frac{\partial H_z}{\partial \mathrm{x}}\right\}+\frac{\partial}{\partial \mathrm{y}}\left\{\frac{1}{k^2}\frac{\partial H_z}{\partial \mathrm{y}}\right\}+H_z=0 \qquad \text{equation2.4}$$

Where

$$\frac{1}{k^2}=\frac{1}{\beta^3}\left\{\beta+2\sum_{\boldsymbol{G}\neq 0}\kappa(\boldsymbol{G})exp[i(\boldsymbol{G}\cdot r)]\right\} \qquad equation2.5$$

G is the reciprocal lattice vector defined as:

$$\boldsymbol{G}=(m\beta_0,n\beta_0) \qquad \text{equation2.6}$$

m and n are arbitrary integers.

$$\beta_0=\frac{2\pi}{a} \qquad equation2.7$$

a is the lattice constant.

$$\beta=\frac{n_{av}\omega}{c} \qquad equation2.8$$

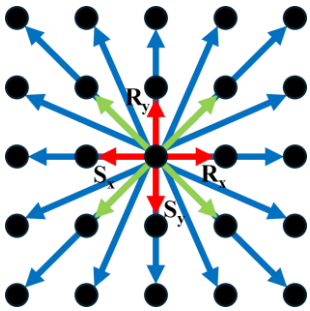

Figure 2.5: Diagram of the corresponding in-plane coupling in reciprocal space. Red arrows represent four fundamental Bloch waves (Rx, Sx, Ry, Sy), green arrows are direct higher-order Bloch waves, blue arrows are indirect higher-order Bloch waves.

n_{av} is the averaged refractive index of photonic crystal which defined by a fill factor f:

$$n_{av}=\sqrt{f_1{n_1}^2+f_2{n_2}^2} \qquad \text{equation2.9}$$

Where $f_1+f_2=1$. [25] A coupling constant is defined as:

$$\kappa(\boldsymbol{G})=\frac{\pi n_{\boldsymbol{G}}}{\lambda} \qquad \text{equation2.10}$$

Where n_G is the Fourier coefficient of the periodic refractive-index modulation and λ is the Bragg wavelength given by $\lambda = an_{av}$.

Figure 2.5 shows a diagram of the corresponding in-plane coupling in reciprocal space, and red arrows represent four fundamental Bloch waves (R_x, S_x, R_y, S_y), green arrows are direct higher-

order Bloch waves, blue arrows are indirect higher-order Bloch waves.

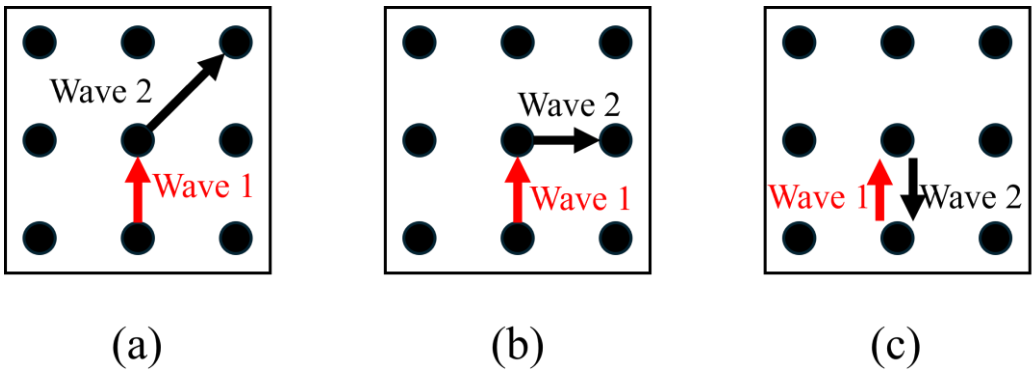

Figure 2.6: Schematic of coupling coefficients, (a) κ_1, (b) κ_2, and (c) κ_3

Within the defined coupling diagram, only 2nd order or below diffraction are considered to have large enough value to be significant, which means $|m|+|n|\leq 2$. Then three corresponding coupling constants κ_1, κ_2, and κ_3 are defined as:

$$\kappa_1 = \kappa(\boldsymbol{G})|_{|\boldsymbol{G}|=\beta_0} \qquad equation 2.11.1$$

$$\kappa_2 = \kappa(\boldsymbol{G})|_{|\boldsymbol{G}|=\sqrt{2}\beta_0} \qquad equation 2.11.2$$

$$\kappa_3 = \kappa(\boldsymbol{G})|_{|\boldsymbol{G}|=2\beta_0} \qquad equation 2.11.3$$

Figure 2.6 shows the schematics of those coupling coefficients among PCs. κ_1 is the coupling coefficient describing the 45° coupling. κ_2 represents 90° coupling, which disappears in the case of square lattice PC with TE polarization, because of the cancelling between two perpendicular waves. κ_3 is 180° coupling which corresponds to the backward scattering in 2nd order DFB lasers.

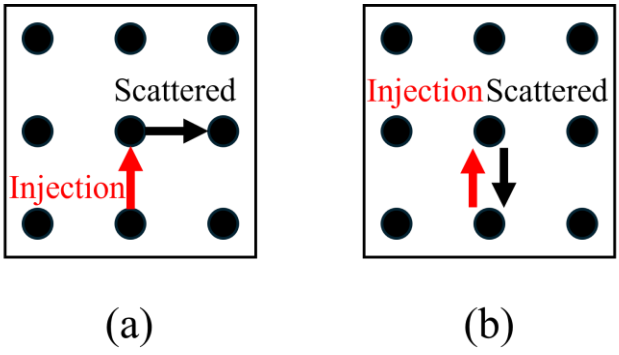

Figure 2.7: Schematic of coupling coefficients described in orthogonal directions. (a) κ_{1D} and (b) κ_{2D}

Taylor *et al.* [26] proposed another way to explain those coupling coefficients with a beam scattering theory in orthogonal directions only. Figure 2.7 (a) describes the behaviour of beam

scattering backwards when interacting with PC, κ_{1D}, which match the description of $\kappa 3$, so the value shall be the same too. Figure 2.7 (b) describes the beam behaviour of scattering to a perpendicular direction (in-plane ±90◦) the value is defined as:

$$\kappa_{2D} = \frac{2 * {\kappa_1}^2}{\beta_0} \qquad equation 2.12$$

These two coupling coefficients are described as in-plane coupling coefficients and preferentially used in this thesis. The vertical coupling (or scattering) has a similar mechanism as the in-plane coupling, but related to a device-level loss (out-of-plane loss), which will be discussed in following section.

2.4.4 Band Structure

The 2D PC with square lattice can be regarded as an array with designed shape in material 1, with refractive index n_1, embedded in a background material 2 with refractive index n_2. Or, another description preferred in this thesis, a compact array composed of unit cells (also named PC atoms) in square shape. The conventional design of such a unit cell is a combination of two materials of different refractive indices (n_1 and n_2), in which material 1 used as a background material in square shape, and material two used as the field material in a single closed shape. Special cases may break the rule, such as air-hole embedded PC, in which air, as a material 3 is built in by using a special epitaxy process, or double-lattice PC, in which there are two oval shape pattern. Figure 2.8 (a) plots the schematic of circular PC with square lattice. The inset of figure 2.8 (a) shows the definition of the above-mentioned unit cell, in which the size of the atom is defined by the lattice constant, a, and in this case material 2 is circular in shape with radius, r, and shares the same centre as squared shape material 1. So, the unit cell can be described by equation 2.9, or more detailed as:

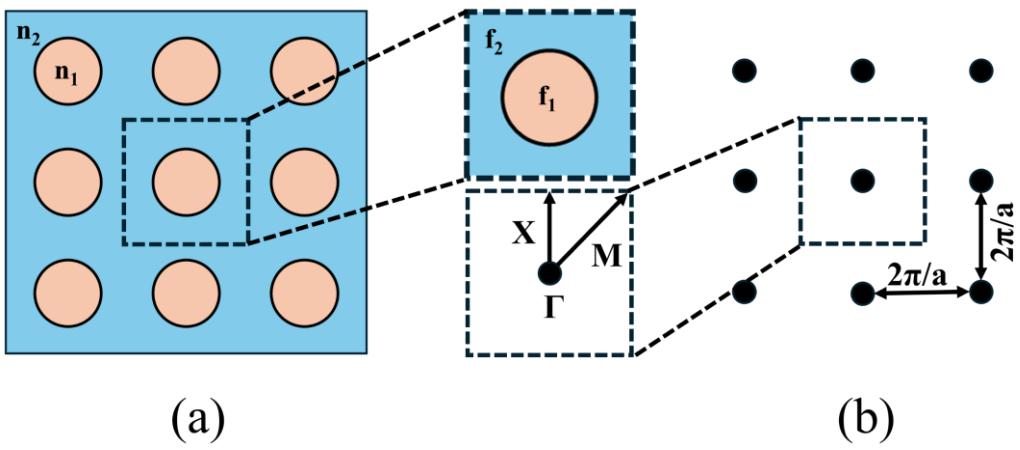

Figure 2.8: (a) Schematic of circular PC with square lattice. (b) Schematic of reciprocal lattice of (a)

$$n_{av} = n_1 \frac{a^2 - \pi r^2}{a^2} + n_2 \frac{\pi r^2}{a^2} \qquad \text{equation2.13}$$

This thesis will not focus on the design of PC, but focuses more about how the whole unit cell behaves, so in the future descriptions, the pattern shape is used to represent the whole unit cell, not just the pattern material. Figure 2.8 (b) plots the reciprocal lattice of figure 2.8 (a), the gap between atoms in reciprocal space is 2π/a, the first Brillouin zone has been highlighted in red square, which is equivalent to the unit cell defined above. The inset of figure 2.8 (b) shows one unit of Brillouin zone, in which the zone-centre, named as Γ, has group velocity equal to zero. Based on which, the fundamental corresponding directions are defined as Γ-X direction, and direct higher order corresponding directions are defined as Γ-M direction. Due to the symmetry of a unit cell (in this case, circular pattern), the photonic band structure can be represented using a X -Γ-M region. The calculation method will be discussed later in section 2.3.5. There are some special points shown in figure 2.9 (Γ1, Γ2, X1 and M1), at where the mode density increases due to the light coupling in different directions. According to coupled-mode theory, X_1 and M_1 correspond to two fundamental directions. Surface emission is achieved at the second-order Γ point (Γ_2). Since single-mode operation is typically preferred in design, higher-order band-edges are not prioritized in photonic crystal surface-emitting laser (PCSEL) designs due to their potential multi-directional emission. The inset shows a detailed view of the Γ_2 point, where the bands intersect and separate. Consequently, the Γ_2 mode is selected as the target lasing point in the following discussion.

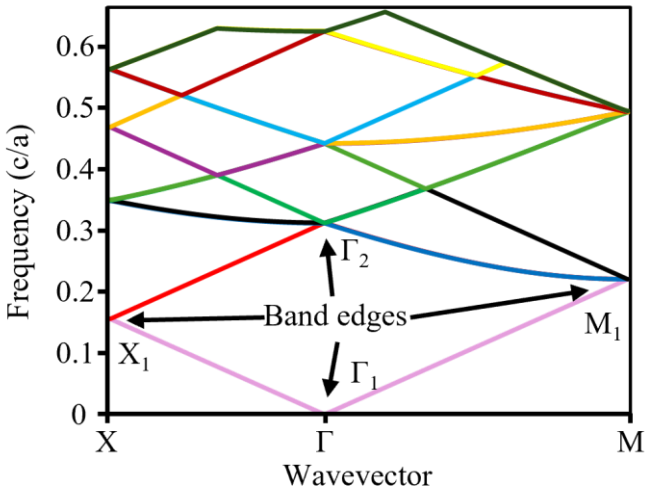

Figure 2.9: Example of band structure.

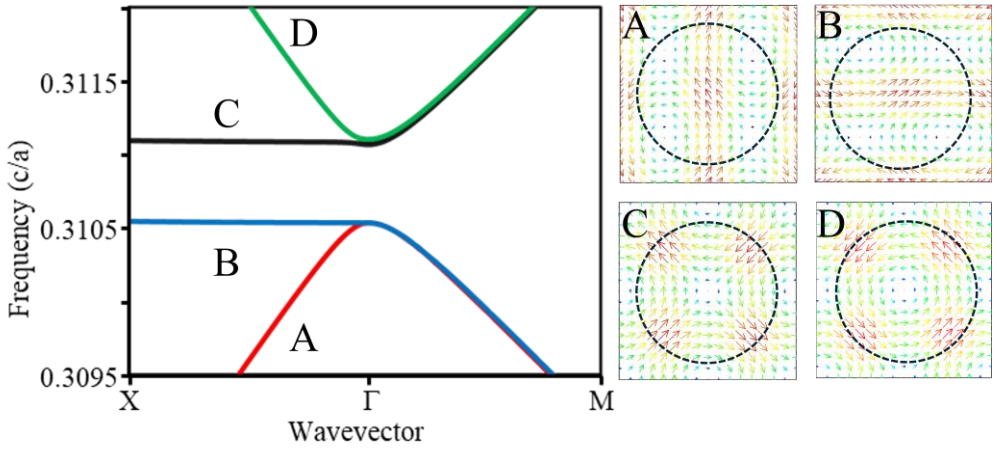

Figure 2.10: The In-plane electric field distribution of band A, B, C and D at Γ2 of the example photonic band structure shown in figure 2.9.

For 2D PCSEL, only PCSELs operating in transverse electric (TE) mode are discussed. Figure 2.10 plots the electromagnetic field distribution of the four modes (A, B, C and D) at Γ2. Non-leaky modes (mode A and B) are those modes having destructive interference of the vertically diffracted light caused by the nonsymmetric in-plane electric field, in which high vertical optical confinement and low surface emission intensity are realized. On the contrary, those mode (mode C and D) with highly symmetric in-plane electric fields have no vertically diffracted light cancellation, due to which have low vertical optical confinement and higher output are called leaky modes. It should be noted that due to the symmetry of a circular PC, the threshold can be low but there is low vertical radiation loss, or low emission power.

2.3.5 Optical loss and Waveguide Engineering

In a semiconductor laser diode, optical gain is achieved by creating a population inversion in the active region via electrical injection. This allows the stimulated emission rate to exceed the absorption rate for photons in the optical mode of the waveguide.

The material gain coefficient quantifies this net amplification per unit length. For lasing oscillation to be sustained, this gain must be sufficient to overcome all losses the optical mode experiences inside the cavity. The lasing threshold is reached when the round-trip modal gain equals the total round-trip modal loss (sum of internal waveguide losses and output coupling losses through the mirrors).

In a FP laser, the threshold gain is described in equation:

$$g_{th} = \alpha_{\mathrm{m}} + \alpha_i \qquad \text{equation2.14}$$

α_m is mirror loss which given by:

$$\alpha_m = \frac{1}{L} ln \frac{1}{r_1 r_2} \qquad equation2.15$$

In which L is the total cavity length and r_1 and r_2 are the facet reflectivities. α_i is the internal optical loss, which refers to the optical loss that occurs within the laser cavity due to various mechanisms, excluding the useful output coupling, α_m. Internal loss is caused by multiple processes, such as free-carrier absorption, active region absorption, or scattering. As a result, there is no single equation to define α_i, but the net internal loss $\langle \alpha_i \rangle$ can be determined by comparison between to identical lasers except their cavity length (L^a and L^b):

$$\langle \alpha_i \rangle = \frac{\eta_d^a - \eta_d^b}{L^a \eta_d^a - L^b \eta_d^b} ln \frac{1}{r_1 r_2} \qquad equation2.16$$

η_d is the differential quantum efficiency, which defined by output power P and operating current I at or beyond threshold as:

$$\eta_d = \left[\frac{q}{hv}\right] \frac{dP_o}{dI} \qquad equation2.17$$

For PCSEL equation 2.15 is adjusted for including vertical emission:

$$g_{th} = \alpha_{//} + \alpha_{\perp} + \alpha_i \qquad \text{equation 2.18}$$

α// is the in-plane loss that represents the optical power exist the PC region from an in-plane direction, in this thesis, the value is assumed to be evenly separated on four edges of the PC with square lattice. α⊥ is out-of-plane loss describes the emission on one vertical direction (upwards or downwards), perpendicular to plane of PC region.

Slope efficiency is commonly used to characterize PCSEL at the device-level, it is defined as the optical power above threshold per unit injection current and given by:

$$\eta_{SE} = \frac{1.24}{\lambda}(1-A)\eta_i \frac{\frac{1}{2}\left(1+2\sqrt{R}\cos\theta+R\right)\alpha_{\perp}}{\left(1+\sqrt{R}\cos\theta\right)\alpha_{\perp}+\alpha_{//}+\alpha_i} \qquad \text{equation2.19}$$

λ is the operating wavelength of PCSEL, A is the absorption ratio of laser substrate, η_i is the carrier injection efficiency of the active layer, which mostly assumed to be 0.9 in this thesis, R is the vertical reflectivity provided by vertical DBR or contact, θ is the phase of reflected light.

Due to the special loss distribution condition shown in figure 2.18, the power conversion efficiency (PCE) of PCSEL is poor, as compared to other classes of semiconductor lasers. This low PCE, yet high power and brightness have stimulated simulation and experimental work world-wide. The currently adopted design flow is described below.

2.3.6 Design Flow

The typical design flow of a PCSEL starts from the analysis of epitaxy regrowth structure of the device. The key point is matching the PC to the active region in the target wavelength and ensuring the optical mode has sufficient overlap to both the PC and the active region.

PC structural design has been the major object of study since the invention of the PCSEL. Without considering any difficulties caused by the nanofabrication process, such as limitations placed by e-beam lithography, etch, and re-growth, any shape of the PC can be imagined. However, a common design concept is to balance the in-plane coupling strength and light cancellation through destructive interference. One common idea is to break the symmetry of the pattern shape. Aside from the symmetry of the pattern, the thickness, d_{PC} of the PC (or z-direction shape in 3D PC) is another factor to be considered, which is given by:

$$d_{PC} = \mathrm{m} * \left(\frac{a}{2}\right) \qquad \text{equation2.20}$$

Where m is the mode index (integer).

The simulated band structure helps determining the coupling coefficients of the design, and the effect of these coefficients will be analysed and discussed in chapter 4. The value of coupling coefficients can be affected by not only the shape of the pattern but also the fill factor of the pattern and the refractive indices of background and pattern materials.

With d_{PC} and averaged refractive index, n_{av}, the optical mode can be simulated in the z-direction

by considering the epitaxial structure as a FP laser. The optical mode is the bound mode of light confined inside of the device waveguide. It is calculated by solving Helmholtz equations:

$$\left(\frac{\partial^2}{\partial x^2}+\frac{\partial^2}{\partial y^2}+{k_0}^2\left((x,y)-n(eff,m)^2\right)\right)E_m(x,y,z)=0 \qquad \text{equation2.20}$$

Where k0 is the wave propagation, n (eff, m) is the effective refractive index from a given mode, $E_m(x,y,z)$ is the electric field distribution of such mode in x, y and z direction, x and y are in-plane coordinates, and z is the vertical direction (epitaxial direction), so it can be described as:

$$E_m(x,y,z)=E_m(x,y)\exp(ik_0n(eff,m)z) \qquad \text{equation2.21}$$

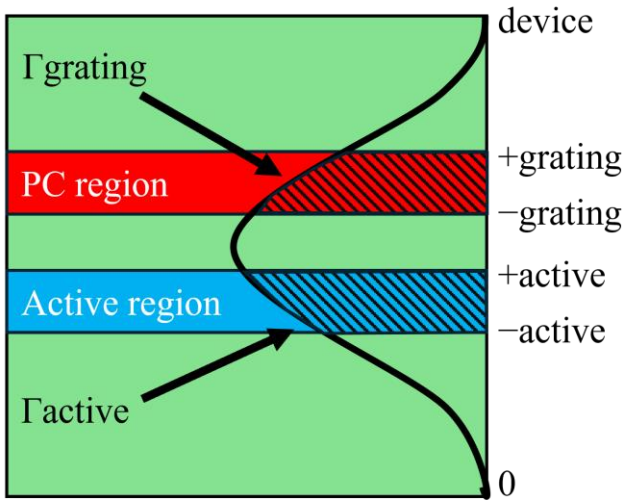

Figure 2.11: Schematic of optical mode overlap on the simplified epitaxy structure.

The most interesting parts are the overlap of optical mode on active region and grating region (PC). Confinement factors are defined to describe this overlap:

$$\Gamma_{active}=\frac{\int_{-active}^{+active}|E(z)|^2dz}{\int_0^{device}|E(z)|^2dz}=\frac{Light\ intensity\ of\ active\ region}{Total\ light\ intensity} \qquad equation2.22.1$$

$$\Gamma_{grating}=\frac{\int_{-grating}^{+grating}|E(z)|^2dz}{\int_0^{device}|E(z)|^2dz}=\frac{Light\ intensity\ of\ grating}{Total\ light\ intensity} \qquad \text{equation2.22.2}$$

While ensuring enough total light intensity, maximizing Γ_{active} and $\Gamma_{grating}$ makes the PCSEL have more ideal characteristics. Engineering the overlap with lossy cladding layers will affect the value of internal loss, the lower such overlap is, the lower internal loss and threshold gain will be, the resulting in higher device efficiency.

2.5 Previous Simulation Methods

As mentioned above, it can be noticed that the design and fabrication process are relatively complicated. Previous research has focussed on the development of many simulation methods to help understand the PCSEL operating mechanisms and support the design process. Existing simulation methods for PCSELs are mostly based on solving Maxwell's equation and calculating the electromagnetic fields among PC layer (finite or infinite area). Several of them are generally accepted and discussed thoroughly in the published literature, such as finite difference time domain (FDTD), plane wave expansion (PWE), and coupled wave theory (CWT).

FDTD, probably is the most widely used computational electromagnetism method due to its simplicity, generality and robustness. The method implements full time-dependent Maxwell's equations for arbitrary materials and various boundary conditions. [27-31] Its simplicity lowers the barrier to use with researchers benefiting in studying new interactions of physical processes.

The calculation starts from discretization of space and time into a grid. An example method is the Yee grid discretization; [32] the method separately samples the electric and magnetic fields at different spatial locations with an offset of half a pixel (based on the selected resolution), the samples are taken from components of the fields calculated in time and space. Then the derivatives of time and space are calculated by a centre-difference approximations. [33] The calculation is done within a computational cell, which should be a finite volume of space with proper boundary conditions. The boundary condition helps the method to expand calculation from one repetitive cell to a finite area. For PCSEL development, Bloch-periodic boundary conditions are commonly used. [34] At last, those field components are used in calculating target characteristics, such as lasing circumstances and the far-field pattern [35]

FDTD is generally used in simulating the lasing mode and in far-field pattern analysis. However, a Fourier calculation is needed if FDTD is used to explore the photonic band gap. Due to the large computational resource requirement, the FDTD (especially 3D FDTD) can be helpful only in analysis of the resonant frequency, loss conditions and mode profiles of PCSELs of small size (fewer than 100×100 #PC). [36] More importantly, the programming and training time could be a more practical problem for implementation. [37]

In conclusion, FDTD as a pure numerical simulation method may have coding barriers for those non-professional coders, but commercial solutions are powerful enough and very convenient for users to use. The real challenge of using FDTD is the required computational

resources or run-time for practical PCSEL device sizes with required resolutions. So, if the purpose is the study of a PCSEL's working mechanism, FDTD can be impractical.

PWE [38-39] is based on Floquet's theorem, expanding eigenmodes of the photonic crystal as an orthogonal and complete set (plane waves). The in-plane waves are indicated in a reciprocal lattice (shown in figure 2.8 (b)), along with which, the dispersion relation within X-Γ-M directions or the band diagram of the modes can be calculated. The conventional PWE assumes the device has an infinite thickness, which means the confinement of photons in the PC and/or active region is not considered. To solve this problem, two dielectric constants calculated from the electric field distribution in the vertical direction are introduced to the algorithm. [40] The value of these two constant ε_a and ε_b can be calculated from:

$$n_{eff}{}^2 = f_a\varepsilon_a + f_b\varepsilon_b \qquad \text{equation2.23.1}$$

$$\Delta\varepsilon = \varepsilon_a - \varepsilon_b \qquad \text{equation2.23.2}$$

Where n_{eff} is the effective refractive index, f is the fill factor, and $f_a+f_b=1$. The difference $\Delta\varepsilon$ is calculated from the confinement factor of PC on the difference between the dielectric constant of the background and PC pattern material. At last, the band diagram can be calculated by considering those two constants.

It can be noted that as a numerical method of simulation, PWE has advantages in analysing the band diagram, especially in analysing PCSEL's dispersion relation of eigenmodes and its attributes, e.g. frequency. It showed excellent efficacy in supporting the design of the very first PCSEL in 1999. [41] However, it cannot be used to analyse the lasing modes of finite-sized PCSELs. It provides no information about out-of-plane scattering. Furthermore, the algorithm is based on expanding the Maxwell's equations with a large number of plane waves, which may lead to a very large requirement on computational resources. [42]

Coupled-wave theory (CWT) is commonly used in analysis of 1D DFB lasers [43], and extended to the analysis of 2D DFB lasers, which contains a low refractive-index-contrast square lattice structure and operates at TE-polarized modes [44]. Obviously, the original CWT already has a large overlap with PCSEL simulation requirements. However, the in-plane orthogonal direction coupling among four fundamental Bloch waves was not considered until 2006, [45] which leads to the absence of CWT in the early study of the PCSEL. [46]

In 2006, Sakai *et al.* improved CWT by considering the four fundamental and four direct high-order Bloch waves in an eight-wave model (discussed in figure 2.5), which proves the

possibility of CWT in supporting PCSEL simulation. [45,47] Then a 3D-CWT was developed in the following few years, considering higher-order Bloch waves and radiative waves which makes PCSEL design more realistic. [48-51] To get more information, the most recent upgrade of CWT combines a time-dependent method, and considers thermal effects as well as carrier-photon interaction, with which the analysis can be expanded to device level characterization. [52-53]

The coupling waves can be expressed in CWT as:

$$(\delta + i\alpha)\begin{pmatrix} R_x \\ S_x \\ R_y \\ S_y \end{pmatrix} = C\begin{pmatrix} R_x \\ S_x \\ R_y \\ S_y \end{pmatrix} + i\begin{pmatrix} \partial R_x/\partial \mathrm{x} \\ -\partial S_x/\partial \mathrm{x} \\ \partial R_y/\partial \mathrm{y} \\ -\partial S_y/\partial \mathrm{y} \end{pmatrix} \qquad \text{equation2.24}$$

Where C represents a 4 × 4 matrix corresponding to different coupling behaviours of within the eight-wave model. CWT can also predict threshold gain, field intensity envelope, far-field pattern and polarization.

3D CWT has supported several outstanding experimental-based research works, such as the loss analysis of the first GaAs-based Watt-class PCSEL and GaN-based Watt-class PCSEL. [54] The highest brightness PCSEL is also based on the CWT analysis. [55]

In conclusion, comparing the above-mentioned numerical simulation methods, CWT provides a more analytical method to simulate PCSEL, and requires relatively less computational resource, which expands the size of finite-size PCSEL from 100×100 #PC in FDTD to many 1000×1000 #PC. The complex mathematical calculations make a barrier to entry in the implementation of CWT for PCSELs. The starting point of a PC shape (2D or 3D), solution of Maxwell's equations and determination of device level losses makes the development of physical understanding and intuition slow.

Reference

2.6 Summary and Outline of Thesis

As discussed previously, the engineering of the PC structure has gained most of the research interest and has so far been regarded as the major study object.

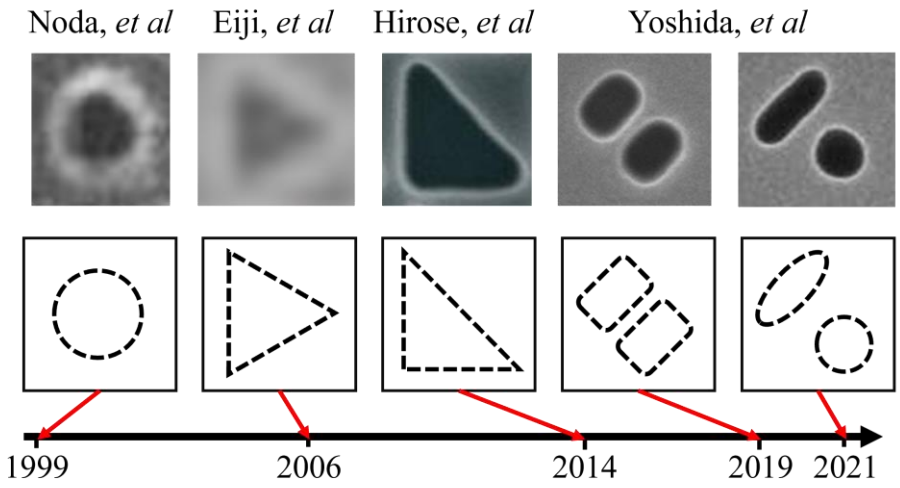

Figure 2.12: Schematic of the evolution of PC pattern shape. [1-5]

Figure 2.12 shows a schematic of the evolution of the PC pattern shape from the creation of PCSEL to the most recent record-breaking devices. [56-60] It can be observed that throughout the evolution of PCSELs, the photonic crystal shape has progressed from circles to equilateral triangles, then to right triangles, and now to double lattice structures, with each major shift occurring roughly every five years. In all case, simulation begins at the PC shape and proceeds to the device level in a similar development process.

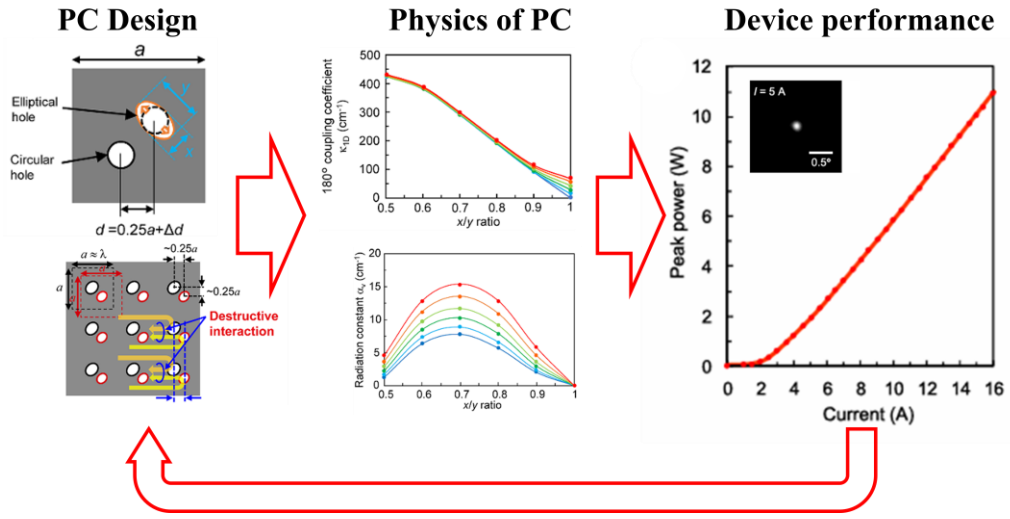

Figure 2.13: Schematic of the conventional PCSEL develop process. [4, 5]

Figure 2.13 shows a schematic representation of the conventional development process of the PCSEL. It starts from the design of the PC pattern shape, including the pattern and background materials, the shape of PC, and fill factor of the pattern. The PC is then physically analysed by simulation methods to make sure the optical property matches the active region and epitaxy

structure. Then the device is fabricated and characterized to see the real performance. At last, analysis the characterization results as a feedback to improve the design of the PC design.

One disadvantage that can be noticed from this process is that the analysis of effects is based only on the iterative design changes of the PC (e.g. a new shape of pattern). Generally, the ideas for PC modification come from the feedback from previous series of devices. How an ideal PC may operate or control the light scattering is not considered. Meanwhile, the fabrication period of PCSEL is relatively longer than other classes of semiconductor lasers. These two have combined to make progress comparatively slow, when we consider Fig 2.12.

To solve this problem, a simple method to link the microscopic coupling coefficients (PC light scattering effects) with macroscopic laser losses is needed. [61-64] With such a model, the development process can be changed. A schematic is shown in figure 2.14 to explain this new process. The model described in this thesis is able to arbitrarily change the value of coupling coefficients or add new structures to the PCSEL device. With this approach, if the predicted result is suitable, this could focus PC fabrication on those targeted scattering parameters. With such a design process, the effect of the PC on light scattering is key, with this new model exploring these effects by linking the microscopic coupling coefficients with macroscopic device-level losses. This is done to guide the direction of research in a more rapid and sustainable manner. Whilst any scattering coefficients can be imagined and implemented, the work here is grounded by using starting values originally extracted from simulation or measurement. These values may then be arbitrarily adjusted when exploring the effects. In the end ideal scattering parameters may then be deduced and an ideal PC structure to deliver these parameters considered. The physical design of the PCSEL device configuration can also be readily explored in the model developed here. Arbitrary gain and loss regions, perimeter reflectors, may be introduced to quickly explore new device functionality.

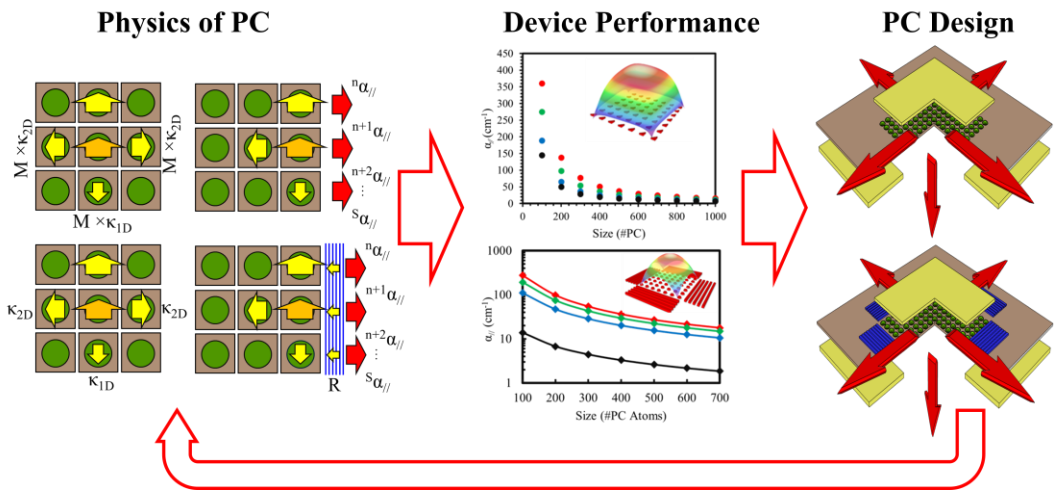

Figure 2.14: Schematic of PCSEL develop process involving PMC model.

To achieve this, a probabilistic Markov chain (PMC) model has been developed and is discussed in chapter 3. The PMC model is based on a Markov chain model, along with a statistic method, to create a link between microscopic input parameters of the PCSEL and in turn determine device-level loss. The input parameters for the PMC model can be obtained from simulation (e.g. PWE or FDTD) or measurement (e.g. band-structure measurement), and arbitrarily adjusted based on those initial reasonable values. The simulation logic and algorithm of the PMC model is discussed in detail in chapter 3. To reach a balance between accuracy and program runtime, a convergence criteria is discussed and set to 0.1 cm^{-1} (details discussed in chapter 3). Finally, two InP-based PCSEL devices are predicted and compared by PMC model in terms of their threshold gains and slope efficiencies. The two devices used for the validation have identical PC regions, but differ in the presence/absence of in-plane boundary mirrors. The predicted results are in excellent agreement with measured results.

With the PMC method, the design of a GaAs based PCSEL is discussed in chapter 4. This design considers a uniform PC region with uniform coupling coefficients (the whole of the PC region is in gain, surrounded by a perfectly absorbing boundary). The effect of varying the coupling coefficients on in-plane loss of PCSEL is then discussed. Then the effect of perimeter mirrors with various reflectivity on in-plane loss is discussed. Further exploration is performed by introducing a spatial variation of the perimeter mirror reflectivity on in-plane loss and near-field pattern. In support of the design and realisation of a Resonator Embedded PCSEL, InP-based PCSEL with low coupling coefficients are simulated with and without in-plane mirrors. Finally, the PMC method is once more validated.

Chapter 5 explores another commonly used design of PCSEL, where an unpumped PC

boundary is used to minimise parasitic in-plane power loss a//. Self-absorption in the unpumped boundary quantum is considered for the first time. A current spreading simulation is caried out and shows that current spreading occurs over a much smaller range than optical power spreading, and is subsequently ignored. Then, the effect of unpumped region on PCSEL parasitic losses is discussed. Finally, comparison to GaAs-based double lattice PCSELs and GaN-based PCSELs from the literature is carried out.

References

[1]. A. Ashkin, J. M. Dziedzic, and T. Yamane, "Optical trapping and manipulation of single cells using infrared laser beams," Nature, vol. 330, no. 6150, p. 769, 1987.

[2]. D. Kim, M. Pelusi, Z. Ahmed, D. Novak, H.-F. Liu, and Y. Ogawa, "Ultrastable millimetre-wave signal generation using hybrid modelocking of a monolithic DBR laser," Electronics Letters, vol. 31, no. 9, pp. 733-734, 1995.

[3]. E. Widmann et al., "Hyperfine structure of antiprotonic helium revealed by a laser-microwave-laser resonance method," Physical review letters, vol. 89, no. 24, p. 243402, 2002.

[4]. L. Johnson and H. Guggenheim, "InfraredPumped Visible Laser," Applied Physics Letters, vol. 19, no. 2, pp. 44-47, 1971.

[5]. Z. Tang et al., "Room-temperature ultraviolet laser emission from self-assembled ZnO microcrystallite thin films," Applied Physics Letters, vol. 72, no. 25, pp. 3270-3272, 1998.

[6]. M. Rosen et al., "Exploding-foil technique for achieving a soft x-ray laser," Physical review letters, vol. 54, no. 2, p. 106, 1985.

[7]. Coldren, L.A., Corzine, S.W. and Mašanović, M.L. (2012). Dynamic Effects. In Diode Lasers and Photonic Integrated Circuits (eds L.A. Coldren, S.W. Corzine and M.L. Mašanović). https://doi.org/10.1002/9781118148167.ch5

[8]. Koch, T. L., & Bowers, J. E. (1984). Nature of wavelength chirping in directly modulated semiconductor lasers. Electronics Letters, 20, 1038-1040. https://doi.org/10.1049/el:19840709

[9]. P. Crump, S. Böldicke, C. M. Schultz, H. Ekhteraei, H. Wenzel, and G. Erbert, “Experimental and theoretical analysis of the dominant lateral waveguiding mech anism in 975nmhighpowerbroadarea diode lasers,” Semicond. Sci. Technol. 27, 045001 (2012).

[10]. C. J. Chang-Hasnain, M. Orenstein, A. Von Lehmen, L. T. Florez, J. P. Harbison, and N. G. Stoffel, “Transverse mode characteristics of vertical cavity surface emitting lasers,” Appl. Phys. Lett. 57, 218–220 (1990).

[11]. M. Winterfeldt, P. Crump, H. Wenzel, G. Erbert, and G. Tränkle, “Experimental investigation of factors limiting slow axis beam quality in 9xx nm high power broad area diode lasers,” J. Appl. Phys. 116, 063103 (2014). 4.

[12]. S. Rauch, H. Wenzel, M. Radziunas, M. Haas, G. Tränkle, and H. Zimer, “Impact of

longitudinal refractive index change on the near-field width of high-power broad-area diode lasers," Appl. Phys. Lett. 110, 263504 (2017).

[13]. M. Imada et al., "Coherent two-dimensional lasing action in surface-emitting laser with triangular-lattice photonic crystal structure," Appl. Phys. Lett., vol. 75, no. 3, pp. 316–318, Jul. 1999.

[14]. M. Meier, A. Mekis, A. Dodabalapur, A. Timko, R. E. Slusher, J. D. Joannopoulos, and O. Nalamasu, "Laser action from two-dimensional distributed feedback in photonic crystals," Appl. Phys. Lett. 74, 7–9 (1999).

[15]. L. A. Coldren, S. W. Corzine, and M. L. Mašanović, Diode Lasers and Photonic Integrated Circuits. Wiley, 2012. doi: 10.1002/9781118148167.

[16]. L. Hargrove, R. L. Fork, and M. Pollack, "Locking of HeNe laser modes induced by synchronous intracavity modulation," Applied Physics Letters, vol. 5, no. 1, pp. 4-5, 1964.

[17]. D. Pohl, "Operation of a ruby laser in the purely transverse electric mode TE01," Applied Physics Letters, vol. 20, no. 7, pp. 266-267, 1972.

[18]. G. H. B. Thompson, "Physics of semiconductor laser devices," Chichester, Sussex, England and New York, Wiley-Interscience, 1980. 572 p., 1980.

[19]. L. Rayleigh, "XVII. On the maintenance of vibrations by forces of double frequency, and on the propagation of waves through a medium endowed with a periodic structure," The London, Edinburgh, and Dublin Philosophical Magazine and Journal of Science, vol. 24, no. 147, pp. 145-159, 1887.

[20]. F. Bloch, "Über die quantenmechanik der elektronen in kristallgittern," Zeitschrift für physik, vol. 52, no. 7-8, pp. 555-600, 1929.

[21]. M. Imada et al., "Coherent two-dimensional lasing action in surface-emitting laser with triangular-lattice photonic crystal structure," *Appl. Phys. Lett.*, vol. 75, no. 3, pp. 316–318, Jul. 1999.

[22]. M. Meier, A. Mekis, A. Dodabalapur, A. Timko, R. E. Slusher, J. D. Joannopoulos, and O. Nalamasu, "Laser action from two-dimensional distributed feedback in photonic crystals," Appl. Phys. Lett. 74, 7–9 (1999).

[23]. T. Sakai and S. Noda, "Coupled-wave theory for photonic crystal waveguides," *Opt. Express*, vol. 14, no. 20, pp. 9460-9466, 2006.

[24]. T. Sakai, E. Miyai, and S. Noda, "Coupled-wave model for square-lattice photonic crystal lasers with transverse-electric polarization," *IEEE J. Quantum Electron.*, vol. 43, no. 11, pp. 1179-1186, 2007.

[25]. Y. Liang, C. Peng, K. Ishizaki et al., "Three-dimensional coupled-wave analysis for triangular-lattice photonic-crystal surface-emitting lasers with transverse-electric polarization," Opt. Express, vol. 21, no. 1, pp. 565–580, 2013, doi: 10.1364/OE.21.000565.

[26]. R. J. E. Taylor, "Chapter 2, Band Structure modelling" Design of Photonic Crystal Surface Emitting Lasers and the Realisation of Coherently Coupled Arrays, Department of Electronic and Electrical Engineering, University of Sheffield, Sheffield, UK, 2015, pp. 42-69.

[27]. R. W. Ziolkowski, J. M. Arnold, and D. M. Gogny, "Ultrafast pulse interactions with two-level atoms," *Phys. Rev. A*, vol. 52, no. 4, pp. 3082–3094, 1995.

[28]. A. S. Nagra and R. A. York, "FDTD analysis of wave propagation in nonlinear absorbing and gain media," *IEEE Trans. Antennas Propag.*, vol. 46, no. 3, pp. 334–340, 1998.

[29]. S.-H. Chang and A. Taflove, "Finite-difference time-domain model of lasing action in a four-level two-electron atomic system," *Opt. Express*, vol. 12, no. 16, pp. 3827–3833, 2004.

[30]. Y. Huang and S.-T. Ho, "Computational model of solid-state, molecular, or atomic media for FDTD simulation based on a multi-level multi-electron system governed by Pauli exclusion and Fermi–Dirac thermalization with application to semiconductor photonics," *Opt. Express*, vol. 14, no. 8, pp. 3569–3587, 2006.

[31]. P. Bermel, E. Lidorikis, Y. Fink, and J. D. Joannopoulos, "Active materials embedded in photonic crystals and coupled to electromagnetic radiation," *Phys. Rev. B*, vol. 73, p. 165125, 2006.

[32]. K. S. Yee, "Numerical solution of initial boundary value problems involving Maxwell's equations in isotropic media," *IEEE Trans. Antennas Propag.*, vol. 14, no. 3, pp. 302–307, 1966.

[33]. A. Taflove and S. C. Hagness, *Computational Electrodynamics: The Finite-Difference Time-Domain Method*, 3rd ed. Norwood, MA: Artech, 2005.

[34]. J. D. Joannopoulos, S. G. Johnson, R. D. Meade, and J. N. Winn, *Photonic Crystals: Molding the Flow of Light*, 2nd ed. Princeton, NJ: Princeton Univ. Press, 2008.

[35]. Design of photonic-crystal surface-emitting lasers with enhanced in-plane optical feedback for high-speed operation

[36]. S. Noda *et al.*, “High-power and high-beam-quality photonic-crystal surface-emitting lasers: A tutorial,” *Adv. Opt. Photon.*, vol. 15, no. 4, pp. 977–1032, 2023, doi: 10.1364/AOP.502863.

[37]. A. F. Oskooi et al., "MEEP: A flexible free-software package for electromagnetic simulations by the FDTD method," *Comput. Phys. Commun.*, vol. 181, no. 3, pp. 687–702, 2010

[38]. M. Plihal and A. A. Maradudin, "Photonic band structure of two-dimensional systems: The triangular lattice," Phys. Rev. B, vol. 44, pp. 8565–8571, 1991.

[39]. S. Shi, C. Chen, and D. W. Prather, "Plane-wave expansion method for calculating band structure of photonic crystal slabs with perfectly matched layers," J. Opt. Soc. Am. A, vol. 21, pp. 1769–1775, 2004.

[40]. M. Imada, A. Chutinan, S. Noda, and M. Mochizuki, "Multidirectionally distributed feedback photonic crystal lasers," Phys. Rev. B, vol. 65, p. 195306, Apr. 2002.

[41]. M. Imada et al., "Coherent two-dimensional lasing action in surface-emitting laser with triangular-lattice photonic crystal structure," Appl. Phys. Lett., vol. 75, no. 3, pp. 316–318, Jul. 1999.

[42]. S. Noda *et al.*, “High-power and high-beam-quality photonic-crystal surface-emitting lasers: A tutorial,” *Adv. Opt. Photon.*, vol. 15, no. 4, pp. 977–1032, 2023, doi: 10.1364/AOP.502863.

[43]. H. Kogelnik and C. V. Shank, "Coupled-wave theory of distributed feedback lasers," *J. Appl. Phys.*, vol. 43, no. 5, pp. 2327–2335, 1972.

[44]. M. Toda, "Proposed cross grating single-mode DFB laser," *IEEE J. Quantum Electron.*, vol. 28, no. 6, pp. 1653–1662, 1992.

[45]. K. Sakai, E. Miyai, and S. Noda, "Coupled-wave model for square-lattice two-dimensional photonic crystal with transverse-electric-like mode," *Appl. Phys. Lett.*, vol. 89, no. 2, p. 021101, 2006.

[46]. K. Sakai, E. Miyai, and S. Noda, "Coupled-wave theory for square-lattice photonic crystal lasers with TE polarization," *IEEE J. Quantum Electron.*, vol. 46, no. 6, pp. 788–795, 2010.

[47]. Y. Liang et al., "Three-dimensional coupled-wave model for square-lattice photonic crystal lasers with transverse electric polarization: a general approach," *Phys. Rev. B*, vol. 84, no. 19, p. 195119, 2011.

[48]. Y. Liang et al., "Three-dimensional coupled-wave analysis for square-lattice photonic crystal surface emitting lasers with transverse-electric polarization: finite-size effects," *Opt. Express*, vol. 20, no. 14, pp. 15945–15961, 2012.

[49]. Y. Liang et al., "Three-dimensional coupled-wave analysis for triangular-lattice photonic-crystal surface-emitting lasers with transverse-electric polarization," *Opt. Express*, vol. 21, no. 1, pp. 565–580, 2013.

[50]. Y. Yang et al., "Three-dimensional coupled wave theory for the guided mode resonance in photonic crystal slabs: TM-like polarization," *Opt. Lett.*, vol. 39, no. 15, pp. 4498–4501, 2014.

[51]. T. Inoue et al., "Comprehensive analysis of photonic-crystal surface-emitting lasers via time-dependent three-dimensional coupled-wave theory," *Phys. Rev. B*, vol. 99, no. 3, p. 035308, 2019.

[52]. S. Katsuno et al., "Self-consistent analysis of photonic-crystal surface-emitting lasers under continuous wave operation," *Opt. Express*, vol. 29, no. 16, pp. 25118–25132, 2021.

[53]. K. Hirose et al., "Watt-class high-power, high-beam-quality photonic-crystal lasers," *Nature Photon.*, vol. 8, pp. 406–411, 2014.

[54]. K. Emoto et al., "Wide-bandgap GaN-based watt-class photonic-crystal lasers," *Commun. Mater.*, vol. 3, p. 72, 2022.

[55]. M. Yoshida et al., "High-brightness scalable continuous-wave single-mode photonic-crystal laser," *Nature*, vol. 618, pp. 727–732, 2023.

[56]. S. Noda *et al.*, “High-power and high-beam-quality photonic-crystal surface-emitting lasers: A tutorial,” *Adv. Opt. Photon.*, vol. 15, no. 4, pp. 977–1032, 2023, doi: 10.1364/AOP.502863.

[57]. E. Miyai, K. Sakai, T. Okano, and T. Baba, "Lasers producing tailored beams," *Nature*, vol. 441, p. 946, 2006, doi: 10.1038/441946a.

[58]. K. Hirose et al., "Watt-class high-power, high-beam-quality photonic-crystal lasers," *Nature Photon.*, vol. 8, pp. 406–411, 2014.

[59]. M. Yoshida, M. De Zoysa, K. Ishizaki et al., "Double-lattice photonic-crystal resonators enabling high-brightness semiconductor lasers with symmetric narrow-divergence beams," *Nature Mater.*, vol. 18, pp. 121-128, 2019.

[60]. M. Yoshida, M. De Zoysa, K. Ishizaki et al., “Double-lattice photonic-crystal resonators enabling high-brightness semiconductor lasers with symmetric narrow-divergence beams,” J. Phys. Photonics, vol. 3, no. 2, 2021, Art. no. 022006, doi: 10.1088/2515-7647/abea06.

[61]. J. Liu, Y. Gao, P. Ivanov, P. Harvey, and R. Hogg, "Probabilistic Markov chain modeling of photonic crystal surface emitting lasers," *Appl. Phys. Lett.*, vol. 123, no. 26, p. 261107, Dec. 2023, doi: 10.1063/5.0168073.

[62]. J. Liu, X. Zhao, Z. Bian, P. Harvey, S. Watson, S. J. Sweeney, and R. A. Hogg, "Interdependence of parasitic losses in photonic crystal surface emitting lasers," *AIP Advances*, vol. 15, no. 4, p. 045321, Apr. 2025, doi: 10.1063/5.0252646.

[63]. J. Liu, Z. Bian, X. Zhao, S. J. Sweeney, and R. A. Hogg, "Optimization of pumping geometry of photonic crystal surface emitting lasers," in *Proc. SPIE Phys. Simul. Optoelectron. Devices XXXIII*, vol. 13360, Mar. 2025, Art. no. 1336004, doi: 10.1117/12.3042883.

[64]. J. Liu, D. Kim, Z. Bian, J. Feng, Y. Gao, and R. A. Hogg, "Convergence criteria for Markov chain modelling of photonic crystal surface emitting lasers," in *Proc. SPIE Photonics West*, 2023, doi: 10.1117/12.2649077.

Chapter 3: Probabilistic Markov Chain Model

3.1 Introduction

In this chapter, a probabilistic Markov chain (PMC) model of photonic crystal surface emitting lasers (PCSELs) is introduced [1]. The model incorporates microscopic input parameters (the in-plane coupling coefficients and those related to radiative and parasitic internal loss) and determines macroscopic device-level PCSEL parameters such as in-plane optical loss (allowing slope efficiency and threshold gain to be deduced) and the near-field profile. The simulation logic and algorithm of the PMC model are discussed and detailed. The model describes the optical power travelling in different directions at each PC atom as the states of a Markov chain, the probabilities of power transfer (scattering probability) between any two states are calculated from the coupling coefficients. Whilst ideally, the PMC model would be allowed to run for an infinite amount of time, the number of simulation iterations must be made finite. The conditions for terminating the simulation process and extracting data (termed convergence) are laid out [2]. With convergence established, validation with experimental results from real devices, a resonator embedded PCSEL and a normal design PCSEL, are described and discussed.

3.2 Macroscopic Losses and Microscopic Scattering of PCSEL Device

The probabilistic Markov chain (PMC) model is not an *ab initio* simulator. [3]. Unlike most other PCSEL simulators it does not solve Maxwell's equations for the given periodic structure, and determine microscopic and possibly determine macroscopic parameters (in the case of 3D CWT of finite sized devices [4-6]). Rather, it bridges the gap between microscopic scattering and macroscopic device level losses. Starting from known or imagined photonic crystal coupling coefficients, device level PCSEL losses are calculated. The PC coupling coefficients are described in cm^{-1} units. In the PMC model, these are converted into probabilities (termed scattering coefficients, P) of photons changing their direction of travel in the plane of the PC, and their chance of scattering vertically to the lasing mode or being lost to internal optical loss within the device. Figure 3.1 (a) shows a schematic of light scattering mechanism among PC atoms (red dots), the black arrow is an example of original direction of light, the yellow arrows representing the direction of scattered light. $\kappa_{\perp}$ representing the total scattered light to the vertical directions (upwards and downwards); κ_{1D} represents light scattered into the counter-propagating 180° in-plane direction; κ_{2D} represents light scattered into the orthogonal in-plane directions (left or right); κ_i represents internal absorption of light (not shown in figure 3.1);

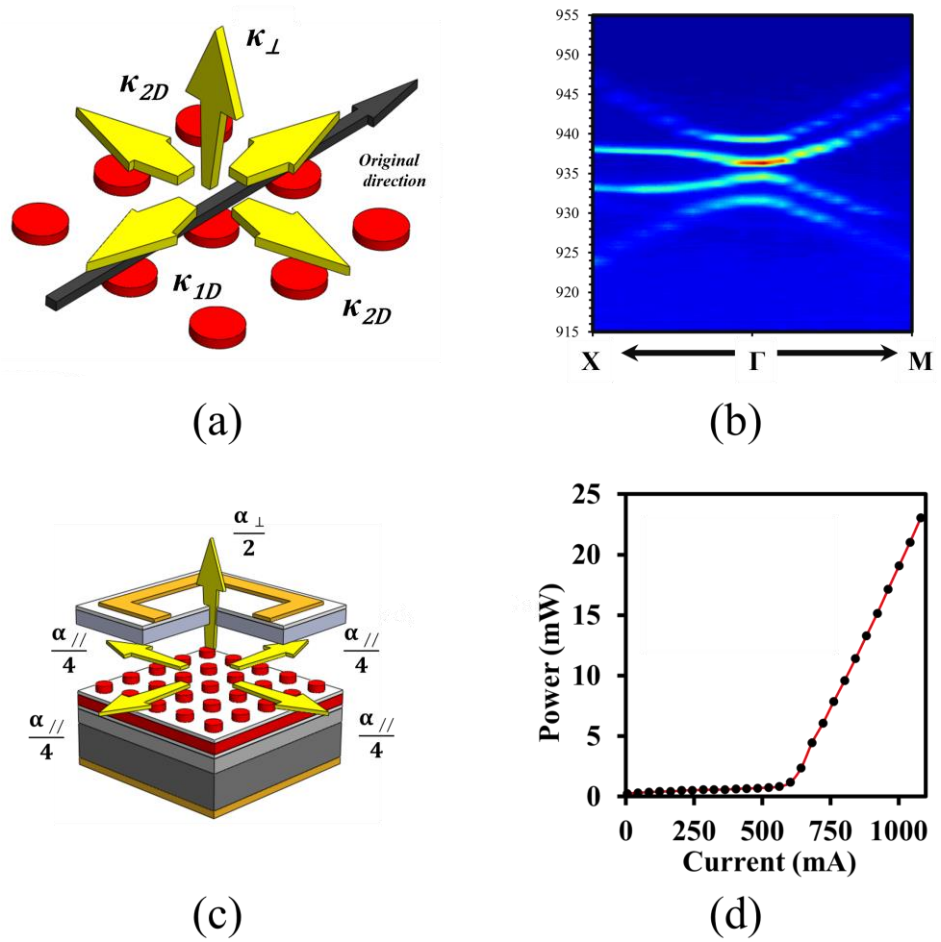

Figure 3.1: (a) schematic of microscopic light scattering mechanism among PC atoms. (b) change this one to a measured band structure (c) schematic of macroscopic device-level loss mechanism of a PCSEL. (d) measured light and current (LI) curve.

$\kappa_{forward}$ represents the situation when light keeps the same direction as original direction which is defined as:

$$\kappa_{forward} = 1 - \kappa_{1D} - 2 \times \kappa_{2D} - \kappa_{\perp} - \kappa_i \qquad equation3.1$$

The scattering coefficients can be deduced either by extraction from experimental measurement (e.g. a measured band-structure [7,8], shown in figure 3.1 (b), or other simulations (e.g. FDTD) [9-12] as described previously.

Figure 3.1 (c) shows a schematic of macroscopic device-level loss mechanisms (yellow arrows) of a PCSEL device as described previously. The threshold gain, g_{th}, of the laser follows the equation:

$$g_{th} = \alpha_{//} + \alpha_{\perp} + \alpha_i \qquad equation3.2$$

Where $\alpha_{//}$ is in-plane loss, which can be assumed to have equal values on the four edges of a square PC matrix. It is not easy to experimentally measure $\alpha_{//}$ (to the best of my knowledge it

has never been measured) so $\alpha_{//}$ is a useful output of this simulator.

Experimentally, the slope efficiency and threshold current can be easily extracted from experimental measurements, e.g. figure 3.1 (d) shows a measured light-current (LI) curve from which a threshold current and slope efficiency are deduced (described previously). From this, the current density can provide threshold gain, if the J-G characteristics of the active material are known, and the extraction of operating parameters (internal efficiency, reflectivity, mirror phase) can occur if some of the losses can be assumed, an example will be shown in later chapter However, experimental determination of the macroscopic losses is difficult in PCSELs.

3.3 Probabilistic Markov Chain PCSEL Model

A probabilistic Markov chain model is a stochastic process. It describes a sequence of events in which the probability of each event depends only on the state attained in the previous event [13-15]. In the PMC model the scattering mechanism of optical power in finite size PCSEL devices is described by the coupling coefficients (κ_{1D}, κ_{2D}, $\kappa_{\perp}$, and κ_i), which physically describe the mutual coupling among fundamental Bloch waves inside of a square lattice PCSEL [8,9,12].

		Scattered direction				
		North	South	West	East	Vertical
Injecting direction	North	$P_{forward}$	P_{1D}	P_{2D}	P_{2D}	$P_{\perp}$
	South	P_{1D}	$P_{forward}$	P_{2D}	P_{2D}	$P_{\perp}$
	West	P_{2D}	P_{2D}	$P_{forward}$	P_{1D}	$P_{\perp}$
	East	P_{2D}	P_{2D}	P_{1D}	$P_{forward}$	$P_{\perp}$

Table 3.1: State transition form of the PMC model

Statistically, these coupling coefficients describe the probabilities of optical power being scattered to different directions. In the PMC model, we consider only the scattering of optical power between these “cardinal” directions. PWE, and CWT utilise higher order scattering in their calculations, but this is not the case in this model. The states of the transmitted power are limited [13-15]. Table 3.1 shows the state transition form of the PMC model. The states are defined and named by the in-plane cardinal directions which are based on the target PC atom, which is the processing element in the program. The injection direction represents the directions of optical power that interacts with a given target PC atom. The scattered direction

is the direction of light leaving the target PC atom. The state transition probabilities linking any two states are represented by scattering coefficients, P, which are calculated from the coupling coefficients, κ.

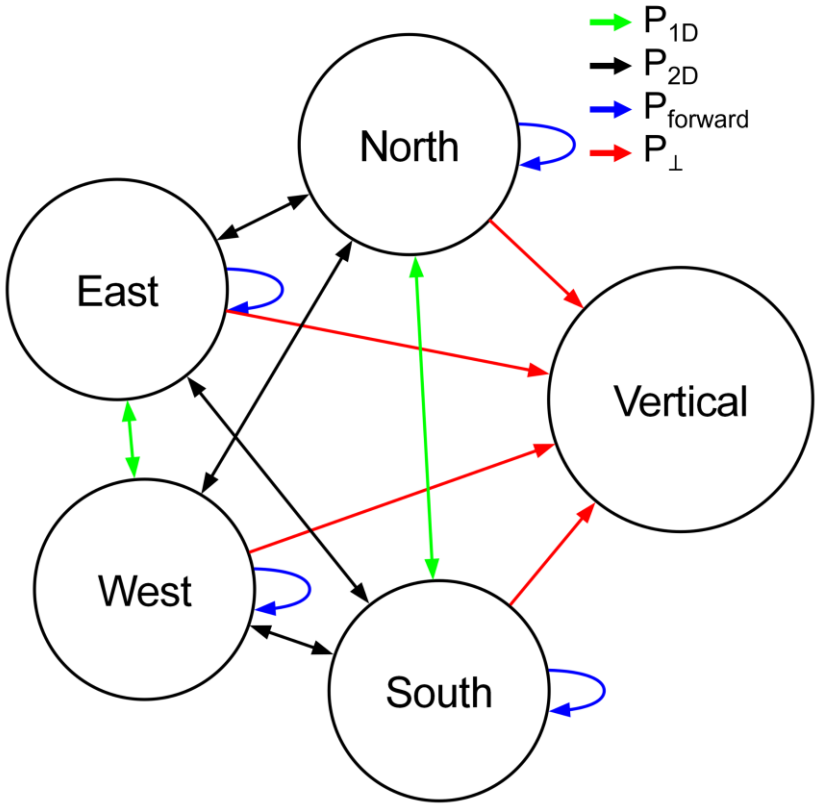

Figure 3.2: Schematic state transition diagram of the PCSEL probabilistic Markov chain model

For optical powers propagating in a given direction, the transmission state solely depends on the current state. The transition process of the optical power can be infinite but the state, S, of it is limited as described by (also in table 3.1):

$$S = North, South, East, West, Vertical \qquad equation 3.3$$

Figure 3.2 is a schematic of the state transition diagram of table 3.1, the arrows show the transition directions (governed by probabilities, P) between states distinguished by colours, green arrows represent P_{1D}; black arrows represent P_{2D}; blue arrows represent $P_{forward}$; red arrows represent $P_{\perp}$. In PMC model, the value of same scattering coefficient is assumed to be constant on whole PC region. Optical power that is scattered to vertical direction, exits the PC region from in-plane edges, or is lost to internal loss are considered to be contributing to $\alpha_{\perp}$, $\alpha_{//}$, or α_i, respectively.

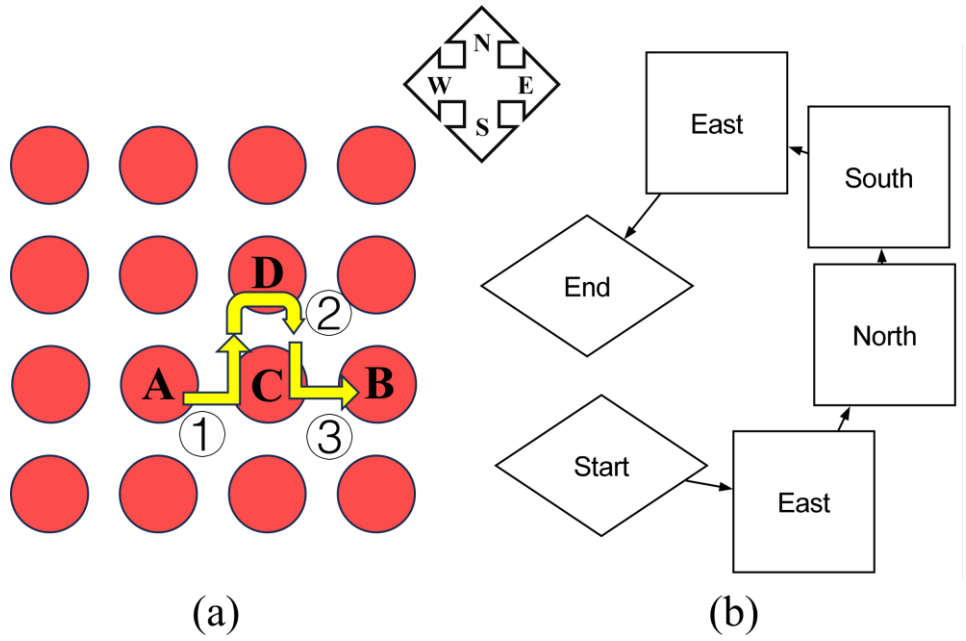

Figure 3.3 (a) an example path of light traveling among PC atoms, assuming the original light emitted in-plane from atom A and stops eventually at atom B. (b) the flow chart of the Markov chain in (a)

An example of a simplified, illustrative in-plane path of a given lasing photon, emitted from PC atom A (towards east) to atom B (arrives from east) is shown in figure 3.3 (a). The example path given is not the shortest nor most complex path but a representative path and is divided into three steps. ① is original photon hits atom C and is scattered north; ② is the photon leaving atom C in a northerly direction to interact with atom D and is scattered to south; ③ is the photon interacting with atom C and being scattered to the east, finally arriving at B. Figure 3.3 (b) is the state transition flow chart of the example path given in figure 3.3 (a). The original optical power is from atom A to east, and scattered north at atom C, then return to C from atom D, finally arriving at atom B from atom C. The probability of this path occurring for a given easterly travelling photon at A is:

$$P = 100\% * P_{forward} * P_{2D} * P_{1D} * P_{2D} \qquad equation 3.4$$

Whilst the previous paragraph illustrates the path of a given photon, due to the high photon numbers at play in a laser the PMC model can consider optical power in the state transition flow chart.

In the PMC model, the PC atom is used as the calculation element, so each has the same length. This brings about the time-step unit that is utilised, that is the time for light to travel from one atom to another. As the period is dimensionless, so the time-step is dimensionless.

Figure 3.4 is a flow chart of the simulation arithmetic of the PMC model. The algorithm of the

PMC model contains two basic parts, the scattering model which simulates the mechanism of

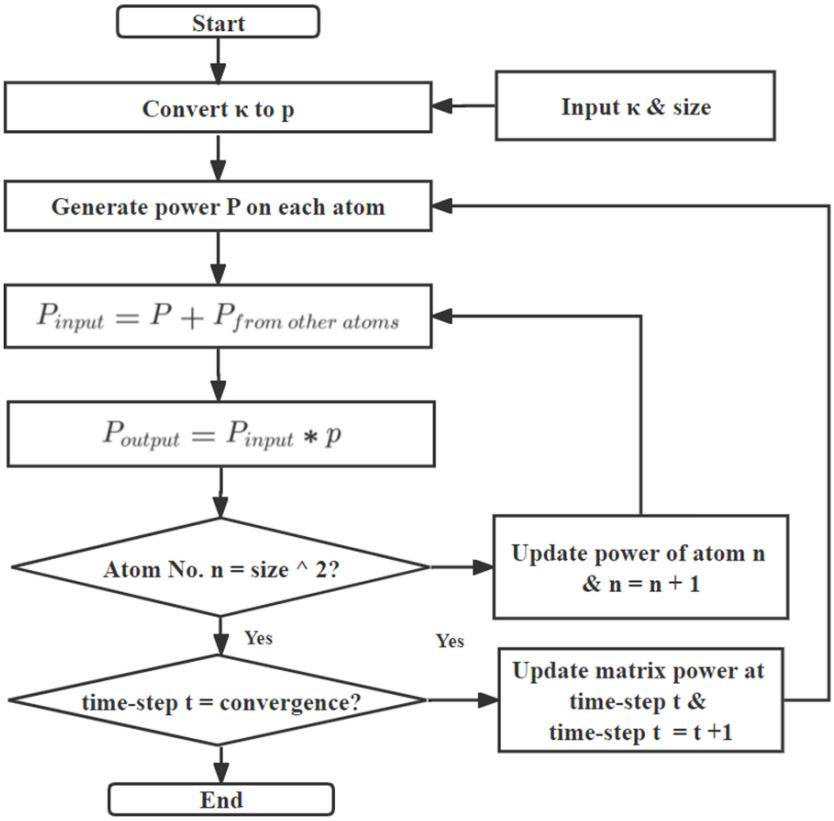

Figure 3.4 flow chart of algorithm of PMC model.

optical power propagating among PC atoms at each time-step, and the process by which the simulation is terminated (i.e. when convergence is reached, details are discussed later). The time-step is defined in equation 3.5:

$$Time - step = \frac{a}{Vg} \qquad equation 3.5$$

Where V_g is the speed of light in the semiconductor; a is the lattice constant (the period of the PC). Firstly, before the time count starts, the microscopic parameters, e.g. coupling coefficients provided in units of cm^{-1}, details of PC region to be simulated (size of PC region and lattice constant a) are set. The coupling coefficient κ is converted from cm^{-1} to the fractional probability (scattering coefficient) P of optical power is generated at each PC atoms. (An example of calculation is provided in Appendix A) At each time-step, 1 unit of optical power generated at each PC atom, with received optical power of the previous time-step from neighbouring PC atoms summed as the total input power (for a given direction) for the target PC atom. Then, before moving to next time-step, the output power is made the input power for the next time-step, and the PC matrix information is updated. The process is repeated at each

time-step and terminated at the specific time-step determined by the convergence criteria.

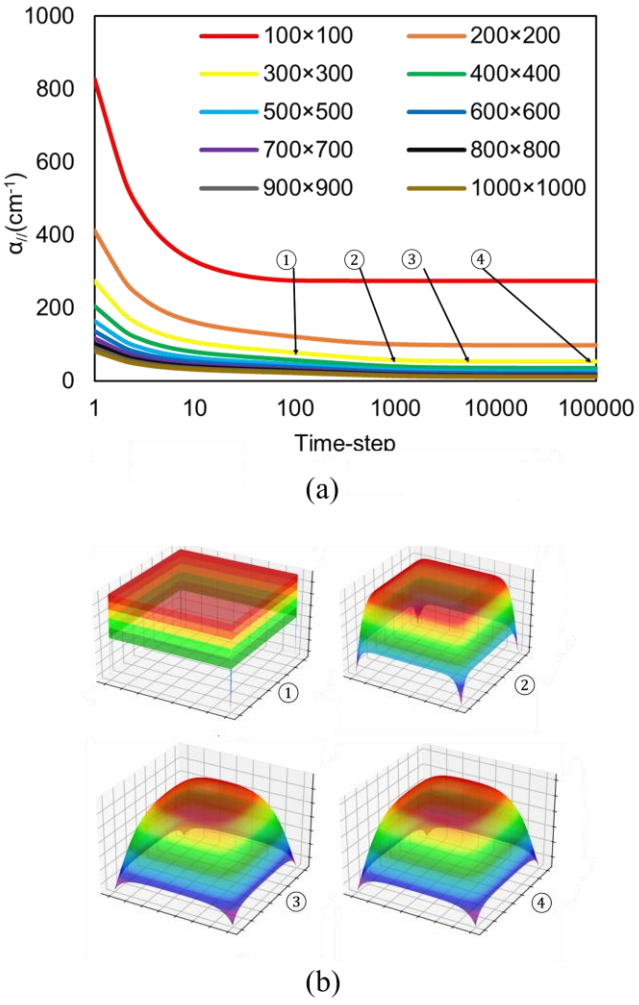

Figure 3.5 (a) the simulated in-plane loss of different size of PCSEL devices (from 100 #PC to 1000 #PC area) as a function of time-step. (b) the simulated nearfield of 700 #PC size device in ① 100 time-steps ② 1000 time-steps ③ 10000 time-steps ④ 100000 time-steps.

3.4 Convergence Criteria of PMC Model

As time-step is incremented, power is continually added to the device, is transferred between PC atoms, and eventually lost through the edge, though surface emission or through internal loss. In the PMC model, the power lost through the edge of device is described as in-plane loss. The surface emission describes the out-of-plane loss, which can be assumed to be evenly divided to half upward and half downward, here the value of out-of-plane loss from the simulator is the total value. Internal loss has its usual meaning, and represents power loss to absorption, and scattering out of the mode.

The simulations are terminated, and results obtained at a time-step where convergence is

obtained. The satisfaction of "convergence" is based on the accuracy required for the calculated in-plane loss. It is noted that most of the existing work on PCSELs uses whole reciprocal centimetres (cm^{-1}) to describe the device-level loss, such as threshold gain, mirror loss and internal loss [10,16-28]. Therefore, in this work, the convergence limit is set to be within ±0.1 cm^{-1}. However, this can be changed according to specific requirements.

Figure 3.5 (a) shows a plot of the in-plane loss from a given square PCSEL device as a function of simulation time-step. A 100×100 period device is referred to as 100 #PC, 200×200 period device is referred to as 200 #PC, and so on. The input parameters to the simulation are κ_{1D} = 1334 cm^{-1}, κ_{2D} = 386 cm^{-1} (extracted from the reported band-structure) and $\kappa_{\perp}$ = 38 cm^{-1}, κ_i = 5 cm^{-1} (reported in literature). [10] The value of $\alpha_{//}$ is unchanged for a given device size at very long time-steps.

Figure 3.5 (b) shows the simulated normalized nearfield patterns of 700 #PC PCSEL at different time-steps. There are obvious differences among nearfields at 100, 1000 and 10000 time-step. (figure 3.5 (a) ①, ② and ③) However, the difference (in shape of mode) is almost undetectable by eye after 10000 time-step, which can be a qualitative confirmation of convergence having been reached.

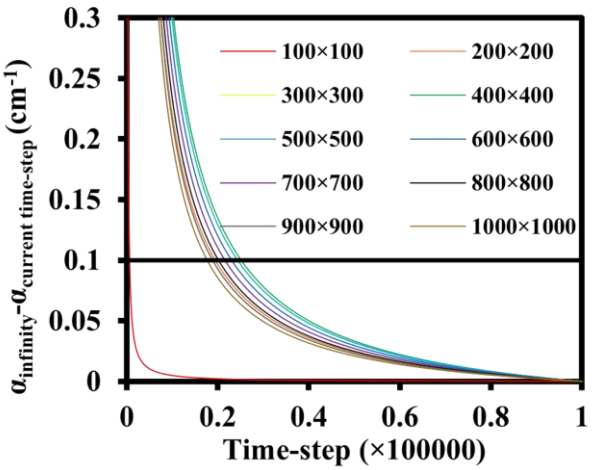

Figure 3.6 the difference between simulated loss at current time-step and infinity as a function of time-step.

As suggested in figure 3.5, the convergence can be reached by running the simulator to very high values of time-step. Computing power, and device parameters can have a significant effect on the run time of the program, and essentially how long we wait to say "infinity" has been reached. A residual value described is defined as:

$$\left|\left|r^{(k)}\right|\right| < \varepsilon = \alpha_{infinity} - \alpha_{current\ time\ step} \qquad equation 3.6$$

r(k) is the residual vector, ε is the convergence threshold based on the convergence limit of chosen. ε is set at 0.1 cm^{-1}. $\alpha_{infinity}$ is defined as the in-plane loss of the device at very long time-step and physically represents the simulated PCSEL device operating stably. For the 10 PCSEL devices considered in this commissioning work, the time-step of $\alpha_{infinity}$ is set at 100000 time-steps. $\alpha_{current\ time\text{-}step}$ is the real-time calculated in-plane loss in PMC model at each time-step.

Figure 3.6 shows the calculated ε using the aforementioned input parameters as a function of time-step. It can be seen from the figure that most of the devices will reach convergence threshold at ~20000-30000 time-steps.

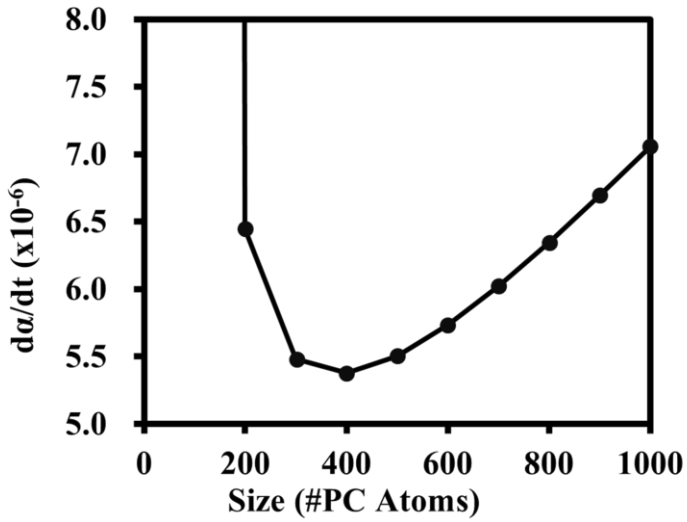

Figure 3.7 The slope coefficient of in-plane loss at 0.1 cm^{-1} as a function of size of PCSEL devices.

Figure 3.7 plots the relative change of in-plane loss between time-steps as a function of size of simulated PCSEL devices at the time-step that 0.1 cm^{-1} accuracy has been achieved for that device. This allows a different choice for the termination of simulation to reduce simulation time. From figure 3.6, one may consider running all simulations to 30000 time-steps. But this would be wasteful of resources. Figure 3.7 allows us to consider a differential between time-steps to terminate the simulation.

It can be observed from the figure 3.6 and 3.7 that, for smaller size PCSEL devices, the convergence can be reached much sooner, that may be due to the ratio of the cavity length (size of PCSEL device in this case) and scattering coefficient values (κ_{1D} and κ_{2D}). For devices larger than 400 #PC, the convergence threshold can be regarded as a linear function of time-step. As shown in figure 3.7, for arbitrary size, the convergence threshold can be reached when da/dt is less than ~5×10^{-6} cm^{-1}. So, the loss condition of any device with provided input parameters

and reasonable size can be simulated or predicted in PMC model within the chosen accuracy in a sustainable (not wasteful) period of time as possible.

3.5 Validation – PCSEL and REPCSEL

As part of this PhD work, a resonator embedded photonic crystal surface emitting laser (REPCSEL) has been realised [29]. As compared with a normal PCSEL (a schematic has been shown in inset of figure 3.8 (a)), the photonic crystal region of a REPCSEL is surrounded by a 1st order DBR mirror on each edge. Whilst the details are discussed later in my thesis, and elsewhere [30], the PCSEL and REPCSEL provide a unique opportunity to validate the PMC model as we have thorough device results for the situation where we have, and do not have a mirror surrounding a PCSEL. This contrasts other more complicated experimental results, discussed in the next chapter. In that case, a pumped PC region is surrounded by an unpumped PC region in the PCSEL. Here, the boundary of a PCSEL can be considered to have either a finite, or zero reflectance.

Figure 3.8 (a) shows the power-current (L-I) curve of a InP based PCSEL (black line with dots). The PCSEL has 0.4 um period with 400 um = 1000 #PC, 1295nm, as detailed in literature [29]. The L-I data for a REPCSEL is also shown that is identical to the PCSEL, but also has 100 periods of DBR surrounding the PCSEL. This is expected to act as a 0.86 reflectivity mirror.

The L-I is measured under continuous wave (CW) conditions supplied by Thorlabs 4001 at 15 °C. It can be seen from figure 3.8 (a) that the threshold current of REPCSEL is 0.673±0.001 A, of PCSEL is 0.91±0.001 A. The slope efficiency, η_{SE}, is also extracted, where REPCSEL has η_{SE} = 14±0.1 mWA^{-1}, PCSEL with η_{SE} = 3.4±0.1 mWA^{-1}. The calculated threshold current density of REPCSEL and PCSEL is 421 Acm^{-2} and 569 Acm^{-2}.

As reported previously [29] the coupling coefficients of the PCSEL AND REPCSEL are κ_{1D} = 113.2 cm^{-1}, κ_{2D} = 2.4 cm^{-1}, $\kappa_{\perp}$ = 1 cm^{-1}, κ_i = 5 cm^{-1} which can be directly used as the input parameters of the PMC model. The period of the PC is 400 nm, which give 1000 #PC. Using the PMC model, the in-plane loss of REPCSEL and PCSEL are predicted to be 5.54 cm^{-1} and 39.65 cm^{-1}.

Using the previously discussed equation (2.19). Where λ is the lasing wavelength, in this case, 1.295 um. A is an absorption constant, defining the ratio of the power absorbed in the substrate to the total output power, which is assumed to be 0.1. η_i is the internal quantum efficiency of the quantum well, which fitted to be 0.715. (An example of fitting has been shown in chapter 6) R is the reflectivity of the vertical mirror, which in this case R represents the reflectivity of

the p-contact and is estimated to be 0.2 [18]. With the parameters above, simulated values for $\alpha_{//}$ and a fit parameter of the radiative rate (1 cm^{-1}), the calculated slope efficiency of REPCSEL and PCSEL are 12.5 mWA^{-1} and 3.6 mWA^{-1}, which there is in excellent agreement with experimental results.

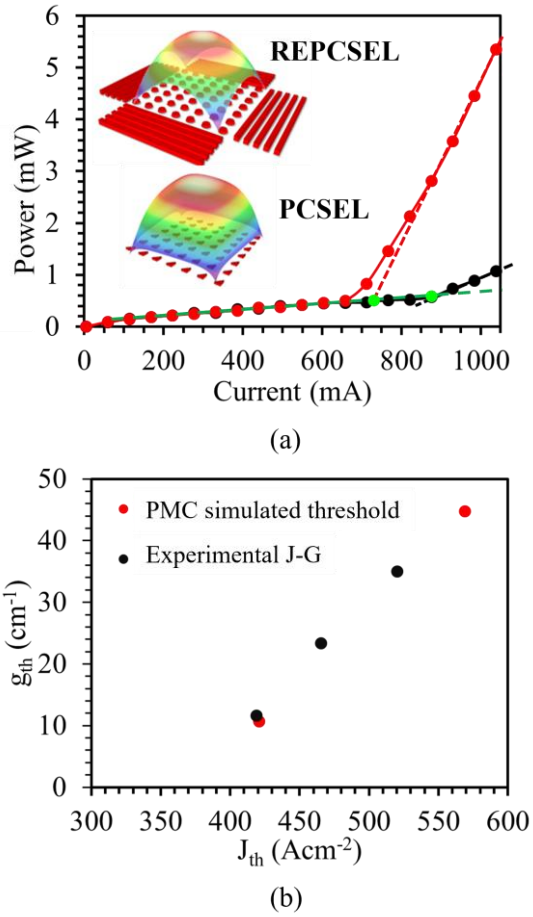

Figure 3.8 (a) The design of PC region and measured L-I curve of PCSEL and REPCSEL. (b) PMC simulated gain threshold of devices in (a) and experimental J-G of InP material.

Figure 3.8 (b) plots the current-density - gain (J-G) characteristics of the active material used in this PCSEL/REPCSEL. This was obtained by length dependent characterisation of broad area lasers. The threshold gain obtained by including the PMC simulated value of $\alpha_{//}$, and fit parameter of the radiative rate of 1 cm^{-1} is also plotted. Again, excellent agreement is obtained. The fact that both the slope efficiency and threshold gain can be fit is a strong case for the efficacy of the PMC model.

3.6 Summary

This chapter has introduced a new simulation method, the probabilistic Markov chain model. The purpose of building this model is to explore a method that links microscopic PC atom level

input parameters and macroscopic device-level output in a fast and simple manner. The basic algorithm of the PMC model simulates optical power scattering behaviour among PC atoms with a Markov chain method. The Markov chain transmission form has been given and discussed with examples. Then, the convergence criteria to shorten program runtime and ensure the accuracy of PMC model has been defined and discussed. The runtime termination criteria were set to 0.1 cm^{-1} in this thesis, based upon experimental accuracies of ±0.5 cm^{-1}. Finally, the PMC model has been validated using PMC simulate of two PCSEL devices and comparison of the predicted threshold gain and slope efficiencies. These devices are an InP-based PCSEL REPCSEL, differing only in the presence/absence of in-plane boundary mirrors. Using the radiative rate as a fit parameter, good agreement is obtained.

3.7 Future Work

As compared with other existing simulation methods, controlling microscopic input parameters (e.g. coupling coefficients) is not limited by physical factors (e.g. semiconductor material, refractive index, shape of PC) [9-12]. The input parameters can be defined by such simulation or experiment, and critically the effect of these parameters can be explored arbitrarily. This can be advantageous in studying the behaviour of optical power transfer among PC atoms and how this affects the device level losses. A key advantage of the PMC model is the low requirements of computing power and model reconfiguration time, making it a flexible design tool such as in applying boundary mirrors, absorbing regions, etc.

In the next chapter, the effect of different aspect ratios of a rectangular PCSEL are explored. Subsequently, several designs of PCSEL are simulated using the PMC model to explore the possibility of reducing in-plane loss. The use of in-plane boundary mirrors in a PCSEL is explored using a range of different coupling coefficients. I also explore the effect of spatially varying the presence of boundary mirrors. The effect of spatially varying the presence of boundary mirrors is also explored.

In Chapter 5 PCSELs with unpumped boundary PC regions are simulated as this is a common technique employed to reduce in-plane power loss, but limited simulations of the effect of self-absorption in the un-pumped region have been made. Further validation of the PMC model is also discussed.

In Chapter 6 it is shown how the PMC model can be used when making a new PCSEL device to decide on the required contact and PC sizes.

As shown in this chapter, the PMC model may be a useful tool in studying PCSEL mechanisms

and a useful guide in PCSEL design. However, the model has not been used and validated in triangular lattice PCSELs [9,11,31-33]. This essentially just requires recoding and the replacement of the cardinal directions for each PC atom (north, south, east, west) with a 6-fold set of directions, e.g., 0°, 60°, 120°, 180°, 240°, 300°.

There is no gain/loss calculator built into the program, so in this thesis, such simulation has all been done in commercial software or own programmed codes, which is outside of the PMC model, including such functionality could make the program more convenient. But again, this is essentially a coding exercise, incorporating modules from elsewhere, and could be considered when improving the "GUI", front end for users.

It is also possible in future to integrate a device simulator (FDTD, PWE, etc) to determine input scattering parameters of PMC algorithms. However, at this stage of development it is better to carefully review the outputs of these simulators before their use.

Of significant future use may be the change from this static model to a dynamic model. In a future dynamic model, power generation at a given PC atom could be replaced by variables for gain and lasing photon generation. These could be wavelength dependent and be varied at each time step (~10^{-13} s). In this case a range of dynamic effects may be explored, and the speed of the PMC model may become very powerful.

References

[1]. J. Liu, Y. Gao, P. Ivanov, P. Harvey, and R. Hogg, "Probabilistic Markov chain modeling of photonic crystal surface emitting lasers," *Appl. Phys. Lett.*, vol. 123, no. 26, p. 261107, Dec. 2023.

[2]. J. Liu et al., "Convergence criteria for probabilistic Markov chains modelling of photonic crystal surface emitting lasers," *Proc. SPIE*, vol. 12440, p. 124400D, Mar. 2023.

[3]. J. A. Pople, "Ab initio molecular orbital theory," in *Advances in Chemical Physics*, vol. 8, pp. 239-286, 1965.

[4]. T. Inoue et al., "General recipe to design photonic crystal cavities for high-power lasers," *Opt. Express*, vol. 23, no. 11, pp. 15565-15574, 2015.

[5]. T. Inoue et al., "Three-dimensional coupled-wave theory for scalable photonic-crystal lasers," *Phys. Rev. Appl.*, vol. 16, no. 3, p. 034038, 2021.

[6]. T. Inoue et al., "Beam-steering PCSELs via phase-modulated 3D coupled-wave theory," *IEEE J. Sel. Topics Quantum Electron.*, vol. 28, no. 3, p. 8200108, 2022.

[7]. T. Sakai and S. Noda, "Coupled-wave theory for photonic crystal waveguides," *Opt. Express*, vol. 14, no. 20, pp. 9460-9466, 2006.

[8]. T. Sakai, E. Miyai, and S. Noda, "Coupled-wave model for square-lattice photonic crystal lasers

with transverse-electric polarization," *IEEE J. Quantum Electron.*, vol. 43, no. 11, pp. 1179-1186, 2007.

[9]. S. Noda, M. Yokoyama, M. Imada, A. Chutinan, and M. Mochizuki, "Polarization mode control of two-dimensional photonic crystal laser by unit cell structure design," *Science*, vol. 293, no. 5532, pp. 1123-1125, 2001.

[10]. K. Hirose et al., "Watt-class high-power, high-beam-quality photonic-crystal lasers," *Nature Photon.*, vol. 8, pp. 406-411, 2014.

[11]. H. Matsubara et al., "GaN photonic-crystal surface-emitting laser at blue-violet wavelengths," *Science*, vol. 319, no. 5862, pp. 445-447, 2008.

[12]. T. Inoue et al., "Topological photonic crystal lasers with FDTD-optimized mode confinement," *Nature Commun.*, vol. 11, no. 1, p. 2758, 2020.

[13]. A. A. Markov, "Rasprostranenie zakona bol'shih chisel na velichiny, zavisyaschie drug ot druga," *Izv. Fiz.-Mat. Obsch. Kazan Univ.*, vol. 15, pp. 135-156, 1906 (in Russian).

[14]. A. N. Kolmogorov, "Über die analytischen Methoden in der Wahrscheinlichkeitsrechnung," *Math. Ann.*, vol. 104, pp. 415-458, 1931 (in German).

[15]. J. R. Norris, *Markov Chains*. Cambridge, U.K.: Cambridge Univ. Press, 1997.

[16]. M. Yoshida, M. De Zoysa, K. Ishizaki et al., "Double-lattice photonic-crystal resonators enabling high-brightness semiconductor lasers with symmetric narrow-divergence beams," *Nature Mater.*, vol. 18, pp. 121-128, 2019.

[17]. M. Yoshida et al., "Recent advances in photonic-crystal surface-emitting lasers," *J. Phys. Photon.*, vol. 3, no. 2, p. 022006, 2021.

[18]. K. Emoto et al., "Wide-bandgap GaN-based watt-class photonic-crystal lasers," *Commun. Mater.*, vol. 3, no. 1, p. 72, 2022.

[19]. M. Yoshida et al., "High-brightness scalable continuous-wave single-mode photonic-crystal laser," *Nature*, vol. 618, pp. 727-732, 2023.

[20]. B. W. Hakki and T. L. Paoli, "Gain spectra in GaAs double-heterostructure injection lasers," *J. Appl. Phys.*, vol. 46, no. 3, pp. 1299-1306, 1975.

[21]. B. W. Hakki and T. L. Paoli, "CW degradation at 300 K of GaAs double-heterostructure junction lasers," *J. Appl. Phys.*, vol. 44, no. 9, pp. 4113-4119, 1973.

[22]. P. Blood, G. M. Lewis, and P. M. Smowton, "Progress in GaAs-based quantum-dot lasers," *IEEE J. Sel. Topics Quantum Electron.*, vol. 9, no. 5, pp. 1275-1282, 2003.

[23]. Y. C. Xin et al., "High-performance InAs quantum dot lasers on GaAs substrates," *Proc. SPIE*, vol. 5722, pp. 49-58, 2005.

[24]. D. T. Cassidy, "Laser diode output power measurement errors caused by temperature and drive current dependence of the emission profile," *J. Appl. Phys.*, vol. 56, no. 11, pp. 3096-3099, 1984.

[25]. V. Jordan, "Semiconductor laser linewidth: Theory and experiment," *Proc. Inst. Elect. Eng.*, vol. 141, no. 1, pp. 13-20, 1994.

[26]. K. L. Shaklee and R. F. Leheny, "Direct determination of optical gain in semiconductor crystals," *Appl. Phys. Lett.*, vol. 18, no. 11, pp. 475-477, 1971.

[27]. A. Oster, G. Erbert, and H. Wenzel, "Measurement of the internal quantum efficiency of laser diodes," *Electron. Lett.*, vol. 33, no. 10, pp. 864-865, 1997.

[28]. Y. C. Xin et al., "1.3-μm InAs quantum-dot lasers fabricated on GaAs substrates using InAlAs strain-reducing layers," *IEEE J. Quantum Electron.*, vol. 42, no. 12, pp. 1259-1266, 2006.

[29]. Z. Bian et al., "Resonator embedded photonic crystal surface emitting lasers," *npj Nanophoton.*, vol. 1, no. 1, p. 13, 2024.

[30]. Z. Bian, "InP-based photonic crystal surface emitting lasers," Ph.D. dissertation, James Watt School of Eng., Univ. Glasgow, Glasgow, U.K., 2023.

[31]. T. Inoue et al., "Topological photonic crystal lasers with FDTD-optimized mode confinement," *Nature Commun.*, vol. 11, no. 1, p. 2758, 2020.

[32]. S.-H. Kim et al., "Design of triangular-lattice photonic crystal surface-emitting lasers for low-threshold operation," *Opt. Express*, vol. 18, no. 23, pp. 23894-23905, 2010.

[33]. K. Emoto et al., "Ultra-low divergence triangular-lattice PCSELs for LiDAR," *IEEE Photon. J.*, vol. 14, no. 4, p. 8200508, 2022.

Chapter 4: Simulation of PCSEL Devices Using PMC Modelling – In-Plane Mirrors

4.1 Introduction

Unlike previous generations of semiconductors, F-P lasers, DFB lasers or VCSELs, the emission direction of PCSEL is perpendicular to the plane of the resonance cavity (2D PC) which brings about a new equation to describe the gain and loss. (equation 2.18) It is standard in the engineering of conventional laser diode classes to minimise the parasitic losses, and "right-size" the total loss to obtain high slope efficiency (η_{SE}) and low threshold (I_{th} or J_{th}) to maximise power conversion efficiency (PCE).

In the PCSEL, there is an additional loss term, $\alpha_{//,}$ that describes the in-plane loss of power as it exits the PC array, which is one component of the parasitic loss of the PCSEL. It has been discussed in previous chapters (figure 3.5) that increasing the size of the PC array decreases the in-plane loss, $\alpha_{//}$. This parameter is also very difficult to extract experimentally, [1] making its evaluation through other means, such as the PMC model, very important.

The outline of the PMC modelling technique, and its validation were discussed in the previous chapter (chapter 2). The PMC model is not limited by a particular input PC shape, rather the scattering parameters at each PC atom. It is also possible to introduce mirrors arbitrarily. Rather than being used to validate experimental results, e.g. where experimentally obtained structural information provides simulated band-structure and device parameters [2], the PMC model can be used to explore the limits of PCSEL design arbitrarily. This is achieved through the choice of scattering strengths and PC boundary conditions such as no mirror, and mirrors of arbitrary reflectivity that may be varied spatially.

In this chapter, using high coupling coefficient inputs [2] as a starting point the effect of the strength of coupling coefficients on in-plane loss is explored. The effect of perimeter mirrors on in-plane loss is then discussed in terms of uniform mirrors with arbitrary reflectivity. The effect of spatially varying perimeter mirrors on in-plane loss and near-field pattern is then explored [3]. Low coupling coefficient devices and the requirements for a resonator effect to be observed are also considered. These design requirements supported work in realising Resonator Embedded PCSELs (REPCSELs). The work goes on to use experimental results and simulations of the expected wavelength dependent reflectivity to predict the different in-plane losses that different modes experience [3]. Finally, the PMC model is used to predict the gain

threshold of devices fit a J-G curve along with experimental data, the excellent agreement provides validation of the PMC model.

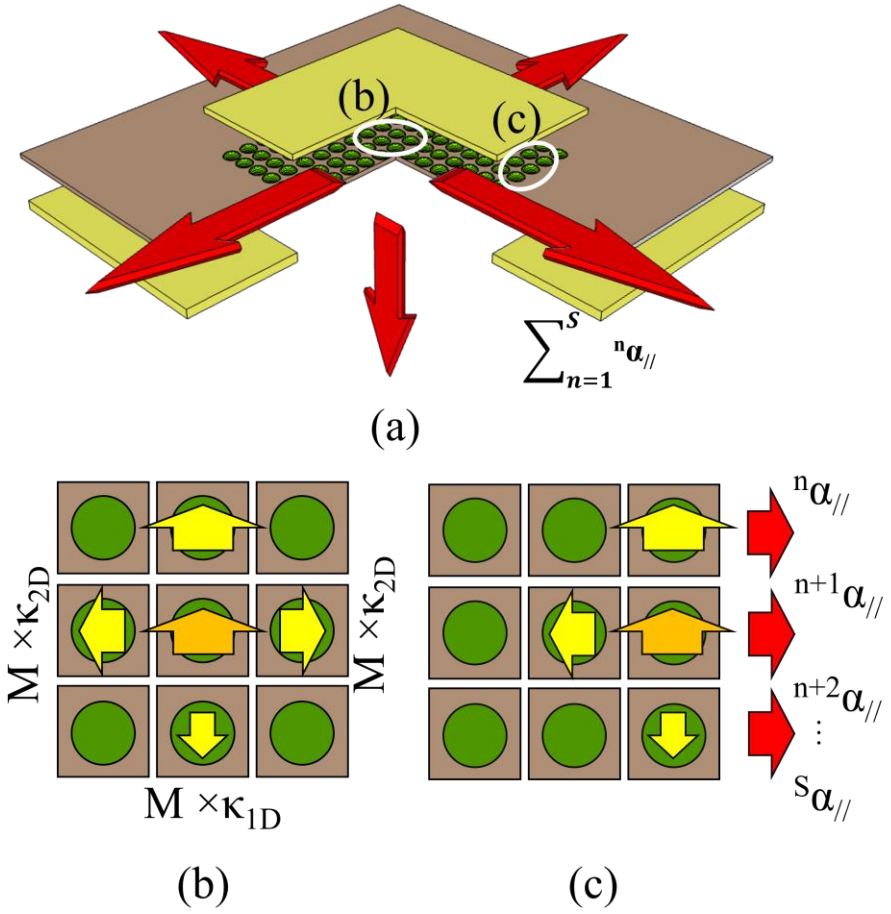

Table 4.1: (a) Schematic of PCSEL device. (b) An example of applying M on in-plane coupling coefficients. (c) An example of calculating in-plane loss.

4.2 Effect of Coupling Coefficients on PCSEL In-Plane Loss $\alpha_{//}$

It has been demonstrated in previous studies that the coupling coefficients describes the coupling strength of mutual coupling strength among the four fundamental Block waves. κ_{1D} and κ_{2D} are used to represent waves transferring to different directions coupling with each other. [4-9] In the PMC model, these coupling coefficients relate to scattering coefficients, the probability of optical power scattered to different directions when interacting with PC atoms. Due to which, the value of these input parameters would significantly change the loss condition. So, it would be helpful to know their effects on reducing in-plane loss. It is seen that in the literature, the value of these coupling coefficients is different due to different materials and the design of the PC, [2, 10-13] but there is no research studying how these coefficients affect the device performance. Based on the commissioning parameters mentioned previously (chapter

3.3), reasonable multiples (M = 0.5,1,2 and 3) are applied directly to the values of in-plane coupling coefficients (κ_{1D} and κ_{2D}) to explore the effect on device level losses. Figure 4.1 (a) shows a schematic of the PCSEL device. In this chapter, the size of the PCSEL (described in number of PC atoms #PC) is the size of electrode, (b) shows an example of nine neighbouring PC atoms in the middle of PC region and how multiple, M applies to κ_{1D} and κ_{2D}; (c) shows the PC atoms on edge of PC region and an example of how the in-plane power loss is collected in the PMC model.

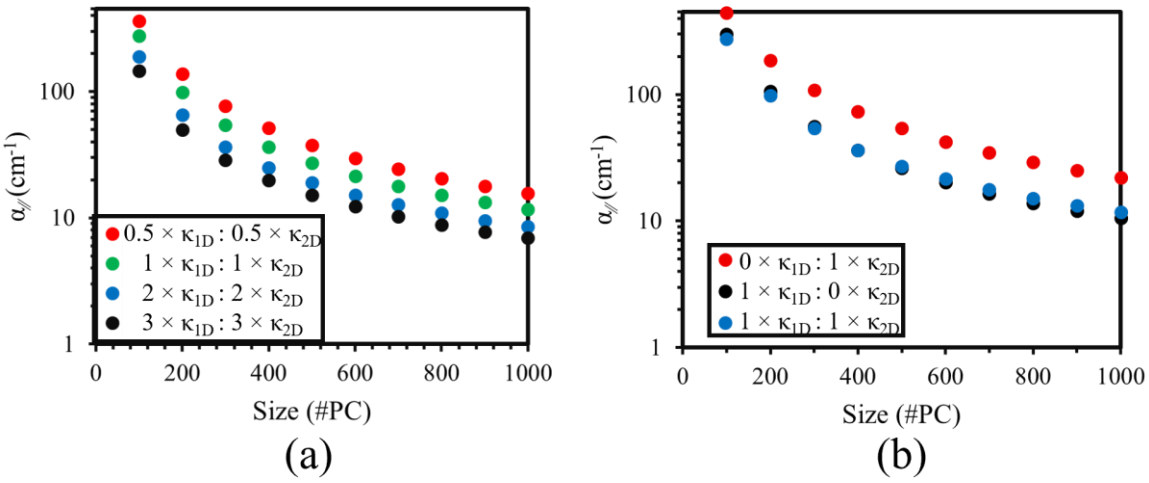

Figure 4.2: (a) Simulated in-plane loss as a function of size of PCSEL applying M = 0.5, 1, 2 and 3 to both in-plane coupling coefficients. (b) Simulated in-plane loss as a function of size of PCSEL applying M = 0 to one of the in-plane coupling coefficients.

Figure 4.2 plots the in-plane loss simulated by the PMC model as a function of size of PCSEL for various PC scattering coefficients. The multiplication factor M is applied to κ_{1D} and κ_{2D} simultaneously in figure 4.2 (a), and separately in figure (b). Figure 4.2 (a) shows that the value of coupling coefficients significantly affects the in-plane loss. Increasing the value reduces the in-plane loss. However, it should be noted that the minimum in-plane loss is ~ 7 cm^{-1} even with very large coupling coefficients (e.g. when M = 3, κ_{1D} ~ 4000 cm^{-1}, κ_{2D} ~ 1160 cm^{-1}). Figure 4.2 (b) shows the case when M = 0 applies to one of the in-plane coupling coefficients, and to both for comparison. It can be noticed that comparing with red dots (κ_{1D} =0), black dots (κ_{2D}=0) is much closer to blue dots (κ_{1D}, κ_{2D}≠0), which means in this case, κ_{1D} is more effectively in reducing in-plane loss.

However, the conclusion made above may be due to the original choice of κ_{1D}, which is approximately 3.5 times of the κ_{2D} value. So, in figure 4.3, the original κ_{1D} and κ_{2D} are both set to 500 cm^{-1}. 0, 1, 2 and 3 are used as multiple. Figure 4.3 (a), (b) and (c) shows the cases when

M=0 and 1 applies separately to κ_{1D} and κ_{2D} and to both. It can be seen that, when κ_{1D} and κ_{2D} have the same value, the difference in figure 4.2 (b) becomes smaller, but still appears. So, the previous assertion about the dominant scattering to reduce in-plane loss was correct. To analyse this difference, a $\Delta\alpha_{//}$ is defined. $\Delta\alpha_{//}$ describes the difference between cases of both in-plane coupling coefficients having a particular value and the case when one of them is 0, e.g. in figure 4.3 (b), the red dots represent the difference of in-plane loss between case, κ_{1D} = 500 cm^{-1} and κ_{2D} = 500 cm^{-1}, and the case, κ_{1D} = 500 cm^{-1} and κ_{2D} = 0 cm^{-1}. It can be seen from the figure that $\Delta\alpha_{//}$ decreases when size becomes larger, larger coupling coefficients lead to smaller $\Delta\alpha_{//}$. Triangular dots always have lower values than circular dots, which again means κ_{1D} has a greater influence in reducing in-plane loss.

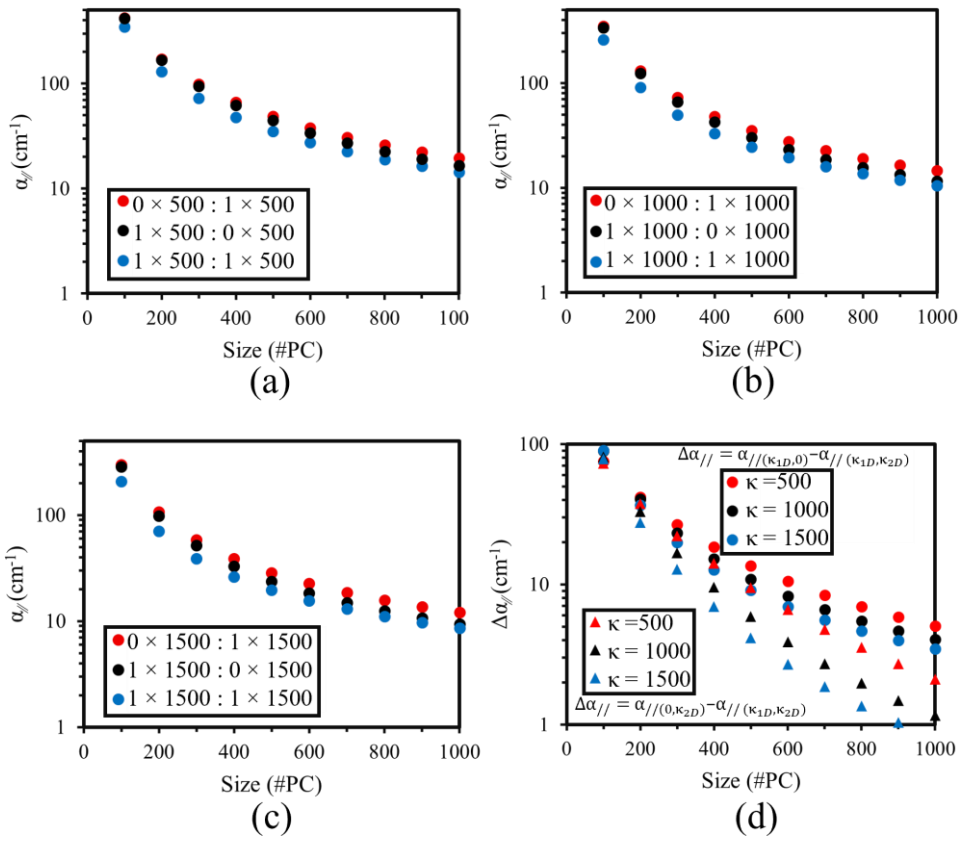

Table 4.3: κ = (a) 500 cm^{-1}, (b) 1000 cm^{-1}, (c) 1500 cm^{-1}. (d) differential in-plane loss with κ = 500 cm^{-1}, 1000 cm^{-1} and 1500 cm^{-1}.

From figure 4.2 and 4.3, it can be concluded that, it is possible to realize very low in-plane loss (<1 cm^{-1}) if the multiple, M is large enough. However, this case is only possible when the values of κ_{1D} and κ_{2D} are very large, which is limited by the pattern and background material of the PC. Engineering κ_{1D} is relatively more effective in reducing in-plane loss than κ_{2D}. It

should also be noted that, the value of κ_{1D} enhances 1D coupling while κ_{2D} enhances 2D coupling, although κ_{1D} or κ_{2D} may have close effect on in-plane loss, the effect on other PCSEL performance factors cannot be ignored, e.g. on far-field profile. In summary of this section, according to results from the PMC model, reducing in-plane loss by increasing value of in-plane coefficients alone may not be a suitable route to reduce in-plane loss, in the quest to make higher efficiency PCSEL devices.

4.3 Effect of In-plane Reflection on PCSEL In-Plane Loss $\alpha_{//}$

The realization of good quality surface emission from PCSELs is reached by utilizing 1st and 2nd order Bragg diffraction. It has been shown above that adjusting the values of coupling coefficients to reduce in-plane loss may not be a simple solution to reducing in-plane loss. According to previously mentioned equation, (eq. 2.18) the in-plane loss can be reduced by limiting the exiting power from PC region, which can be a macroscopic method to reach this goal.

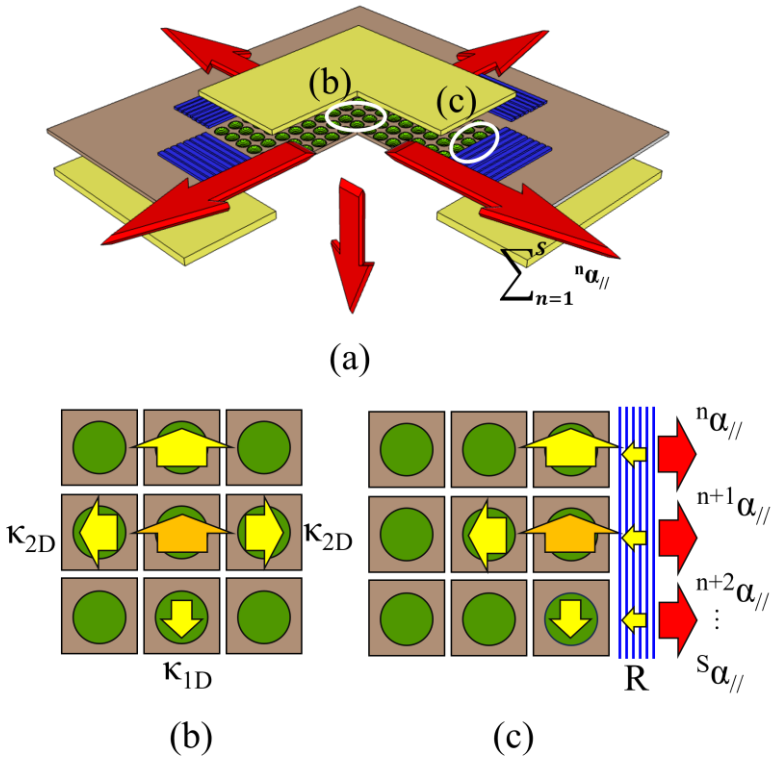

Table 4.4: (a) Schematic of PCSEL device with in-plane mirrors. (b) An example of in-plane coupling coefficients. (c)An example of calculating in-plane loss.

Distributed Bragg reflectors (DBRs) utilize a highly reflective 1D periodic structure that satisfies the Bragg condition. [14-15] The multiple layer DBR is used commonly in several

previous generations of semiconductor devices such as DBR lasers, distributed feedback (DFB) lasers and vertical cavity surface emitting lasers (VCSELs).

As mentioned in previous chapter (chapter 2.4), beam quality can be significantly improved by adding a DBR to an FP laser, to one end of a ridge (DBR laser) or both sides of the ridge (DFB laser). VCSELs, unlike the in-plane light coupling lasers, sandwiches two DBR mirrors outside of the active region in a vertical direction (epitaxial direction) to get optical feedback, gain and emission in this direction, enabling surface emission. The DBR has been shown to provide wavelength selectivity and enhance the beam quality, which makes it a good candidate to be included in PCSEL devices. As the required characteristic from DBR in this chapter is just limiting the light that exists the PC in the in-plane direction, it is also termed an "in-plane mirror".

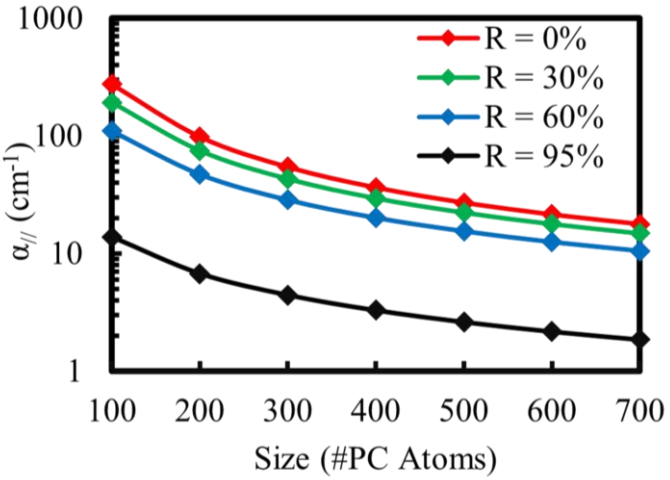

Figure 4.5: In-plane loss as a function of size with different in-plane

Figure 4.4 (a) shows a schematic of a PCSEL with in-plane mirrors on edges (blue bars, not in scale). It is assumed to have 0◦ phase shift between PC and in-plane mirror. [13] Figure 4.4 (b) shows the definition of κ_{1D} and κ_{2D}, it is assumed not to be affected by the introduction of those mirrors. Figure 4.4 (c) shows how a mirror is applied to edge PC atoms and how the PMC model calculates in-plane loss with reflectivity. In the PMC model, the phase of light is not considered, so the reflectivity, R in this thesis is power reflectivity. The values of reflectivity (R = 30%, 60% and 95%) used are based on typical values from the literature. [13]. It should be noted that the total size of the device may be increased due to the length of the DBR gratings, but in this thesis, size only refers to the PC atom number. Figure 4.5 shows the simulated in-plane loss as a function of the size of PCSEL with selected reflectivity. It can be seen from figure that increasing R can significantly reduce the in-plane loss, and make it possible to zero

it when the PCSEL is sufficiently large. 4.4 Structured Reflection Effects for PCSEL In-plane Loss and Near-Field Profile

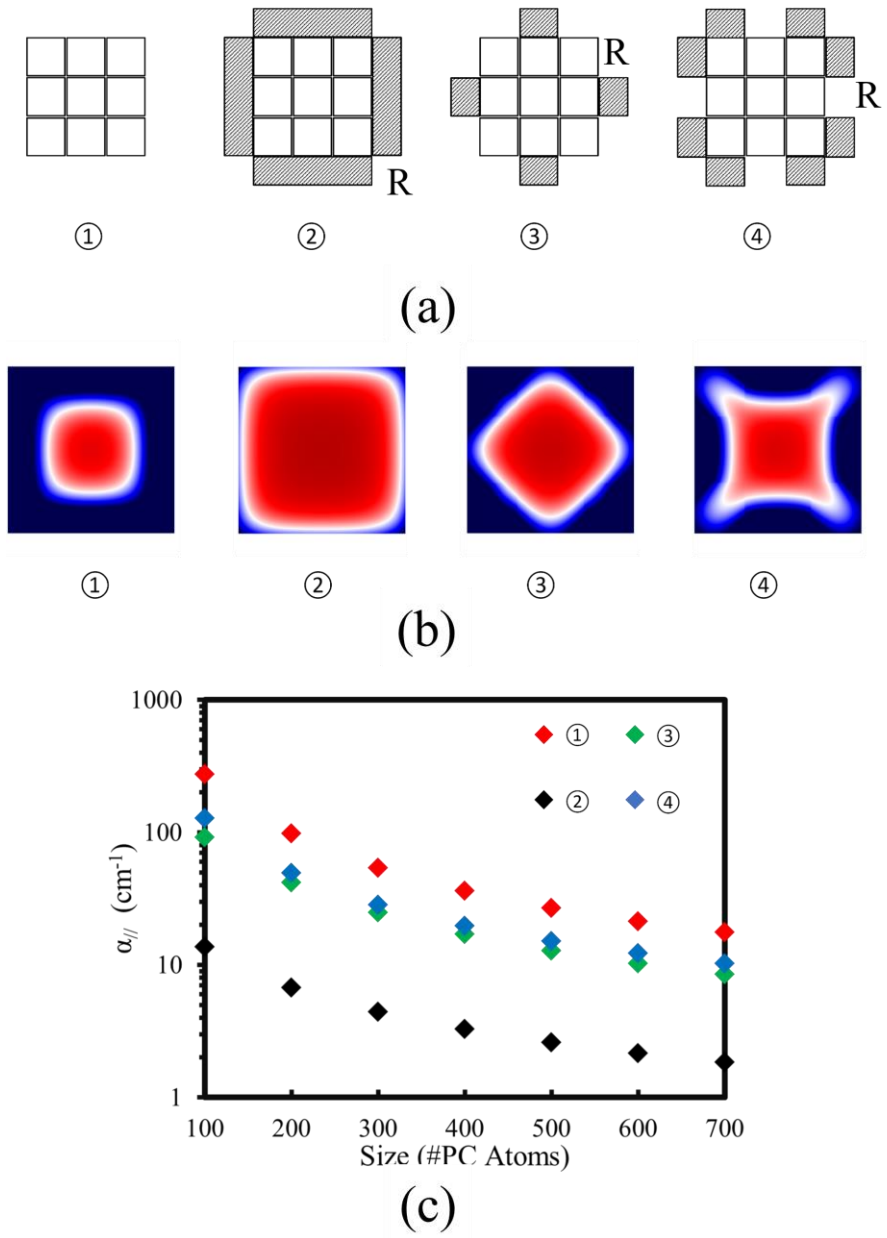

Figure 4.6: (a) in-plane loss of devices with different types of structured reflector varies with size. (b) schematics of four different types of structured reflector (shadowed area) (c) Nearfield mode of device with structured reflector.

It has been shown above that integrating an in-plane mirror around the PCSEL boundary significantly reduces the in-plane loss. Considering the possible simplicity of manufacturing the DBR structures, it would be interesting to further explore the spatial variation of these mirrors. Figure 4.6 (a) shows the schematic of different types of structured DBR on the PC array, which is represented by white squares (not to scale). The shadowed parts are in-plane

mirrors with reflectivity R, which is also not to scale. ① is a normal PC array (without any mirror) as the control sample; ② is the above mentioned PCSEL with perimeter mirror; ③ is with central area covered DBR and ④ is corner area covered DBR. In this simulation, the design of ③ and ④ are complementary with 1/3 length of PC array edge of each DBR width. To make the results easier to analysis, R = 95%, is used in this simulation. [13] The scale of simulated near-field pattern, shown in figure 4.4 (b) is the same. It can be noticed that when applying in-plane mirrors, the vertical emission does increase, and the shape of the near-field pattern can be controlled by engineering the structure of the DBR. Figure 4.6 (c) shows the simulated in-plane loss as a function of the size of the PCSEL with corresponding designs. It can be noticed that the effect of reducing in-plane loss will be significantly reduced when in-plane mirror coverage is reduced.

4.5 Resonator Effect in REPCSELs

The effect of in-plane mirrors on the in-plane loss of PCSELs has been discussed above, comparing with other above discussed design, applying in-plane mirrors may reduce the in-plane loss to an almost negligible value (~1 cm^{-1}) with proper size of device and in-plane reflectivity R. Although some disadvantages have been pointed out, it is still worth further exploration of the possibility of zeroing in-plane loss and other effects of in-plane mirror. In this section an InP-based resonator embedded PCSEL (REPCSEL) has been designed, developed and simulated by the PMC model.

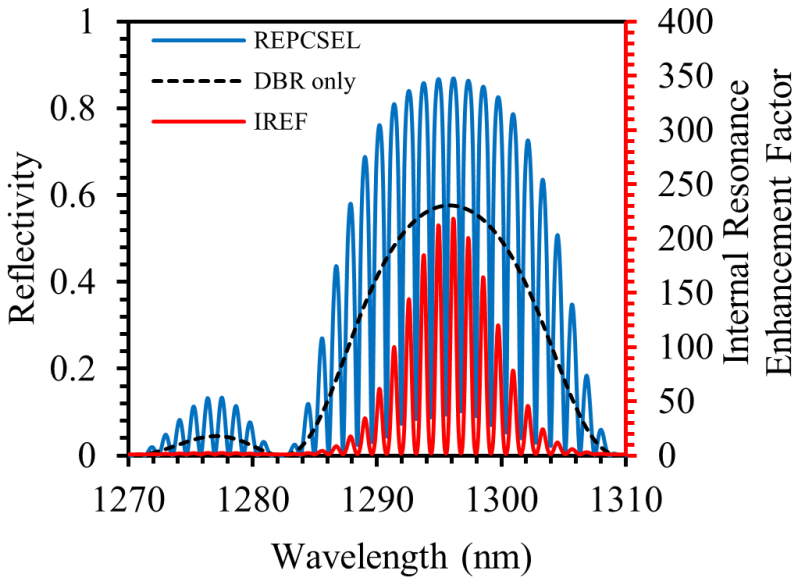

Figure 4.7: Reflectance simulation of a single DBR structure (black dotted line); REPCSEL (blue line) and associated with internal resonance enhance factor (red line).

As the phase shifting and reflectivity significantly affects the effect of in-plane mirrors, the structure of the mirror needs to be designed carefully. In all calculations, only reflected light in-phase with the PC is considered. Figure 4.7 shows the calculated reflectance of a DBR mirror (black dotted line) and a well-defined 200 um cavity length for Fabry-Pérot resonator effect (blue line). The red line is the calculated internal resonance enhancement factor (IREF) [16] which describes the amplified ratio between the enhanced light due to the REPCSEL structure and the transmitted light from PC region. This simulation is carried out using a transmission matrix approach via the cavity modelling framework (CAMFR) software [13], which is a fully vectorial Maxwell solver to calculate the reflectivity of the multi-layer stack. In this case, the mark/space ratio (MSR) is defined as 50%. Zero phase shift phase is achieved by engineering the gap between PC and mirrors. The IREF can be estimated as:

$$IREF = \frac{1}{\left(1 - \sqrt{R}^2\right)} \qquad equation 4.1$$

It can be seen from the result that the maximum reflectivity is ~86%, which is used in the following simulation. [13]

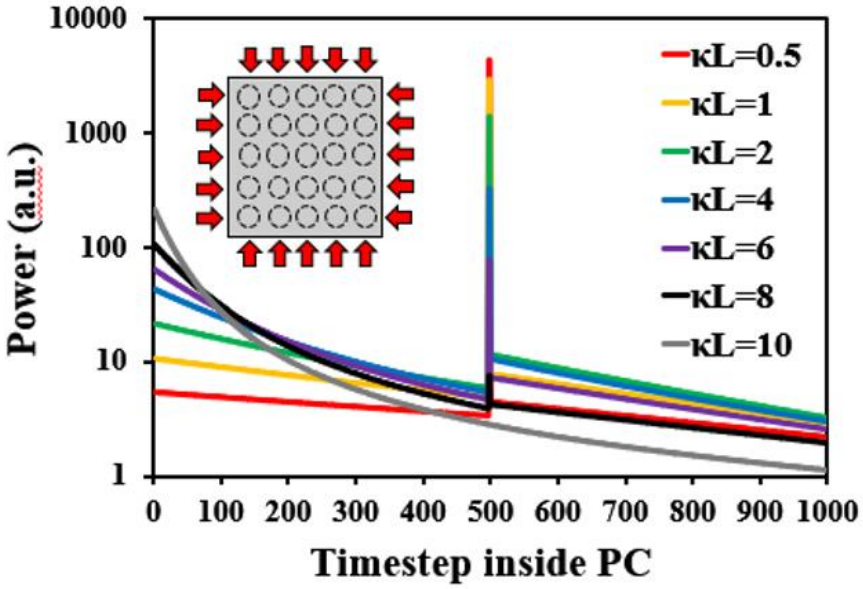

Figure 4.8: Simulated in-plane power loss as a function of time for different values of κL according to the PMC model. Inset is a schematic of PMC model at time-step = 0. The size of REPCSEL is 500 #PC, red arrows represent the incident light at the boundary.

To explore the effect of in-plane coupling on the resonator, a new application has been added to PMC model. Unlike previous mentioned simulations, the light is not continuous injected to all PCs, but only injected once at timestep = 0 from the edge PCs towards inside of PC region. The light leaving the PCSEL is plotted as a function of time-step for a range of coupling

coefficients. Figure 4.8 plots this edge emitted power as a function of timestep for different κL. Input parameters are from literature, period, a = 400 nm; κ_{1D} = 113.2 cm^{-1}; κ_{2D} = 2.4 cm^{-1}. In this case, the size of REPCSEL is set as constant 500 #PC, the coupling coefficients are same scaled, e.g. κL = 10 corresponds to κ_{1D} = 113.2×2 cm^{-1}; κ_{2D} = 2.4×2 cm^{-1}. An obvious peak occurs at timestep = 500 which represents unscattered light arriving at the opposite edge of the REPCSEL. It can be seen that, with increasing κL, the peak decreases and disappears at κL <~ 10, which indicates that when in-plane mirror has reflectivity, R = 86%, κL =~ 10 is needed to avoid the in-plane resonance effect for a REPCSEL.

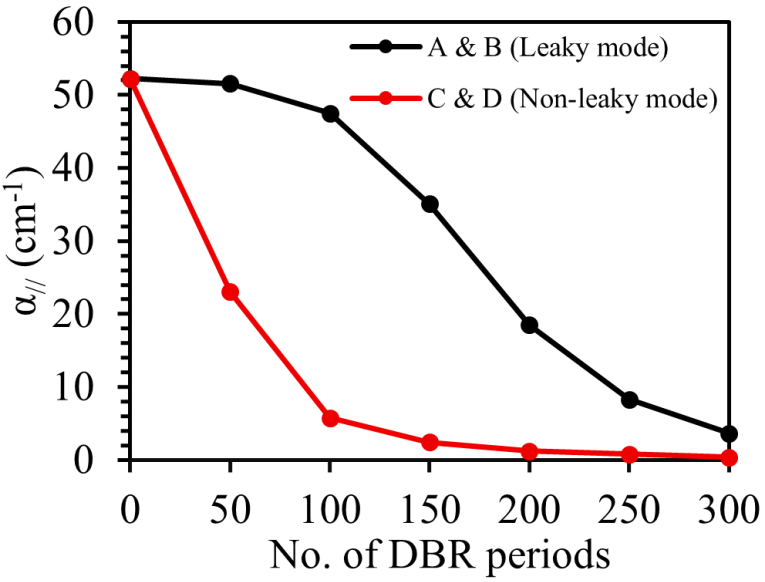

Figure 4.9: The simulated in-plane loss of a 1.3 um REPCSEL for the two band-edges as a function of number of perimeter DBR pairs.

To analyse the effect of in-plane mirrors on this emission enhancement at threshold, the in-plane loss of leaky mode and non-leaky modes at gamma point is calculated. Figure 4.9 shows the simulated in-plane loss as a function of number of DBR repeats. The black line with dots is for the leaky modes (A and B), red line with dots is non-leaky modes (C and D). From the plot it can be known that without a mirror the two band edges have the same in-plane loss, and this value is comparatively high (up to 52 cm^{-1}). With the increase of number of DBR mirror repeats, the in-plane loss for both band edges decreases, and may eventually be zeroed for >300 repeats. For intermediate DBR number, there is a difference in the in-plane loss for the two sets of modes. It should be noted that this difference between leaky mode and non-leaky modes reaches a maximum at 100 repeats of in-plane mirror (difference in loss ~45 cm^{-1}). This difference in-plane loss (or threshold gain) is discussed below.

In summary, for REPCSEL devices with small value coupling coefficient, a large size is needed

to avoid too strong in-plane resonance effect, on the other hand, κL is the key factor to consider when designing REPCSEL. It has been proved that the in-plane mirror shows significant effect on reducing threshold, and it is possible to select the lasing mode by engineering the frequency of mirror.

4.6 PCSEL Realisation & Validation of Prediction

Using the design rules discussed above, a series of InP-based PCSEL and REPCSEL have been realized. The devices are from same wafer, have undergone identical fabrication process and are designed to have κL = ~2. The REPCSEL has in-plane mirror with reflectivity R = 0.86 so as to have the largest difference between in-plane loss $\alpha_{//}$ for the different modes. [13]

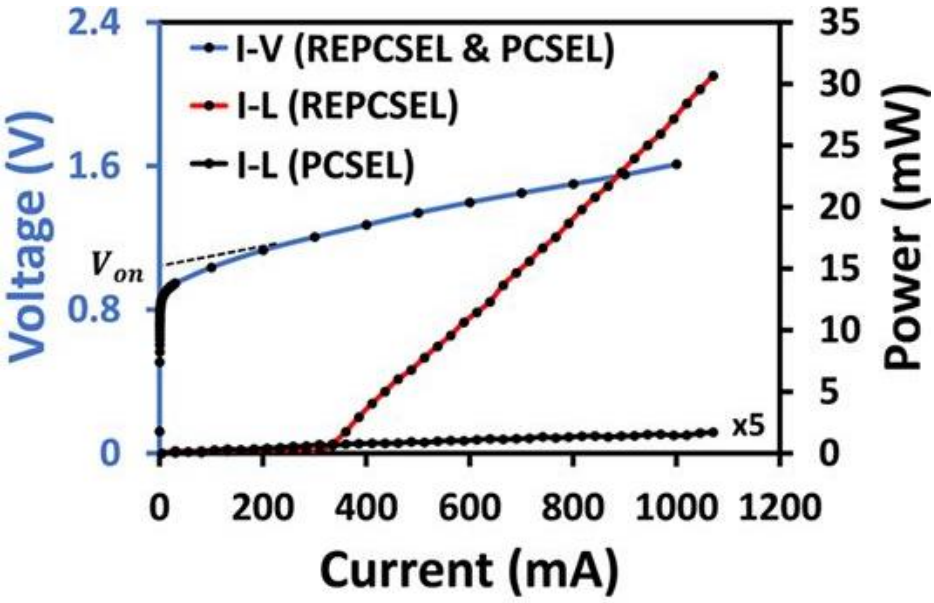

Figure 4.10: Measured LIV of a 200 × 200 um REPCSEL and PCSEL.

Figure 4.10 shows the measured LIV curves of a 200 × 200 um REPCSEL (red dots) and PCSEL device (black dots). the IV curves are measured under a 2-wire measurement system supplied by a Keithley 2401 continuous wave current source. While the LI curves are measured a pulsed condition with 2% duty cycle and 5 us pulse width supplied by a ILX Lightwave LDP-3840 pulsed current source. It can be observed that the threshold current of the REPCSEL is ~325 mA (860 Acm^{-2}) whilst the PCSEL does not lase up to 1050 mA (~3 $kAcm^{-2}$). The slope efficiency of the REPCSEL is measured to be ~0.04 WA^{-1}. It can be noted that the REPCSEL shows lower threshold current and higher efficiency. These advantageous performances are achieved not by the introduction of a vertical reflector [2] but through in-plane mirrors.

Figure 4.11 (a) and (b) plots the measured band structure of the REPCSEL device at 0.4 × I_{th}

and 1.2 × I_{th}. The band structure is measured from Γ point towards X and M directions with 10 steps of XX um. In figure 4.9 (a), two modes (leaky and non-leaky modes) are observed with similar intensity. The emission from the non-leaky modes is enhanced by positioning the modes at the peak of the IREF curves in figure 4.7. When lasing, in figure 4.11 (b) only the non-leaky mode is observed, which indicates that threshold gains are different despite radiative rates and internal losses being very similar. The comparison between the cases below and beyond threshold suggests that the in-plane loss is different for these modes.

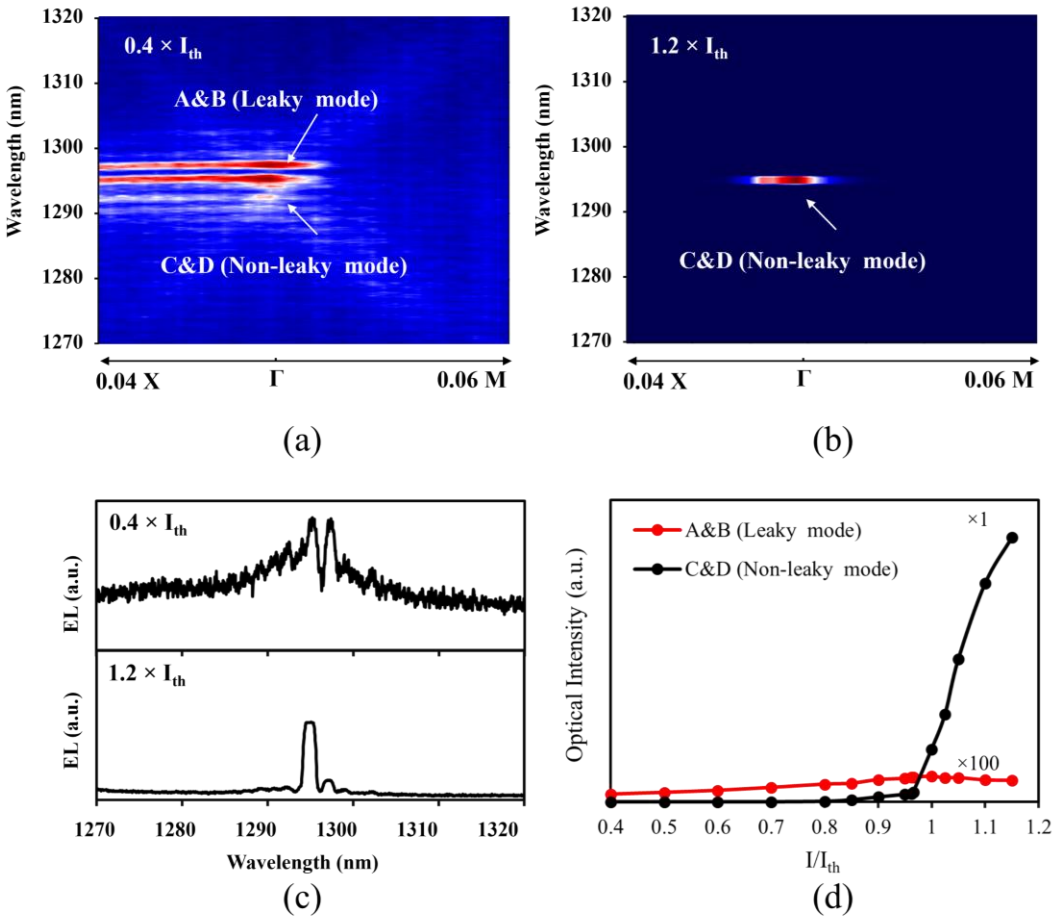

Figure 4.11: (a) The measured band structure of the REPCSEL at I = 0.4 × I_{th}. (b) The measured band structure of the REPCSEL at I = 1.2 × I_{th}. (c) The corresponding EL spectrum at Γ point with I = 0.4 × I_{th} and I = 1.2 × I_{th}. (d) The maximum optical intensity of the band edges as a function of I/I_{th}. The optical intensity of leaky modes (mode A and B) is plotted × 100 for ease of comparison.

Figure 4.11 (c) plots the spectrum of Γ point at corresponding driven current in figure 4.11 (a) and (b). For ease of comparison, the optical intensity of plots in figure 4.11 (c) are not in same scale, which leads to the different signal/noise.

Figure 4.11 (d) plots the intensity of the sub-threshold surface emission as a function of driven current for the two sets of modes. Super-luminescence occurs for only one set of modes at

approximately 0.75 × I_{th}, which indicates that the total optical loss for non-leaky mode is lower than that of the leaky mode. This agrees with the reduction of in-plane loss which resulted above. In summary, the simulation and experiment are in very good qualitative agreement.

4.7 Validation of Predicting Gain Threshold of PCSELs

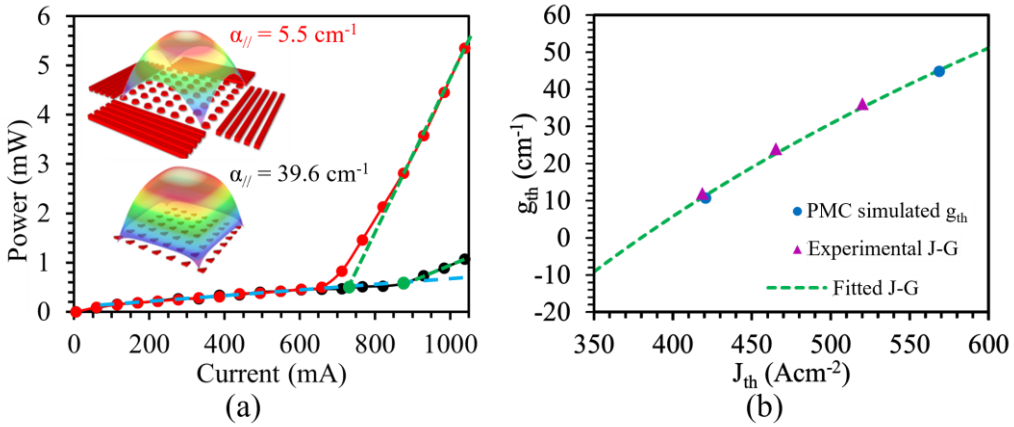

Figure 4.12: (a) Measured L-I of REPCSEL (red) and PCSEL (black), dotted lines are trend line of linear region. Schematic of REPCSEL and PCSEL are insets. (b) PMC simulated (blue dots), experimental (purple dots) and fitted (green dotted line) g_{th} as a function of J_{th}.

As described above, a validation of the PMC model was made by predicting the resonance effect of the in-plane mirror of REPCSEL. Here, another pair of REPCSEL and PCSEL are analyzed by the PMC model. Along with the experimental data, the PMC model predicts the threshold gain of both devices to fit the current density – threshold gain curve (J-G curve). With the correct fitting, the transparent current density J_0 and transparent gain g_0 are explored. Then other input parameters are extracted from a GaAs-based PCSEL device from literature. Finally, an output ratio is defined, which is treated as the jointly main output along with power conversion efficiency (PCE) discussed in this chapter.

Figure 4.12 (a) shows the power-current (L-I) curve of an InP-based PCSEL (black line with dots). The PCSEL has 0.4 um period with a side of 400 um (1000 #PC) operating at 1295 nm. The L-I of a REPCSEL, nominally identical to the PCSEL, but with 100 periods of DBR surrounding the PC is also plotted. There are some previously reported results from devices with a side of 200 um. [13]. It can be seen from figure 4.12 (a) that the threshold current (green dots) for REPCSEL is 730 mA of PCSEL is 880 mA. The slope efficiency, η_{SE}, is also extracted (green dotted lines), where the REPCSEL has η_{SE} = 14.1 mWA^{-1}, PCSEL with η_{SE} = 3.4 mWA^{-1}. The calculated threshold current density of REPCSEL and PCSEL is 421 Acm^{-2} and 569 Acm^{-2}. As previously reported, [13] the coupling coefficients of the PCSEL and REPCSEL are

κ_{1D} = 113.2 cm^{-1}, κ_{2D} = 2.4 cm^{-1}, $\kappa_{\perp}$ = 1 cm^{-1}, κ_i = 5 cm^{-1} which can be directly used as the input parameters of the PMC model. The period of the PC is 0.4 um, which gives 1000 #PC. Using the PMC model with these input parameters, the in-plane loss of REPCSEL and PCSEL are determined to be 5.5 cm^{-1} and 39.6 cm^{-1}, respectively.

Figure 4.12 (b) plots the current density-gain (J-G) characteristics of the active material used in this PCSEL/REPCSEL. This was obtained by length dependent characterization of broad area lasers. Fitting of the J-G characteristics of the active element (green dotted line) was made using:

$$J_{th} = J_0 exp(g_{th}/g_0) \qquad equation\ 4.2$$

Where J_{th} is threshold current density, J_0 is transparent current density, g_{th} is threshold gain, g_0 is transparent gain. This yielded J_0 = 380 Acm^{-2} and g_0 = 120 cm^{-1}.

I now use the following equation for η_{SE} to continue the fitting:

$$\eta_{SE} = \frac{1.24}{\lambda}(1-A)\eta_i \frac{\frac{1}{2}\left(1+2\sqrt{R}\cos\theta+R\right)\alpha_{\perp}}{\left(1+\sqrt{R}\cos\theta\right)\alpha_{\perp}+\alpha_{//}+\alpha_i} \qquad equation\ 4.3$$

Where λ is the lasing wavelength, in this case, 1.295 um. A is an absorption constant, defining the ratio of the power absorbed in the substrate to the total output power, which is assumed to be 0.1. η_i is the internal quantum efficiency of the quantum well, which was measured to be 0.5. R is the reflectivity of the vertical mirror, which in this case R represents the reflectivity of the p-contact and is estimated to be 0.4 [5]. With the parameters above, the aforementioned PMC simulated values for $\alpha_{//}$, a single fit parameter of the radiative rate (5.0 cm^{-1}) is used. The calculated slope efficiency of REPCSEL and PCSEL are 14.2 mWA^{-1} and 3.4 mWA^{-1}, and the threshold gain values are 11.8 cm^{-1} and 44.9 cm^{-1}, respectively. These points are plotted in green (slope and threshold) in figures 4.12 (a) and (b). A very good agreement with experimental results is obtained in both cases.

4.8 Summary

In this chapter, the PMC model is used to analyse commonly used PCSEL designs. We begin with a PCSEL having its electrode and PC of the same size. The PMC model was initially used to analyse the effects of coupling coefficients on in-plane loss of such design. As the PMC model is not limited by the materials or design of the PC pattern, arbitrary values of coupling coefficients can be applied for the purpose of exploration. The original value of coupling coefficients is extracted from literature, and multiplication factors (0.5, 1, 2 & 3) were used to

enlarge or reduce them. To eliminate the influence caused by the difference between original reported in-plane coupling coefficients, the case when $\kappa_{1D} = \kappa_{2D} = 500$ cm^{-1} and M = 0 is considered. All cases show that with larger coupling coefficients, the in-plane loss reduces and is a function of the size of PCSEL (PC Number). κ_{1D} is shown to have an advantage in reducing in-plane loss as compared with κ_{2D}. However, to effectively zero in-plane loss the PCSEL size and PC scattering values would need to be unreasonable large. This is a key result, as it points out that more and more complex PC structures to increase coupling are fundamentally unable to solve the issue of high additional parasitic losses in PCSELs. Different routes are required.

An in-plane mirror was then considered; it was simply defined as an in-plane power reflector on the boundary of a square lattice PC. The result shows that in-plane loss decreases when reflectivity becomes greater, and in-plane loss could be zeroed in modestly large scale PCSELs with large reflectivity. To further explore the effect, a structural engineered reflection was then defined within the PMC model. The result shows that even though engineering in-plane reflection has potential in controlling near-field pattern, the reduction of in-plane loss is significantly weakened. The development of the REPCSEL was then discussed. The PMC model plays an important role in analysing the optical loss of the REPCSEL to explore the point at which a resonator effect occurs within the PCSEL. It was shown that for given values of κL, a resonator effect can be realised. The model was also shown to provide insight into the mode selection caused by in-plane mirror.

Similarly, the PMC model is used to predict the gain threshold and slope efficiency of a PCSEL and REPCSEL with the same design except for the presence/absence of in-plane boundary mirrors.

4.9 Future work

For a modest sized, conventional designed PCSEL, enhancing κ1D and κ2D is not significantly reduce the in-plane loss, α//. Some existing research reports that large area PCSELs with small value of κ2D still has significant α//. In conclusion, engineering PC shape is not the route for α// minimization.

Compared to the most conventional design, applying boundary reflection is a better route. The similar idea has been pursued experimentally [13, 17] and in simulation [18]. Based on the effects of varying perimeter reflectivity explored in this chapter, it would be interesting to make PCSEL with selectable mirrors. Referencing the existing design, [19] a unique type of laser diode with contact covering mirrors which individually control the mirrors. This design will

make it possible to modify the beam shape and possibly central position with some elements of beam steering.

In next chapter, the PMC model is extended to simulate another conventional design of PCSEL, which includes an absorptive loss in PC telling the difference between pumped and unpumped PC region.

References

[1]. Peng, CY., Cheng, HT., Hong, YH. *et al.* Performance Analyses of Photonic-Crystal Surface-Emitting Laser: Toward High-Speed Optical Communication. *Nanoscale Res Lett* **17**, 90 (2022). https://doi.org/10.1186/s11671-022-03728-x

[2]. K. Hirose, Y. Liang, Y. Kurosaka et al., "Watt-class high-power, high-beam-quality photonic-crystal lasers," Nature Photon., vol. 8, pp. 406–411, 2014, doi: 10.1038/nphoton.2014.75.

[3]. J. Liu, Y. Gao, P. Ivanov, P. Harvey, and R. Hogg, "Probabilistic Markov chain modeling of photonic crystal surface emitting lasers," Appl. Phys. Lett., vol. 123, no. 26, 2023, Art. no. 261107, doi: 10.1063/5.0168073.

[4]. K. Sakai, E. Miyai, and S. Noda, "Coupled-wave model for square-lattice two-dimensional photonic crystal with transverse-electric-like mode," Appl. Phys. Lett., vol. 89, no. 2, 2006, Art. no. 021101, doi: 10.1063/1.2220057.

[5]. T. Inoue, T. Kim, S. Katsuno et al., "Measurement and numerical analysis of intrinsic spectral linewidths of photonic-crystal surface-emitting lasers," Appl. Phys. Lett., vol. 122, no. 5, 2023, Art. no. 051101, doi: 10.1063/5.0135042.

[6]. Y. Liang, C. Peng, K. Ishizaki et al., "Three-dimensional coupled-wave analysis for triangular-lattice photonic-crystal surface-emitting lasers with transverse-electric polarization," Opt. Express, vol. 21, no. 1, pp. 565–580, 2013, doi: 10.1364/OE.21.000565.

[7]. Y. Liang, C. Peng, K. Sakai, S. Iwahashi, and S. Noda, "Three-dimensional coupled-wave analysis for square-lattice photonic crystal surface emitting lasers with transverse-electric polarization: finite-size effects," Opt. Express, vol. 20, no. 14, pp. 15945–15961, 2012, doi: 10.1364/OE.20.015945.

[8]. Y. Yang, C. Peng, Y. Liang, Z. Li, and S. Noda, "Three-dimensional coupled wave theory for the guided mode resonance in photonic crystal slabs: TM-like polarization," Opt. Lett., vol. 39, no. 15, pp. 4498–4501, 2014, doi: 10.1364/OL.39.004498.

[9]. T. Inoue, R. Morita, M. Yoshida, M. De Zoysa, Y. Tanaka, and S. Noda, "Comprehensive analysis of photonic-crystal surface-emitting lasers via time-dependent three-dimensional coupled-wave theory," Phys. Rev. B, vol. 99, no. 3, 2019, Art. no. 035308, doi: 10.1103/PhysRevB.99.035308.

[10]. K. Emoto, T. Koizumi, M. Hirose et al., "Wide-bandgap GaN-based watt-class photonic-crystal lasers," Commun. Mater., vol. 3, p. 72, 2022.

[11]. M. Yoshida, M. De Zoysa, K. Ishizaki et al., “Double-lattice photonic-crystal resonators enabling high-brightness semiconductor lasers with symmetric narrow-divergence beams,” Nature Mater., vol. 18, pp. 121–128, 2019, doi: 10.1038/s41563-018-0242-y.

[12]. M. Yoshida, M. De Zoysa, K. Ishizaki et al., “Double-lattice photonic-crystal resonators enabling high-brightness semiconductor lasers with symmetric narrow-divergence beams,” J. Phys. Photonics, vol. 3, no. 2, 2021, Art. no. 022006, doi: 10.1088/2515-7647/abea06.

[13]. Z. Bian, X. Zhao, J. Liu et al., “Resonator embedded photonic crystal surface emitting lasers,” npj Nanophoton., vol. 1, p. 13, 2024, doi: 10.1038/s44310-024-00014-9.

[14]. Y. Cheng, J. Pan, S. Liang, W. Feng, Z. Liao, F. Zhou, B. Wang, L. Zhao, H. Zhu, and W. Wang, "Butt-coupled MOVPE growth for high-performance electro-absorption modulator integrated with a DFB laser," J. Crystal Growth, vol. 308, no. 2, pp. 297–301, 2007, doi: 10.1016/j.jcrysgro.2007.09.004.

[15]. L. Hou, M. Haji, J. Akbar, J. H. Marsh, and A. C. Bryce, "AlGaInAs/InP monolithically integrated DFB laser array," IEEE J. Quantum Electron., vol. 48, no. 2, pp. 137–143, Feb. 2012, doi: 10.1109/JQE.2011.2174455.

[16]. Z. Bian, "Chapter 5. Resonator Embedded Photonic Crystal Surface Emitting Lasers (REPCSEL)," in InP-based Photonic Crystal Surface Emitting Lasers, James Watt School of Science and Engineering, University of Glasgow, Glasgow, UK, 2023, pp. 116-138.

[17]. D. Moodie, "PCSELs at telecommunications wavelength using a heterolattice design", International PCSEL workshop 2025, Glasgow, United Kingdom, Nov 08-12.

[18]. T. Inoue, T. Kim, S. Katsuno, R. Morita, M. Yoshida, M. De Zoysa, K. Ishizaki, and S. Noda, “Measurement and numerical analysis of intrinsic spectral linewidths of photonic-crystal surface-emitting lasers,” *Appl. Phys. Lett.*, vol. 122, no. 5, p. 051101, Jan. 2023, doi: 10.1063/5.0135042.

[19]. R. J. E. Taylor et al., "Coherently Coupled Photonic-Crystal Surface-Emitting Laser Array," in IEEE Journal of Selected Topics in Quantum Electronics, vol. 21, no. 6, pp. 493-499, Nov.-Dec. 2015, Art no. 4900307, doi: 10.1109/JSTQE.2015.2417998.

Chapter 5: Loss Simulation of PCSELs with an Unpumped Boundary Region

5.1 Introduction

It is common in PCSEL design to make the PC region larger than the contact (electrically driven) to reduce the in-plane loss [1-7]. To the best of my knowledge, the PCSEL literature does not make a distinction between the pumped and unpumped PC regions in terms of its gain or absorption characteristics. This work considers the effect of self-absorption by the active elements in the unpumped boundary region. The effect on internal loss of the device as well as the in-plane loss is explored for a range of design parameters. The PMC model is used to simulate and explore this commonly used PCSEL design. An example GaAs-based PCSEL from the literature [1] is simulated [8-9]. The PC region is divided into two parts and defined as a pumped region (considered to be the same size as the contact) and a unpumped boundary (outside of contact, having width W). As the number of quantum wells in the active region of the reported device is not given, nor the detuning of the PCSEL emission wavelength to the gain peak, the absorption is determined numerically. Then, a current spreading analysis is carried out, concluding that current spreading has a much smaller characteristic length than the leakage of photons in-plane. The interlinkage of the in-plane loss and internal loss is shown by varying the un-pumped boundary width for a given contact size (this is simulated for 1 to 3 quantum wells, and different detuning. Finally, two reports from the literature using an unpumped PC boundary are analysed. The are state-of-the-art GaAs [3-4] and GaN [7] PCSELs.

5.2 Study of Quantum Well Absorption in a GaAs PCSEL

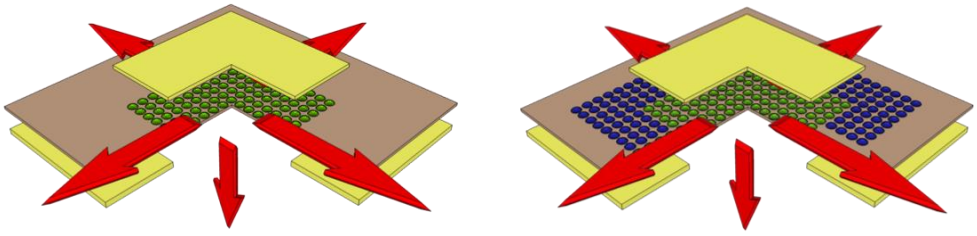

Figure 5.1: (a) Schematic of a PCSEL device without unpumped region, (b) Schematic of a PCSEL device

In previous chapters, the simulated devices had equivalent PC region (total #PC) and electrode (or p-contact) sizes [10]. A schematic of such devices is shown in figure 5.1 (a). The common design choice that the PC array has slightly larger size [1-7] than the electrode is shown in

figure 5.1 (b), green dots are PC that covered by electrode (in gain), and blue dots are PC outside of the area of contact (lossy).

Layer	Material	Thickness (um)	Doping Concentration (cm^{-3})	Structure
9	GaAs	0.2	1×10^{19}	Current Spreading
8	AlGaAs	1.8	1×10^{18}	p-Cladding
7	GaAs	0.235	4×10^{17}	PC
6	GaAs	0.065	-	Intrinsic Layer
5	GaAs	0.008	-	
4	InGaAs	0.01	-	Active Region
3	GaAs	0.058	-	
2	AlGaAs	2	1×10^{18}	n-Cladding
1	AlGaAs	150	1.5×10^{18}	Substrate

Table 5.1: The device structure for current spreading simulation [1]

Here, the parasitic loss is defined as:

$$\alpha_{parasitic} = \alpha_{//} + \alpha_i \qquad equation 5.1$$

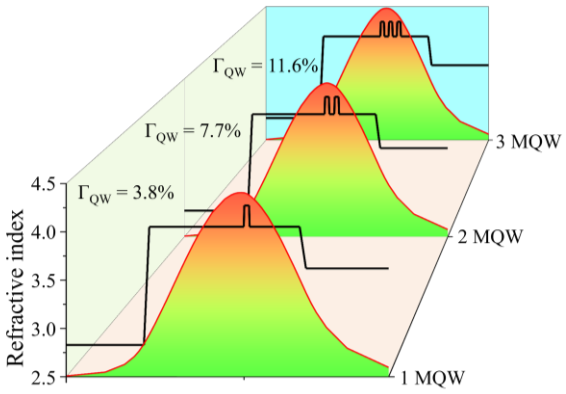

Figure 5.2: Schematic of the mode-profile of the simulated PCSEL device as a function of MQW number. Confinement factor, Γ_{QW}, (overlap of the MQW and mode) is shown for each case.

To determine the value of self-absorption in the unpumped region, the reported epitaxy structure [1] (table 5.1) is simulated. Figure 5.2 shows the schematic of the overlap of the optical mode and different repeats of the quantum well (single, double and triple QW are shown). The optical mode is expanded in terms of eigenmodes. Then use photon rate equations to describe the intensity within these modes. The equations are solved fully coupled with the electro-thermal transport. (Simulated by Rsoft/LaserMOD) The confinement factor (Γ_{QW}) represents the overlap of QW on simulated optical mode. Figure 5.2 shows the schematics of such overlap, confinement factor of one, two and three repeats of QW are 3.8%, 7.7% and

11.6%. The reason of non-linear increase of value may be due to imperfect matching between the QW and optical mode.

PCSEL Wavelength (nm)	Material Gain (cm^{-1})	Quantum Well Absorption (cm^{-1})		
		1QW	2QW	3QW
970	-917	-35	-70	-106
965	-1602	-61	-123	-185
960	-2270	-87	-174	-262

Table 5.2: Quantum well absorption coefficients in the un-pumped perimeter region at three PCSEL operating wavelengths as a function of quantum well number.

With the same epitaxy structure, material gain is simulated based on an 8×8 KP band structure calculation for a 3-repeat TE-polarization QW. It can be known from figure 5.3 that the simulated material gain of the device is as a function of carrier density. 965 nm is reported as gain-spectrum peak, results of 960 nm and 970 nm (±5 nm detuning) are also analysis for comparison. The inset of figure 5.3 shows the gain at the three considered wavelength, 960 nm (blue dots), 965 nm (black dots) and 970 nm (red dots). The absorption loss has been calculated by considering both the gain and confinement factor of QW, the result is shown in table 5.2.

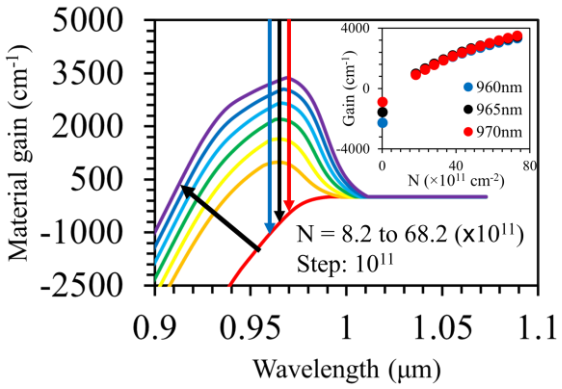

Figure 5.3: Calculated material gain spectrum for InGaAs/AlGaAs quantum well at room temperature as a function of carrier density. Inset shows the material gain at three operating wavelengths as a function of carrier density and the zero-carrier absorption.

5.3 Study of Current Spreading in GaAs PCSEL

Besides the value simulation above, the area of pumped and unpumped region also need to be defined. In semiconductor, a current spreading phenomenon occurs due to the movement of electrons driven by carrier concentration gradients and electric fields. [11-13] Due to which, there should be a grating region between pumped and unpumped region. So, in this section, a current spreading analysis is done by LaserMOD to find out the effect of such grating region.

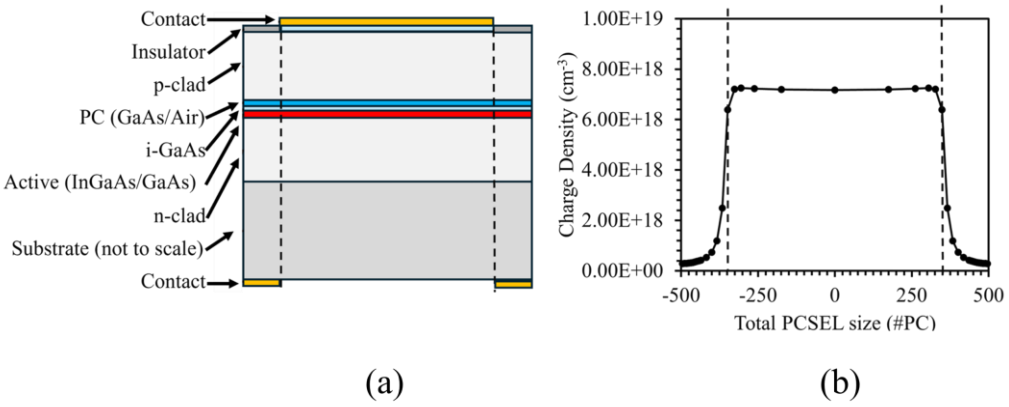

Figure 5.4: (a) Schematics of simulated PCSEL devices with p-contact size of 200 um. (b) Simulated spatial charge density on PCSEL.

Figure 5.4 (a) shows the simulated structure. [1] The simulation of carrier density is done by solving the carrier continuity equations and Poisson's equation, along with the Schrödinger equation for charge distribution in the QWs. A square size p-contact is set to 700 × 700 PC atoms which fits the n-window size. Figure 5.4 (b) shows the simulated charge density condition of QW when applying 200 mA to it. It can be known from the result that, the current spreads evenly on QW within the p-contact area (described also as pumped region), which proves that the internal loss is constant within the area. A 50% reduction in carrier density is indicated at approximately 10 #PC atoms away from pumped region, and the value reduces to less than 10% at 30 #PC atoms in distance, then eventually reduces to almost zero. As a result, the variation area of the quantum self-absorption between pumped region and unpumped region is very small (~30 #PC) compared to the pumped region (or p-contact size). So, the effect of the current spreading issue is relatively small, so will not be considered in following simulations.

5.4 Effect of Unpumped Region on PCSEL Parasitic Losses

With preparations above, the PCSELs with fixed size (700×700 #PC) and various width of unpumped region are simulated by PMC model in this section. The in-plane coupling coefficients and internal loss are regarded as constant, and applied to all PC region with values of, $\kappa_{1D} = 1334\ cm^{-1}$, $\kappa_{2D} = 386\ cm^{-1}$, $\alpha_i = 5\ cm^{-1}$. For the unpumped region, there is no power injection and an extra loss caused by quantum well, κ_{ab} has been applied, of which the value is shown in table 5.2. And as mentioned above, this simulation does not consider absorption bleaching.

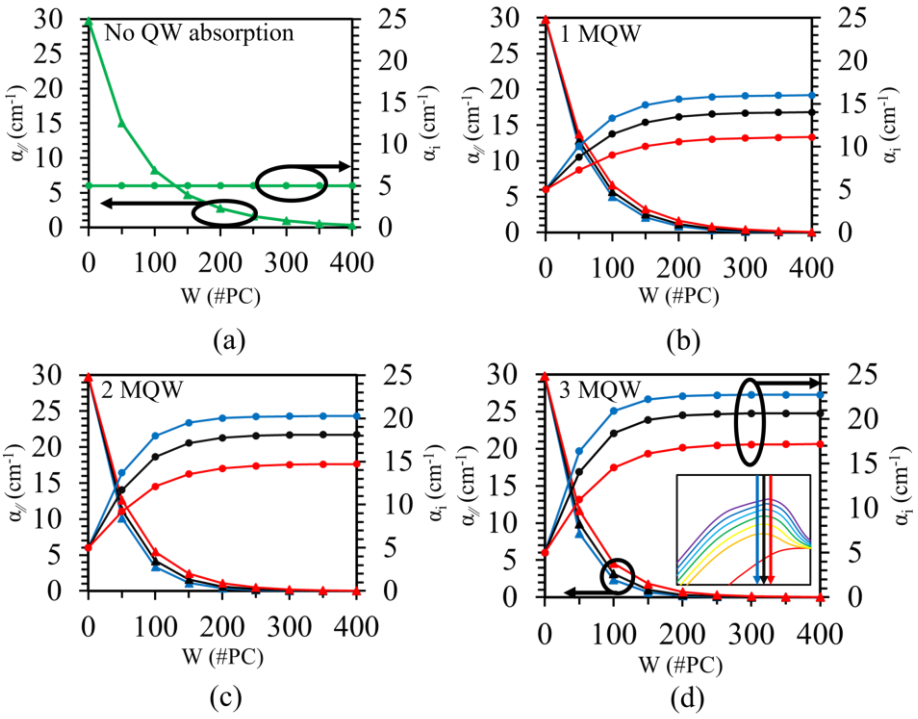

Figure 5.5: Simulated in-plane and internal loss as a function of un-pumped perimeter PCSEL width W, for (a) no QW absorption, (b) 1 QW, (c) 2 QW, (d) 3 QW. Values are determined using different PCSEL operating wave-lengths (960nm, 965nm, 970nm) as shown in the inset to (d).

Figure 5.5 plots the simulated in-plane loss and internal loss as a function of the width of the unpumped region W. In (a), κ_{ab} is not applied to PCSELs, the unpumped region has same internal loss as pumped region, (b), (c) and (d) has 1, 2 and 3 QW absorption applied. For the case shown in figure 5.5 (a), the internal loss remains a constant value, and the in-plane loss tends towards zero as the width of unpumped region increasing. With considering the convergence limit (0.1 cm^{-1}) of PMC model in this simulation, and the values of in-plane coupling coefficients used here, the zeroing of in-plane loss occurs at around W = 400 #PC in case (a). For cases with the introduction of QW absorption (figure 5.5 (b), (c) and (d)), an increase in internal loss with increasing W and a corresponding reduction in in-plane loss is observed. This is due to the QW self-absorption is regarded as a part of internal loss in this simulation. It should be noted from the comparison of figure (b) to (d), that this increase is as a function of detuning of the lasing peak to the gain spectrum peak (blue, black and red dots are 960 nm, 965 nm and 970 nm). In these cases, the in-plane loss is essentially zeroed at W = 350 #PC. The internal loss also reaches a constant value beyond that W, and is as a function of the detuning of the emitting wavelength and the gain-spectrum peak. It can be concluded that, an interdependence between in-plane loss and internal loss has occurred with introducing unpumped region to PCSEL. Decreasing the number of QWs is possible to reduce the width of

the boundary PC at which the in-plane loss is zeroed, however at the same time, the constant value of internal loss at such width becomes higher.

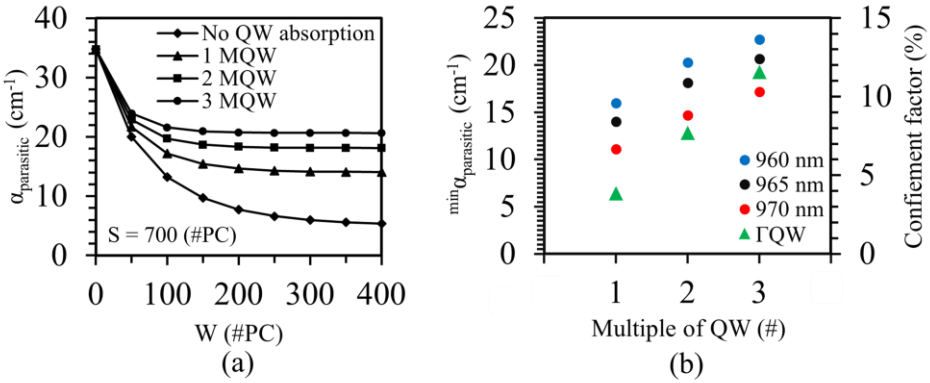

Figure 5.6: (a) Total parasitic loss as a function of un-pumped region W for different QW number (including intrinsic loss alone) for the three PCSEL operating wavelengths. (b) Minimum parasitic loss and confinement factor as a function of different QW number for the three PCSEL operating wavelengths.

As defined before, the parasitic loss describes the sum of in-plane loss and internal loss, and is plotted as a function of the width of unpumped boundary in figure 5.6 (a). The plot data is the case when PCSEL emission perfectly aligns with the gain spectrum peak (965 nm). To explore the effect of QW absorption, 1, 2, and 3 QWs are considered to compare with the case without QW absorption. The parasitic loss shows a decreasing trend with increasing W, and will be minimized but not zeroed eventually. Due to the interdependence between in-plane loss and internal loss, for large W, when in-plane loss is zeroed, total parasitic loss is dominated by internal loss and reaches a minimum value ($^{min}\alpha_{parasitic}$). The parasitic loss increases when QW number increase as the fraction of light lost radiatively in the unpumped region reduces, due to the competing power loss channels in absorption. Figure 5.6 (b) is the minimum parasitic loss as a function of QW number and lasing wavelength detuning to the gain-spectrum peak. It also plots the QW confinement factor as a function of MQW number for the reference and note the strong correlation between QW overlap and minimum parasitic loss.

5.5 Analysis 1: GaAs-based Double Lattice PCSEL

In this section, another GaAs-based double lattice PCSEL with unpumped region from an experimental-based literature is simulated. [3-4] The PCSEL device was designed and fabricated for constructing a LiDAR system that uses no external lens system in its light source and to demonstrate highly spatially resolved time-of-flight sensing.

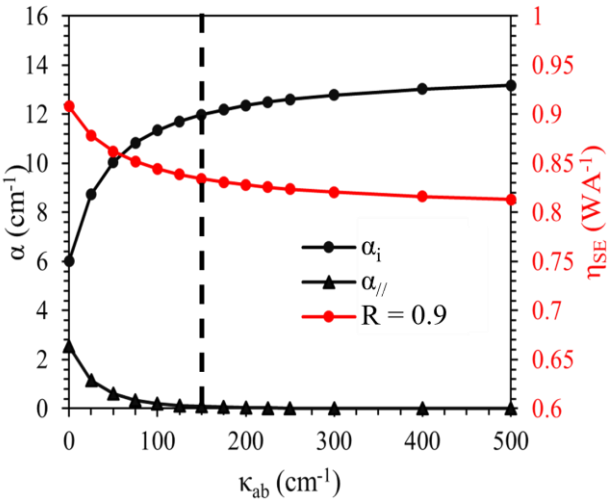

Figure 5.7: Simulated internal loss, in-plane loss and slope efficiency as a function of quantum well absorption when vertical reflectivity is 0.9.

The input parameters for PMC model are partly given and partly extracted from the experimental results, e.g. the measured light-current curve. Size of pumped region S = 1790 #PC, unpumped region W = 360 #PC, period a = 0.28 um, in-plane coupling coefficients κ_{1D} = 300 cm^{-1}, κ_{2D} = 200 cm^{-1}, radiation loss $\alpha_{\perp}$ = 16 cm^{-1}, internal loss α_i = 6 cm^{-1}. The quantum well absorption loss, κ_{ab} = 150 cm^{-1} which is assumed according to the previous simulation (table 5.2), the vertical reflectivity R = 0.9.

To clarify how κ_{ab} affects the microscopic scattering mechanism the coupling probabilities among PCs are defined below, for pumped region:

$$P_{forward} = 1 - P_{1D} - 2 * P_{2D} - P_{\perp} - P_i \qquad equation 5.2$$

For unpumped region:

$$P_{forward} = 1 - P_{1D} - 2 * P_{2D} - P_{\perp} - P_i - P_{ab} \qquad equation 5.3$$

P_{ab} here stands for the probability of power lost by quantum well absorption.

According to the measured LI curve, the slope efficiency of mentioned device is 0.835 WA^{-1}. The reported parasitic losses are in-plane loss $\alpha_{//}$ = 3 cm^{-1} and internal loss α_i = 6 cm^{-1}. Figure 5.7 plots the PMC simulated parasitic losses (in-plane loss is black triangular dots, internal loss is black circular dots) and the calculated slope efficiency (red dots) as a function of quantum well absorption. For the case κ_{ab} =150 cm^{-1}, the PMC model simulated parasitic losses are, $\alpha_{//}$ < 0.1 cm^{-1} and α_i = 12.1 cm^{-1}, which is not as reported in literature. However, the calculated slope efficiency is 0.835 WA^{-1} which has a great match with the reported measured result. This may be due to that the value of internal loss is simulated without considering the difference

between pumped and unpumped region in literature. As discussed in earlier chapter, the unpumped region has very different loss condition, and the introduction of quantum well absorption makes the value of internal loss not a constant anymore, which is the main reason the in-plane loss decreases in this design.

Although the PMC model simulated result does not explain the loss condition in the same way as the literature does, it accurately predicts the device-level parasitic losses of the target PCSEL device. The difference appears to be in the definition of $\alpha_{//}$ and α_i. In the report discussed above, the calculated total parasitic loss has the same value as reported. This is reconciled if the authors are attributing absorptive loss in the unpumped region to $\alpha_{//}$, rather than α_i.

5.6 Analysis 2: GaN-based PCSEL

The analysis of PMC model on InP-based and GaAs-based PCSELs were discussed earlier. To ensure the PMC model fits GaN, another popular III-V material used in semiconductor lasers, an analysis of PMC model on a target GaN-based PCSEL from literature has been done in this section.

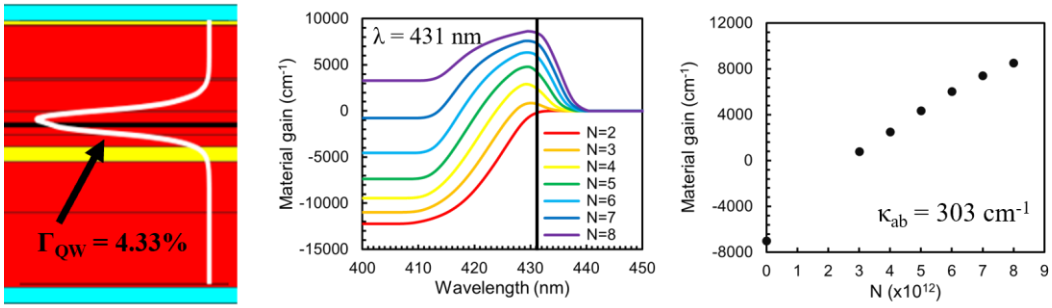

Figure 5.8: (a) The simulated optical mode of a GaN-based PCSEL overlaps on the schematic of its epitaxy structure. (b) Simulated material gain as a function of wavelength with various injection of current density

A CW operated, 300 um radius in size PCSEL device with filling factor (air hole) of 8.8% in the literature is used as the target of the simulation. The reported in-plane coefficients are κ_{1D} = 460 cm^{-1}, κ_{2D} = 35 cm^{-1}. The reported internal loss is α_i = 2 cm^{-1}. A p-electrode reflectance simulation has been discussed in literature, based on which the vertical reflectivity used in this simulation is R = 0.8. The slope efficiency is extracted from a measured LI curve, which with the value of η_{SE} = 0.85 WA^{-1}.

According to the schematic reported in literature, the target device uses the design discussed in this chapter, with unpumped boundary. To explore the value of quantum well absorption (κ_{ab}),

a simulation with provided epitaxy structure of the target device has been done (method discussed in previous chapter). Figure 5.8 (a) shows the simulated optical mode (white solid line) of the target device overlapping on the schematic of given epitaxy structure. The calculated confinement factor of 2 QW (reported active region) is 4.33%. Figure 5.8 (b) plots the simulated material gain as a function of wavelength. Injecting carrier density, N varies from 2-8 $\times 10^{12}$ cm^{-2}. The gain-peak wavelength matches the reported lasing wavelength, 431 nm. Figure 5.8 (c) plots the material gain at λ = 431 nm as a function of carrier density. The predicted material gain is g_0 =~7000 cm^{-1} (N = 0), and the calculated quantum well absorption loss ($\kappa_{ab} = \Gamma_{QW} \times g_0$), κ_{ab} = 303 cm^{-1} which will be applied to unpumped region.

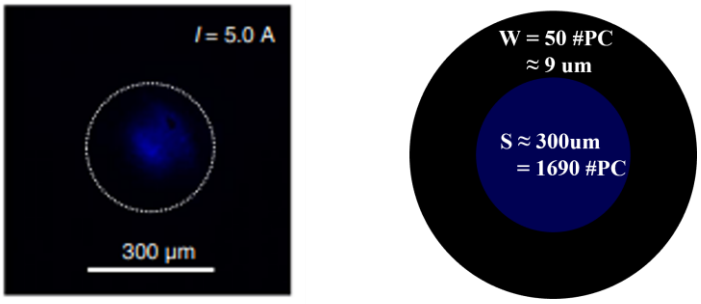

(a) (b)

Figure 5.9: (a) Measured near-field pattern of target device reported by literature. (b) Assumed operation circumstances of target device.

According to the measured near-field pattern (shown in figure 5.9 (a)), the target device is assumed to emit as shown in figure 5.9 (b). When absorptive boundary has width, W = 50 #PC the simulated parasitic losses are, $\alpha_{//}$ = 2.2 $cm^{-1}$and α_i = 5 cm^{-1}. The calculated slope efficiency is, η_{SE} = 0.845 WA^{-1}, which has <~5% difference compared to reported measured result. Again, the PMC model may be used to describe the operation of this PCSEL in terms of device-level loss parameters.

5.7 Summary

In this chapter, a common accepted design, PCSEL with an unpumped boundary has been introduced to PCSEL devices. The PMC model is used to define this boundary and explore its effect. By analysing a GaAs-based PCSEL from literature, [1] a quantum well absorption has been realized, the effect is named by the photon absorption behaviour happening on the unpumped region and numbered by simulating a reported epitaxy structure from same literature. As defined, the absorption loss is considered as a part of internal loss. When exploring the

value, the number of quantum well and gain-spectrum peak detuning are also considered. It can be concluded that, just like intuition, the in-plane loss is reduced when introducing these unpumped region and as a function of the width of it. It should be noted that the value of in-plane loss can be zeroed when proper width of boundary is applied. However, this reduction realized with a cost, the internal loss significantly increases when having thicker boundary. Due to the independency between in-plane loss and internal loss, it is not fair to design a PCSEL with considering just one of them, so a parasitic loss is defined to show the total value of unwanted losses. The parasitic loss reduces and eventually reaches a minimum value when increasing the width of unpumped region but increases when having more repeat of quantum well. In conclusion, blindly increase the width of unpumped region may not realize the best performance of PCSELs, and for some cases, using less repeat of QW might reduce the parasitic loss more. At last, another GaAs-based PCSEL and a GaN-based PCSEL has been analysed by the same method in the PMC model. The results show that PMC model has good advantage in analysing these PCSEL devices with unpumped boundary.

5.8 Future Work

As discussed in this chapter, the new defined parasitic loss represents the total unwanted losses of PCSEL device. So, minimizing it can be regarded as a way to engineering the power conversion efficiency (PCE). Introducing unpumped boundary and engineering its width reduces the parasitic loss but the effect is limited by the size of pumped region. Using a smaller number of QW also reduces the parasitic loss, however, the total gain will reduce at the same time, which limits the application circumstance. Using in-plane mirrors without unpumped region which discussed in previous chapter reduces in-plane loss and has a constant internal loss, so the parasitic loss decreases too. However, the mirror may create extra loss based on experiments, and the high reflectivity of mirror may enhance the 1D coupling in orthogonal directions, which reduces threshold gain but brings bad far-field pattern. Also, theoretically in-plane loss can be reduced if all coupling coefficients are very high, multi-mode operating may appear.

In conclusion, all above discussed constructions may theoretically reduce the value of parasitic loss, but all have obvious disadvantages or suitable for narrow circumstances. For industrial consideration, the power conversion efficiency (PCE) might be an indicator that are given more priority for consideration compared with specific optical losses. In next chapter, several novel design of PCSELs based on the absorbing boundary (or solving the unwanted self-absorption

loss) to enhance the PCE is considered.

References

[1]. K. Hirose, Y. Liang, Y. Kurosaka *et al.,* "Watt-class high-power, high-beam-quality photonic-crystal lasers," *Nature Photon*., vol. 8, pp. 406–411, 2014, doi: 10.1038/nphoton.2014.75.

[2]. K. Emoto, T. Koizumi, M. Hirose *et al.,* "Wide-bandgap GaN-based watt-class photonic-crystal lasers," *Commun. Mater*., vol. 3, p. 72, 2022.

[3]. M. Yoshida, M. De Zoysa, K. Ishizaki *et al.,* "Double-lattice photonic-crystal resonators enabling high-brightness semiconductor lasers with symmetric narrow-divergence beams," *Nature Mater*., vol. 18, pp. 121–128, 2019, doi: 10.1038/s41563-018-0242-y.

[4]. M. Yoshida, M. De Zoysa, K. Ishizaki *et al.,* "Double-lattice photonic-crystal resonators enabling high-brightness semiconductor lasers with symmetric narrow-divergence beams," *J. Phys. Photonics*, vol. 3, no. 2, 2021, Art. no. 022006, doi: 10.1088/2515-7647/abea06.

[5]. M. Nishimoto, K. Ishizaki, K. Maekawa, K. Kitamura and S. Noda, "Photonic-crystal surface-emitting laser," *Appl. Phys. Express*, vol. 6, no. 4, 2013, Art. no. 042002, doi: 10.7567/APEX.6.042002.

[6]. Y. Kurosaka, S. Iwahashi, Y. Liang *et al.,* "On-chip beam-steering photonic-crystal lasers," *Nature Photon*., vol. 4, pp. 447–450, 2010, doi: 10.1038/nphoton.2010.118.

[7]. H. Matsubara, S. Yoshimoto, H. Saito *et al.,* "GaN photonic-crystal surface-emitting laser at blue-violet wavelengths," *Science*, vol. 319, no. 5862, pp. 445–447, 2008.

[8]. J. Liu, X. Zhao, Z. Bian *et al.,* "Interdependence of parasitic losses in photonic crystal surface emitting lasers," *AIP Advances*, vol. 15, no. 4, 2025, Art. no. 045321, doi: 10.1063/5.0252646.

[9]. J. Liu, Y. Gao, P. Ivanov, P. Harvey, and R. Hogg, "Probabilistic Markov chain modeling of photonic crystal surface emitting lasers," *Appl. Phys. Lett.*, vol. 123, no. 26, 2023, Art. no. 261107, doi: 10.1063/5.0168073.

[10]. Z. Bian, X. Zhao, J. Liu *et al.,* "Resonator embedded photonic crystal surface emitting lasers," *npj Nanophoton*., vol. 1, p. 13, 2024, doi: 10.1038/s44310-024-00014-9.

[11]. *Solid State Electronic Devices* (B.G. Streetman & S. Banerjee, 7th Ed., 2014, Pearson)

[12]. *Physics of Semiconductor Devices* (S.M. Sze & K.K. Ng, 3rd Ed., 2006, Wiley)

Chapter 6: Exploring High Power Conversion Efficiency PCSELs

6.1 Introduction

Applying unpumped photonic crystal (PC) boundaries is a conventional route to enhance PCE. [1-7] In last chapter, the loss mechanism of PCSELs was explored with this commonly used structure and analysed a GaAs-based PCSEL and a GaN-based PCSEL with such design. Introducing self-absorption loss due to the unpumped quantum well active element in the unpumped boundary region, it was shown that the in-plane loss ($\alpha_{//}$) and internal loss (α_i) of the PCSEL are interlinked. [8] This new-found interdependence proves that simply minimizing in-plane loss is not the key strategy in PCSEL development, but should focus on reducing this self-absorption loss.

In this chapter this simulation is extended to explore a range of device designs to minimize parasitic loss in PCSELs by removing this self-absorption. The chapter begins by describing the device types to be explored. The inputs and outputs to the simulation are then described. The effects of butt-coupled passive sections in the boundary PC region, selective area intermixing the active element in the boundary PC region and using a second contact to the boundary PC are explored. The additional contact device renders the boundary transparent, whilst the other two approaches maintain an internal loss only.

Various characteristics of these techniques are explored and the PCE for an exemplary 1 W source are discussed. For the butt-coupled device the fabrication related issues of scattering loss at the etched/regrown waveguide interface are considered. For the selective area intermixed device, the lateral extent of the transition from active to passive wavelengths is also considered. Additional waste power is included in the case of the dual contact device in terms of the calculation of PCE. A critical comparison of approaches is made, and possible future research avenues discussed.

6.2 Device Types

In previous chapters, two conventional design of PCSELs have been discussed. It was shown that applying absorptive boundary to pumped PC region (discussed in chapter 5) has significant advantages in reducing in-plane loss compared to the older design (discussed in chapter 4). However, internal loss increased. So, in this chapter, novel PCSEL designs are explored based on same pumped PC region, but using elements of photonic integration to enhance PCE. Results are then compared with absorptive boundary PCSELs.

Figure 6.1 shows a schematic of different designs of PCSEL devices and their respective spatial loss/gain conditions. It should be clarified that the schematic PC (dots) in figure 6.1 are not to real scale, with the active element containing several hundreds of PC atoms on one side. The yellow dots schematics shown in figure 1 represent the contact-covered PC atoms, that are in gain, and lasing. It has been discussed in previous studies that the current spreading region is small compared to the leakage of photon into the surrounding PC boundary, so the transition between gain and loss is considered to be abrupt in this study. [8]

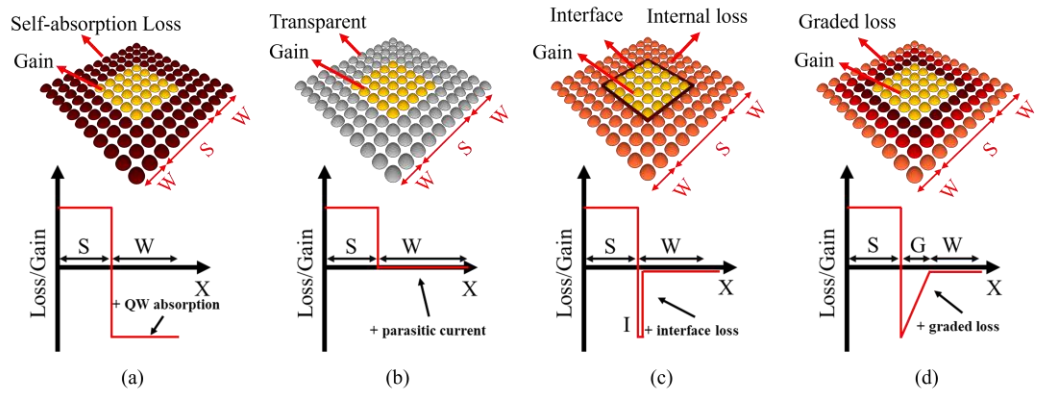

Figure 6.1: Schematic and loss/gain as a function of the distance to device center of different geometry of

Figure 6.1(a) is PCSEL with an absorptive boundary (dark red dots), in which the PCs are not pumped and have self-absorption loss caused by the absorptive QWs in the PC boundary region. [8] The schematic graph indicates the loss/gain characteristics of the active element, where outside the contact, the propagating optical power is subject to self-absorption in the unpumped quantum wells. This device schematic represents current approaches to minimizing parasitic loss [1-7]. The design has been analysed, and the interconnection of in-plane loss and internal loss has been highlighted in previous studies [8]

Figures 6.1 (b) and 6.1 (c) consider widely utilized monolithic integration technologies to realize passive boundary PC elements. Figure 6.1 (b) is a PCSEL utilizing butt-coupled waveguide technology. Here etching of the active element and epitaxial regrowth of a passive waveguide are employed to realize active and passive regions. This technology is a critical building block for large scale InP photonic integrated circuits. However, this process introduces scattering loss at the active/passive butt-coupled interface. It is accommodated in our model as an additional loss in a single PC atom thick boundary layer between gain and passive sections, as indicated in the schematic graph of loss/gain.

Figure 6.1 (c) is PCSEL utilizing selective area quantum well intermixing (QWI). This is a

solution to tune the emission/absorption wavelength by using a post-growth process to locally alter the bandgap energy of quantum well. [9] Based on which, QWI creates different sections (e.g. gain or passive) on the same wafer, and has been used to realize non-absorbing mirrors in high-power edge-emitters [10], and to locally vary the emission in broad spectral band-width devices [11]. However, this approach never creates an abrupt spatial change in the wavelength of optical transitions as it is driven by atomic diffusion. A transition region (G) between the intermixed section and non-intermixed section is considered. It is assumed that the change in optical transition energy results in a linear variation in the QW absorption, [12-13]. The schematic graph of loss/gain characteristics of the active element indicates that the transition region, G is subject to a graded absorptive loss until enters the passive region, of width W, where light is only subject to internal loss.

The selective area epitaxy [14] is not considered as this technique, whilst reducing the gain at the lasing wavelength at the boundary, realizes a boundary with higher absorptive losses. It would therefore produce parasitic losses higher than the simple unpumped boundary in Fig 6.1 (a).

Figure 6.1 (d) is PCSEL with dual contacts, where the perimeter PCs are covered by another isolated contact (C2), providing the ability to independently control the current to the active element in the boundary PC region. The boundary is considered to be transparent, with no internal loss in the perimeter region. Our simulation does not generate spontaneous emissions in the boundary region. The schematic graph illustrates the loss/gain characteristics of the active element in this case. Multiple contact laser devices typically utilize shallow etching of the contact and waveguide layers [15-16] and have been employed in mode-locked edge emitting lasers [17] and PCSELs [18].

6.3 Simulation Input and Output

Here discusses the other input parameters used in simulation of those proposed device structures to explore routes to maximize the PCE. Table 1 presents input parameters used that are mainly from an InP-based PCSEL from literature [19].

In the absence of the authors providing J_0 and g_0 values, those values obtained experimentally are used.

Lattice constant (a)	480 nm	**κ_{2D+}**	197 cm^{-1}
Wavelength (λ)	1550 nm	**κ_{2D-}**	176 cm^{-1}
Size (S)	Φ200 um	**$\alpha_{\perp}$**	8 cm^{-1}
Vertical reflectivity (R)	0.4	**α_i**	9 cm^{-1}
Interference phase (θ)	0°	**J_0**	380 A cm^{-2}
κ_{1D}	468 cm^{-1}	**g_0**	120 cm^{-1}

Table 6.1: Input parameters for PMC model and data processing.

With reference to edge emitting lasers: [20]

$$\eta_d = \eta_i \frac{\alpha_m}{\alpha_m + \alpha_i} \qquad equation\ 6.3$$

Where η_d is a differential quantum efficiency, α_m is the mirror loss of the laser cavity. For the PCSEL:

$$\eta_d = \eta_i \frac{\frac{1}{2}\left(1 + 2\sqrt{R}\cos\theta + R\right)\alpha_{\perp}}{\left(1 + \sqrt{R}\cos\theta\right)\alpha_{\perp} + \alpha_{//} + \alpha_i} \qquad equation\ 6.4$$

Assuming the case of R = 1 and θ = 0° as:

$$\eta_d = \eta_i \frac{2\alpha_{\perp}}{2\alpha_{\perp} + \alpha_{//} + \alpha_i} \qquad equation\ 6.5$$

Or

$$\eta_d = \eta_i \eta_{\perp} \qquad equation\ 6.6$$

Where

$$\eta_{\perp} = \frac{2\alpha_{\perp}}{2\alpha_{\perp} + \alpha_{//} + \alpha_i} \qquad equation\ 6.7$$

Where $\eta_{\perp}$ is the PCSEL output ratio.

For this case, the gain threshold can be described as:

$$g_{th} = 2\alpha_{\perp} + \alpha_{//} + \alpha_i \qquad equation\ 6.8$$

Another output discussed below is the power conversion efficiency (PCE), defined as the total optical power output by PCSEL divided by the total electrical power input into it. [33] The equations below describe the practical approach of calculation in this paper:

$$PCE = \frac{P_{out}}{P_{in}} = \frac{P_{chosen}}{I_{in}V_{in}} \qquad equation\ 6.9$$

Where the chosen power, P_{chosen} is 1 W; V_{in} is based on typical I-V characteristics from the literature [19]:

$$V = V_0 + IR \qquad equation\ 6.10$$

Where V_0 = 0.82 V and R = 0.18 Ω. I_{in} is based on the calculated η_{SE} by the PMC model:

$$\eta_{SE} = \frac{P_1 - P_2}{I_1 - I_2} \qquad equation\ 6.11$$

Where P_1 is the chosen power 1 W, P_2 is the power at threshold current, which is almost 0 as reported in literature [31], I_1 is the input current I_{in}, I_2 is the threshold current Ith, then:

$$I_{in} = \frac{1}{\eta_{SE}} + I_{th} \qquad equation\ 6.12$$

It is noted that a key requirement for PCE improvement in the PCSEL is the development of technologies that increase the vertical mirror reflectivity R, without impacting the electrical characteristics. Furthermore, all parasitic losses should be minimized, and radiative loss "right-sized" to ensure high η_d and low g_{th}. Our work focusses on device designs that address this later requirement. It is pointed out in the results below the state-of-the-art input parameters at the time of writing. Expected future improvements in vertical mirror technology, increasing R towards 1, will significantly increase the PCE values obtained.

6.4 Absorptive PC Boundary

Figure 6.2 (a) shows a schematic of the absorptive boundary PCSEL. Initially, the size of the contact (yellow dots) is fixed at S = 420 #PC, and the width of boundary region W (dark red dots) varies from 50 to 450 #PC. Lasing occurs in the contacted region, S, and self-absorption (κ_{ab}) is considered for the unpumped boundary of width W. The absorption coefficient is dictated by the MQW design and detuning between active element peak gain and the PCSEL lasing wavelength. In this work it is estimated that κ_{ab} = 100 cm^{-1}. [3]

Figure 6.2 (b) plots the calculated in-plane loss (black dots) and internal loss (red dots) as a function of W. As expected, the in-plane loss, $\alpha_{//}$, reduces to zero as W is increased, but due to self-absorption, the internal loss α_i increases. This interdependence has been previously reported [8]. The in-plane loss reduces to essentially zero (< 0.1 cm^{-1}) for W > 350 #PC, this improvement comes with an increase of α_i from 9 to ~31 cm^{-1}.

Having determined the losses, the total parasitic losses and output ratio are discussed below. Figure 6.2 (c) plots the total parasitic loss ($\alpha_{parasitic} = \alpha_{//}+\alpha_i$) and calculated output ratio ($\eta_\perp$) as

a function of W for the absorptive boundary PCSEL. Total parasitic loss reduces from 87 cm^{-1} (W = 0), asymptotically reaching a value of 31 cm^{-1} at W > 350 #PC. This leads to $\eta_{\perp}$ increasing from 0.08 (W = 0) to 0.2 (W > 350 #PC).

So, for the absorptive boundary PCSEL with input parameters mentioned above, W = 350 #PC is needed to minimize the parasitic loss (or zero the in-plane loss). Then for case W = 350 #PC, the effect of size, S is explored. Figure 6.2 (d) plots the total parasitic loss, $\alpha_{parasitic}$ and calculated output ratio, $\eta_{\perp}$ as a function of S for the absorptive boundary PCSEL. $\alpha_{parasitic}$ reduces from 79 (S = 100 #PC) to 17 cm^{-1} (S = 1000 #PC). And this reduction leads to $\eta_{\perp}$ increasing from 0.09 to 0.31.

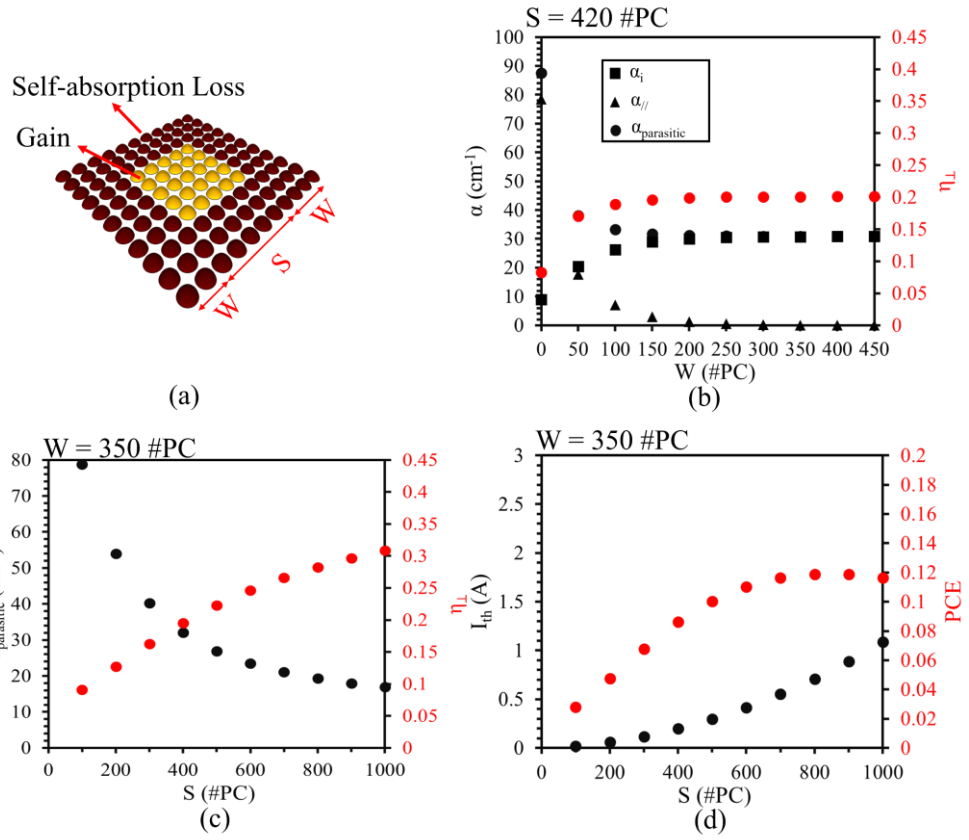

Figure 6.2: (a) Schematic of absorptive boundary. Loss and output ratio as a function of (b) W and (c) S. (d) Threshold current and power conversion efficiency as a function of S.

Then the effect of S on threshold current, I_{th} and power conversion efficiency, PCE is explored. Figure 6.2 (d) plots I_{th} and PCE as a function of S. I_{th} increases from ~0.02 to 1.09 A. While PCE increases from 0.03 (S = 100 #PC) and reaches a maximum value of 0.12 at S = ~850 #PC.

This result highlights that this approach to improving PCE is effective, but the efficacy is

limited due to the high internal loss of the absorptive boundary region. For ease of comparison, the results presented in this section are denoted by solid lines in the following figures (Figures 6.2 – 6.5). Reducing the QW number to reduce absorption requires the reduction in total device loss to be a valid approach [3, 24]. Detuning the gain peak is an additional route to reducing self-absorption [25], but this again comes with a reduction in operating characteristics and increased temperature sensitivity.

6.5 Butt-coupled Active/passive PCSEL

Figure 6.3 (a) plots the schematic of the PCSEL with a butt-coupled passive PC containing boundary region. A scattering interface (dark red line) separates the passive region from gain region (this is positioned at the boundary between PC atoms in the model and has no physical size).

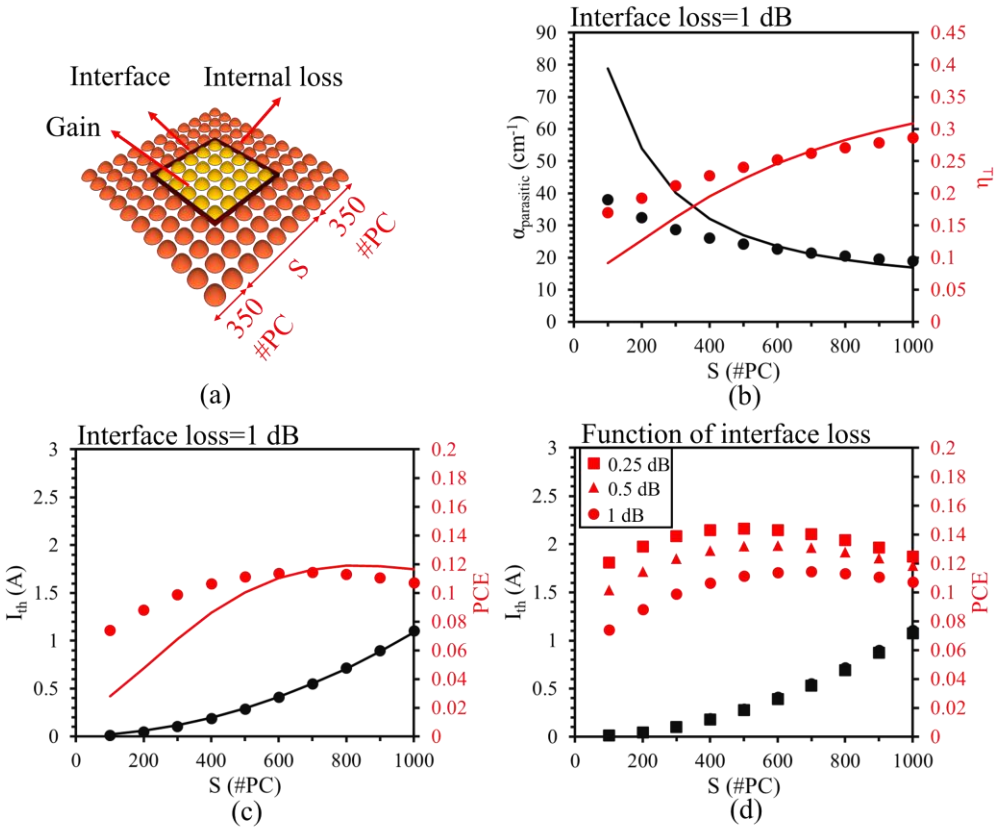

Figure 6.3: (a) Schematic of butt-coupled PCSEL. (b) Parasitic loss and output ratio as a function of S. Threshold current and power conversion efficiency as a function of (c) S and (d) interface loss.

It is initially used a value for this scattering loss of 1dB, experimentally determined for monolithically integrated edge-emitting lasers [21]. Figure 6.3 (b) plots the total parasitic loss, $\alpha_{parasitic}$, and $\eta_\perp$ as a function of S. $\alpha_{parasitic}$ decreases from 38 to 19 cm^{-1}, with a concomitant

increase of $\eta_{\perp}$, raising from 0.17 to 0.29. It is noted that total parasitic loss is very similar to those of the unpumped boundary.

Figure 6.3 (c) plots the PCSEL threshold current, I_{th} and power conversion efficiency, PCE as a function of S. I_{th} increases from ~0.01 to 1.11 A. PCE reaches maximum at S = 700 #PC with value of 0.11. Again, higher PCE appears when S < 700 #PC. Whilst optimal contact size is different as compared to the unpumped boundary PCSEL, the values of the threshold currents and PCE are very similar.

To further explore the effect of this interface loss on I_{th} and PCE, the effect of reducing coupling loss is simulated. Figure 6.3 (d) plots I_{th} and PCE as a function of S with interface loss of, 0.25 dB (square dots), 0.5 dB (triangular dots) and 1 dB (circular dots). It can be seen that the I_{th} does not show significant change. As expected, the PCE increases when interface loss is reduced. For the case interface loss = 0.25 dB, PCE reaches a maximum of 0.14 at S = 500 #PC; the case interface loss = 0.5 dB, PCE reaches a maximum of 0.13 at S = 600 #PC.

Whilst for this device the increase in PCE is not significant (other engineering choices are discussed later), by comparison to the unpumped boundary, the Butt-Coupled PCSEL allows a smaller, comparable efficiency PCSEL to be realized.

6.6 Selective Area Intermixed Active/passive PCSEL

Figure 6.4 (a) plots a schematic of intermixed PCSEL. The gain region (yellow dots) has varied sizes, S. The intermixing technique creates a transition region, within which the wavelength shifts. In the PMC model, this transition region is assumed to have an absorption loss with linear reducing value from contact to passive boundary W. See Fig 1(d). The width of this transition region, G, is initially assumed to have a value of 50 #PC (~20 um for InP based devices) [17] W and G have a total width of 350 #PC as in previous discussions.

Figure 6.4 (b) plots the $\alpha_{parasitic}$ and $\eta_{\perp}$ as a function of S, for the case G = 50 #PC, $\alpha_{parasitic}$ shows a reduction from 33 to 15 cm^{-1}, with an increase of $\eta_{\perp}$ from 0.12 to 0.26. Figure 6.4 (c) plots the I_{th} and PCE as a function of S. For G = 50 #PC, I_{th} shows a similar increase as butt-coupled PCSEL from ~0.02 to1.1 A. PCE reaches a maximum with value of 0.14 at S = 600 #PC.

By contrast to the intermixing of full laser structures [22-23], the thickness of semiconductor material between the surface and the MQW can be small in PCSELs, leading to the possibility for smaller transition regions. The effect of reducing the width of this transition is explored, choosing transition thicknesses of 5 and 25 #PC, corresponding to ~2 and 10 um. Figure 6.4

(d) plots the I_{th} and PCE as a function of S, with varied G (5, 25 and 50 #PC). I_{th} does not exhibit significant change.

For the case where G = 50 #PC, PCE has a maximum value of 0.16 at S = 600 #PC; the case G = 25 #PC, PCE has a maximum value of 0.18 at S = 500 #PC. The effect of reducing the transition thickness is to enhance the PCE and to allow the move to smaller PCSELs.

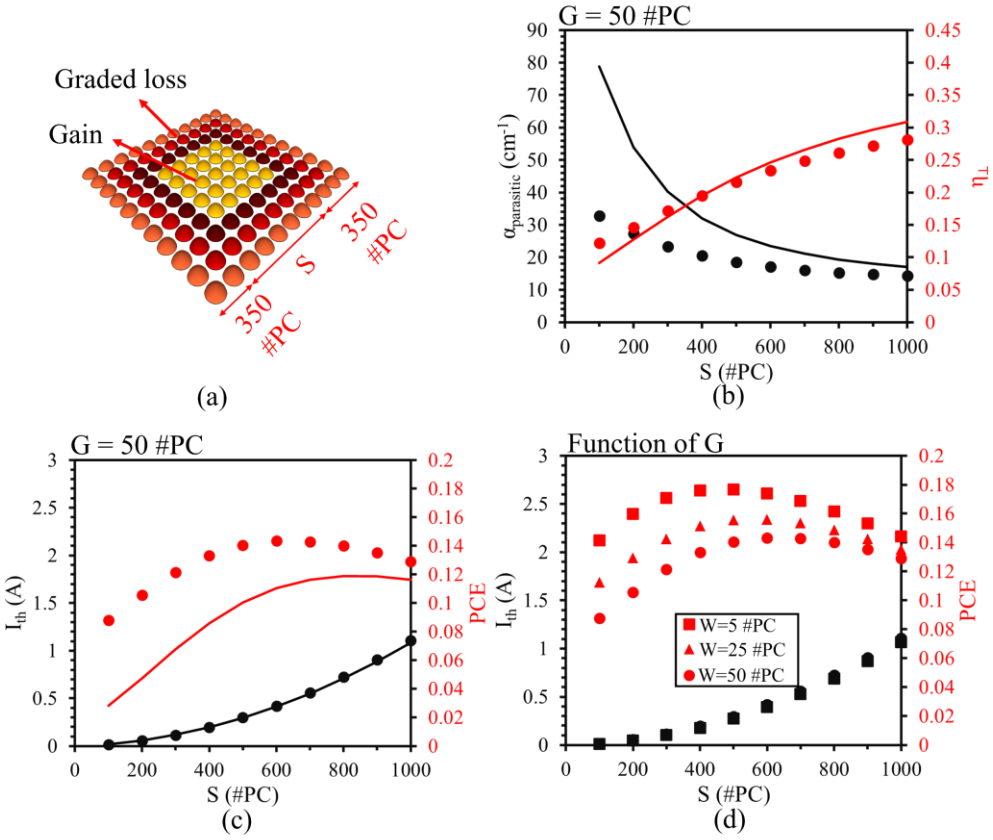

Figure 6.4: (a) Schematic of intermixed PCSEL (b) Parasitic loss and output ratio as a function of S. Threshold current and power conversion efficiency as a function of (c) S and (d) G.

6.7 Dual Contact PCSEL

Using the characteristic boundary width W=350 #PC from above, the effect of adding a second independent contact to the boundary layer is explored below. Figure 6.5 (a) shows a schematic of the dual contact PCSEL; contact 1 (C1, yellow dots) has size S, and contact 2 (C2 grey dots) has fixed width W = 350 #PC. It is considered that a current being applied to C2 to make the active element in the boundary PC region transparent (κ_{ab} and α_i).

The input current to the device is updated to:

$$I_{in} = I_{C1} + I_{C2} \qquad equation\ 6.13$$

Where I_{C1} is given by equation (12), where the threshold gain (equation 8) allows threshold current to be determined from the assumed values of J_0 and g_0. The slope efficiency uses the parameters in table 1 and the calculated parasitic losses to determine $\eta_\perp$. The transparent current (I_{C2}) is calculated from J_0 and the size of C2:

$$I_{C2} = J_0 * S_{C2} \qquad equation\ 6.14$$

Figure 6.5 (b) plots the total parasitic loss, $\alpha_{parasitic}$, and $\eta_\perp$ as a function of S. The parasitic loss shows a gradual reduction as the size of contact 1 is increased, reducing from 13 to 11 cm^{-1}. The output ratio shows an increase with increasing contact 1 size, rising from 0.36 to 0.43. In the case of an infinitely thick boundary PC layer, it is reasonable to expect these figures to remain constant. Their small variation is attributed to their finite size.

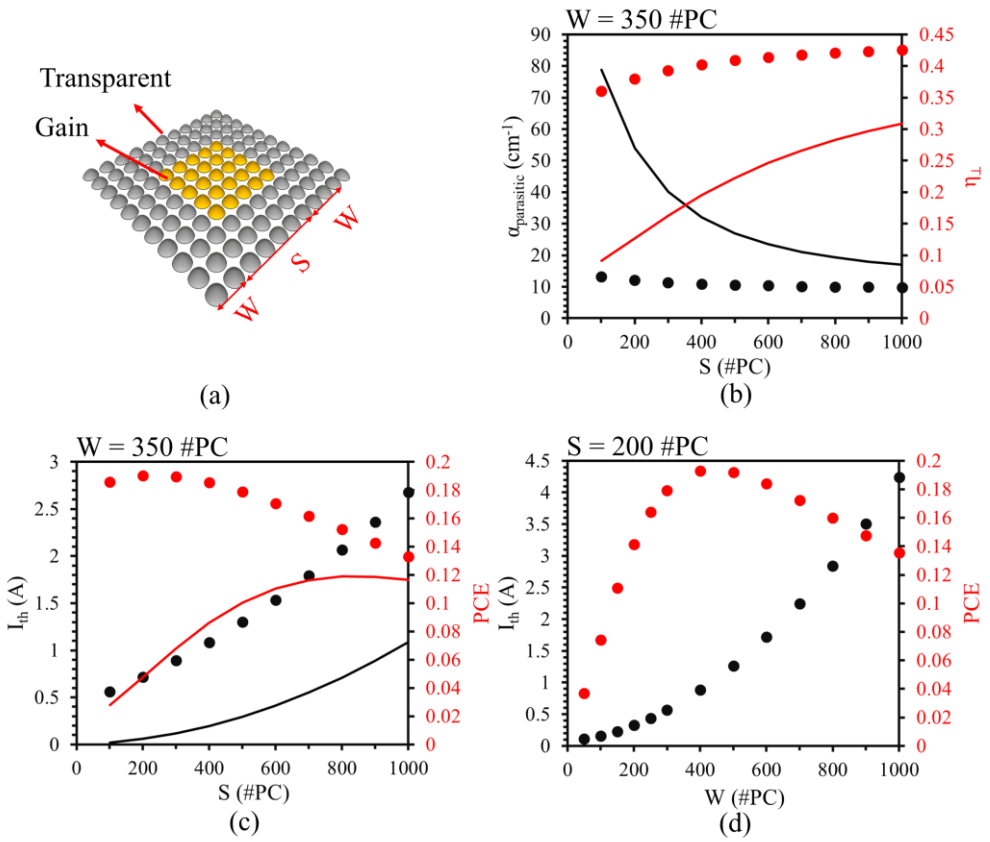

Figure 6.5: (a) Schematic of dual contact. (b) Parasitic loss and output ratio as a function of S. Threshold current and power conversion efficiency as a function of (c) S and (d) W.

Figure 6.5 (c) plots the PCSEL threshold current, I_{th} and power conversion efficiency, PCE as a function of contact 1 size. I_{th} shows an increase from 0.6 to 2.7 A as S increases from 100 to 1000 #PC. This increase in threshold current is mainly a function of the area scaling (of both C1 and C2) as losses remain almost constant. The PCE shows a significant increase compared

to the absorptive boundary case (Fig. 6.2(d)). This is notwithstanding the additional current required to make the boundary transparent. The PCE has a maximum value of ~0.19 (0.190) at S = 200 #PC.

I then continue to explore the effect of the contact 2 size to I_{th} and PCE for the case with highest PCE, S = 200 #PC. Figure 6.5 (d) plots the I_{th} and PCE as a function of the width of contact 2, W. I_{th} shows an increase from 0.1 to 4.2 A. PCE has a maximum value of ~0.19 (0.193).

6.8 Discussion

For PCSELs in general, improvement in vertical mirror technologies, reduction of parasitic losses, and right-sizing radiative loss are required. The current approach to PCE enhancement by using an absorptive boundary leads to an effective zeroing of in-plane loss, but an enhancement in internal loss. To engineer such devices, reducing the number of QWs in the active will result in lower absorption and hence higher PCE. However, this can only be achieved by reducing all losses (radiative and parasitic) to reduce threshold gain. There is also design room for detuning, but this impacts threshold current.

In order to engineer butt-coupled PCSELs, the interface scattering and internal loss of the PC boundary layer (not discussed here) need reducing. A drive to smaller PCSELs breaks the need for PC shapes that have lower coupling to enable spatial spectral mode control for large areas [6]. The increase of the PC scattering strength will in turn reduce parasitic at the butt-joint, in turn driving up PCE.

The intermixing approach shows promise. The use of intermixing very close to the MQW active, followed by PC definition and epitaxial re-growth may provide a route to higher PCE without the need for additional drive electronics. The minimization of the graded transition region thickness is therefore an interesting route to pursue. The relative technological ease of realizing a low scattering butt-joint, or thin intermixed transition region may decide the best approach. However, the butt-joint does offer the opportunity to create undoped passive waveguides, adding a possible advantage of reduced internal loss in the passive element.

The dual contact approach benefits over all other approaches by zeroing parasitic loss in the boundary. However, this occurs at a price: the additional current supplied to the boundary (and associated heat, and energy required to remove that heat). This would again be reduced in the case of fewer QWs, reducing the C2 current as transparency current density is lower. Again, a push to lower PCSEL size allows higher coupling strength PCs, further reducing the in-plane loss, reducing the required PC boundary size, and additional current.

6.9 Summary

A range of device designs to minimize parasitic loss in PCSELs have been explored using the Probabilistic Markov chain (PMC) model. It is described that the inputs and outputs to the simulation and described the effects of butt-coupled passive sections in the boundary PC region, selective area intermixing the active element in the boundary PC region, and using a second contact to the boundary PC. The additional contact device renders the boundary transparent, whilst the other two approaches maintain an internal loss only.

Various characteristics of these techniques were explored and the PCE for an exemplary 1 W source were discussed. For the butt-coupled device it is considered that improvement in the fabrication technologies leading to reduced scattering loss at the etched/regrown waveguide interface. For the selective area intermixed device, a reduction in the lateral extent of the transition from active to passive wavelengths is also considered. In the case of the dual contact device, the highest PCE was shown to be possible, given the input parameters taken from the literature. A critical comparison of the approaches was made, and possible future research avenues discussed.

6.10 Future Work

In general, for this type of device, R is the key factor to improve the PCE. The realization of R =~ 1 may be reached by applying the vertical 1D DBR or perfect metallization of backside contact.

There is some realistic difficulty in realizing mentioned designs in this chapter. Compared to other class of semiconductor lasers, PCSEL is relatively complex in fabrication already. Butt-coupled or intermixed technologies will enhance device operation, however, more complex process on the core (active region, e.g. quantum well) is required, which leads to the real enhancement is also limited. As a result, the cost and payback of realize these to designs may not easily be balanced.

As for dual contact, adding a 2^{nd} contact is much easier in fabrication, in other words, more realizable. To validate the theory obtained in this chapter, input parameters need to be determined by analysing existing PCSEL devices with conventional design. With such inputs, use the PMC model to predict the enhancement provided by dual contact design. It should be noted that, the current spreading needs to be separately simulated cause the material properties are not considered in the PMC model. With simulations above, the dual contact PCSEL device

can be designed and fabricated. For comparison consideration, PCSELs without the 2nd contact should also be fabricated and characterized.

Dual contact PCSEL theoretically reduces the total loss, which may allow the number of QWs to be reduced in combination with great value coupling coefficients PC, as a result, very small device could be possibly realized.

Another possible application of multiple contact on PCSEL device might be shaping the current density distribution, which will be important for mode control of PCSEL.

References

[1]. K. Hirose, Y. Liang, Y. Kurosaka et al., "Watt-class high-power, high-beam-quality photonic-crystal lasers," Nature Photon., vol. 8, pp. 406–411, 2014, doi: 10.1038/nphoton.2014.75.

[2]. K. Emoto, T. Koizumi, M. Hirose et al., "Wide-bandgap GaN-based watt-class photonic-crystal lasers," Commun. Mater., vol. 3, p. 72, 2022.

[3]. M. Yoshida, M. De Zoysa, K. Ishizaki et al., "Double-lattice photonic-crystal resonators enabling high-brightness semiconductor lasers with symmetric narrow-divergence beams," Nature Mater., vol. 18, pp. 121–128, 2019, doi: 10.1038/s41563-018-0242-y.

[4]. M. Yoshida, M. De Zoysa, K. Ishizaki et al., "Double-lattice photonic-crystal resonators enabling high-brightness semiconductor lasers with symmetric narrow-divergence beams," J. Phys. Photonics, vol. 3, no. 2, 2021, Art. no. 022006, doi: 10.1088/2515-7647/abea06.

[5]. M. Nishimoto, K. Ishizaki, K. Maekawa, K. Kitamura and S. Noda, "Photonic-crystal surface-emitting laser," Appl. Phys. Express, vol. 6, no. 4, 2013, Art. no. 042002, doi: 10.7567/APEX.6.042002.

[6]. Y. Kurosaka, S. Iwahashi, Y. Liang et al., "On-chip beam-steering photonic-crystal lasers," Nature Photon., vol. 4, pp. 447–450, 2010, doi: 10.1038/nphoton.2010.118.

[7]. H. Matsubara, S. Yoshimoto, H. Saito et al., "GaN photonic-crystal surface-emitting laser at blue-violet wavelengths," Science, vol. 319, no. 5862, pp. 445–447, 2008.

[8]. J. Liu, X. Zhao, Z. Bian *et al.,* "Interdependence of parasitic losses in photonic crystal surface emitting lasers," *AIP Advances*, vol. 15, no. 4, 2025, Art. no. 045321, doi: 10.1063/5.0252646.

[9]. J. H. Marsh, "Quantum well intermixing for optoelectronics," *Semicond. Sci. Technol*., vol. 8, no. 6, p. 1136, 1993.

[10]. L. Hou, R. Dylewicz, M. Haji, P. Stolarz, B. Qiu and A. C. Bryce, "Monolithic 40-GHz Passively Mode-Locked AlGaInAs–InP 1.55-μ m MQW Laser With Surface-Etched Distributed Bragg Reflector," *IEEE Photon. Technol. Lett.*, vol. 22, no. 20, pp. 1503-1505, Oct.15, 2010, doi: 10.1109/LPT.2010.2064764.

[11]. K. J. Zhou et al., "Quantum dot selective area intermixing for broadband light sources," *Optics*

Express, vol. 20, no. 24, pp. 26950-26957, Nov. 2012. doi: 10.1364/OE.20.026950.

[12]. T. Tabbakh, "Diffusion and Quantum Well Intermixing," in *Recent Advances in Nanophotonics - Fundamentals and Applications, IntechOpen*, 2020. doi: 10.5772/intechopen.92440.

[13]. S. Helmy, A. C. Bryce, D. C. Hutchings, J. S. Aitchison, and J. H. Marsh, "Band gap gratings using quantum well intermixing for quasi-phase-matching," *J. Appl. Phys*., vol. 100, no. 12, 2006, Art. no. 123107, doi: 10.1063/1.2402034.

[14]. X. Zhao, A. F. McKenzie, C. W. Munro *et al.,* "Large-area 2D selective area growth for photonic crystal surface emitting lasers," *J. Cryst. Growth*, vol. 603, 2023, Art. no. 127036, doi: 10.1016/j.jcrysgro.2022.127036.

[15]. L. A. Coldren, G. A. Fish, Y. Akulova *et al.,* "Tunable semiconductor lasers: a tutorial," *J. Lightw. Technol.*, vol. 22, no. 1, pp. 193-202, Jan. 2004, doi: 10.1109/JLT.2003.822207.

[16]. M. A. Tran, D. Huang, and J. E. Bowers, "Tutorial on narrow linewidth tunable semiconductor lasers using Si/III-V heterogeneous integration," *APL Photonics*, vol. 4, no. 11, 2019, Art. no. 111101, doi: 10.1063/1.5124254.

[17]. H. A. Haus, "Mode-locking of lasers," *IEEE J. Sel. Topics Quantum Electron*., vol. 6, no. 6, pp. 1173-1185, Nov.-Dec. 2000, doi: 10.1109/2944.902165.

[18]. R. Taylor, D. Childs, P. Ivanov *et al.,* "Electronic control of coherence in a two-dimensional array of photonic crystal surface emitting lasers," *Sci. Rep*., vol. 5, 2015, Art. no. 13203, doi: 10.1038/srep13203.

[19]. T. Aoki, Y. Itoh, K. Fujii *et al.,* "High-power high-beam-quality 1550-nm-wavelength InP-based photonic-crystal surface-emitting laser," in *Proc. SPIE Novel In-Plane Semiconductor Lasers XXIV*, vol. PC13385, 2025, Art. no. PC133850Y, doi: 10.1117/12.3037797.

[20]. L. A. Coldren, S. W. Corzine, and M. L. Mašanović, "Mirrors and Resonators for Diode Lasers," in *Diode Lasers and Photonic Integrated Circuits*, 2nd ed. Hoboken, NJ, USA: Wiley, 2012, ch. 3, pp. 91–155.

[21]. Y. Cheng, J. Pan, S. Liang, W. Feng, Z. Liao, F. Zhou, B. Wang, L. Zhao, H. Zhu, and W. Wang, "Butt-coupled MOVPE growth for high-performance electro-absorption modulator integrated with a DFB laser," *J. Crystal Growth*, vol. 308, no. 2, pp. 297–301, 2007, doi: 10.1016/j.jcrysgro.2007.09.004.

[22]. L. Hou, M. Haji, J. Akbar, J. H. Marsh, and A. C. Bryce, "AlGaInAs/InP monolithically integrated DFB laser array," *IEEE J. Quantum Electron.*, vol. 48, no. 2, pp. 137–143, Feb. 2012, doi: 10.1109/JQE.2011.2174455.

[23]. J. H. Marsh, "Quantum well intermixing revolutionizes high power laser diodes," *Laser Technik J.*, vol. 4, no. 6, pp. 32–35, 2007, doi: 10.1002/latj.200790190.

[24]. P. M. Ilroy, A. Kurobe, and Y. Uematsu, "Analysis and application of theoretical gain curves to the design of multi-quantum-well lasers," *IEEE J. Quantum Electron.*, vol. 21, no. 12, pp. 1958–1963, Dec. 1985, doi: 10.1109/JQE.1985.1072606.

[25]. Ramdane, F. Devaux, N. Souli, D. Delprat and A. Ougazzaden, "Monolithic integration of multiple-quantum-well lasers and modulators for high-speed transmission," in *IEEE Journal of Selected Topics in Quantum Electronics*, vol. 2, no. 2, pp. 326-335, June 1996, doi: 10.1109/2944.577388.

Chapter 7: Conclusion

This thesis has been dedicated to the development, validation, and application of a probabilistic Markov chain (PMC) model for the analysis and design of photonic crystal surface emitting lasers (PCSELs). The work commenced from the recognition that a gap existed in the PCSEL design cycle: the need for a computationally efficient and flexible tool that could directly link microscopic scattering parameters to macroscopic device-level performance, particularly the critically important in-plane loss ($\alpha_{//}$). The research presented bridges this gap, leading to both fundamental insights and practical design guidelines for advancing PCSEL technology.

Chapter 3 established the PMC model as a robust and reliable simulation framework. By conceptualizing light propagation as a Markov process between discrete directional states, the model efficiently calculates the flow and loss of optical power in a finite PC lattice. The convergence criteria were discussed, providing and results were subsequently validated with excellent agreement against experimental data from both conventional PCSELs and the more complex Resonator Embedded PCSELs (REPCSELs). This validation confirmed the PMC model's capability to accurately predict key device metrics such as threshold gain and slope efficiency.

The model was then used to explore PCSEL design in **Chapter 4**. The parameter studies revealed that while increasing the in-plane coupling coefficients (κ_{1D}, κ_{2D}) can reduce $\alpha_{//}$, the effect plateaus, and impractically large values would be required to minimize this loss. This finding suggests that solely pursuing complex PC patterns for higher coupling may be a futile strategy for high-efficiency devices. More promisingly, the model quantitatively demonstrated the impact of in-plane mirrors, showing that they can reduce $\alpha_{//}$ to negligible levels and enable control over the lasing mode, a capability exploited in the design of REPCSELs.

In **Chapter 5** the PMC model was applied to the use of an unpumped PC boundary. The analysis uncovered a fundamental interdependence between in-plane loss ($\alpha_{//}$) and internal loss (α_i), mediated by self-absorption in the unpumped quantum wells. This redefines the optimization problem: minimizing $\alpha_{//}$ by widening the boundary inevitably increases α_i. The introduction of the "total parasitic loss" ($\alpha_{//} + \alpha_i$) as a key figure of merit provides a more holistic and accurate metric for device design, revealing that blindly extending the pumped or unpumped region is an ineffective and often counterproductive strategy.

Building on this understanding, **Chapter 6** utilised the PMC model as a predictive design tool by proposing and evaluating three novel PCSEL architectures aimed at breaking the parasitic

loss interdependence. The comparative analysis of the butt-coupled, selective area intermixed, and dual-contact designs provided a critical roadmap for future development. While each approach showed promise, the dual-contact scheme was identified as theoretically capable of achieving the highest power conversion efficiency (PCE) by effectively rendering the boundary transparent, albeit at the cost of increased complexity and drive current. The intermixing approach also emerged as a highly promising route, especially if the transition region can be minimized. These proposals offer pathways towards PCSELs with significantly enhanced performance, moving beyond the limitations of current designs.

In conclusion, this research has made the following contributions to the field of PCSELs:

- The successful development and experimental validation of a novel, efficient, and flexible Probabilistic Markov Chain simulation model.
- Fundamental new insights into PCSEL physics, particularly the interdependence of in-plane and internal loss in devices with unpumped boundaries.
- The conceptualization and theoretical evaluation of innovative, high-efficiency PCSEL designs that leverage advanced photonic integration techniques.

The PMC model can accelerate the design and optimization of PCSELs. The insights gained and the future directions outlined pave the way for the next generation of devices. Future work will focus on the experimental realization of the proposed dual-contact and intermixed devices, further code development will include dynamic and gain effects, and the extension of the model to other PC lattices.

Chapter 8: Future Work

The PMC model successfully bridges microscopic coupling coefficients and macroscopic device-level losses, enabling the exploration of novel device configurations with low computational cost. Its development and validation in this thesis have established a robust and flexible framework for analysing and designing PCSELs. This work has revealed several promising avenues for further development, both of the model itself and its applications. This chapter outlines a plan for future research, structured into five key directions.

8.1 Towards a Next-Generation PMC Simulation Platform

The future evolution of the PMC model can be envisioned as a three-stage roadmap, progressing from immediate usability improvements to a fundamental transformation of its core capabilities.

Development of a graphical user Interface (GUI): To transform the PMC model from a code-based tool into a versatile platform, the development of an intuitive GUI is required. This interface would enable the visual definition of device geometries (e.g., contact size, PC region, mirror placement), streamline parameter input, and automate the visualization of results, significantly lowering the barrier to entry for non-specialists.

Extension to Triangular Lattice Structures: A critical extension of the model's versatility is its adaptation for triangular lattice PCSELs. This primarily requires recoding the propagation directions for each PC atom from a four-fold set (north, south, east, west) to a six-fold set (0°, 60°, 120°, 180°, 240°, 300°), thereby expanding its domain of application.

Integration of a Gain/Loss Calculator and Toolchain Coupling: To create a more self-contained environment, an internal gain/loss calculator should be integrated, moving beyond the current manual input method. Furthermore, a deeper integration with fundamental electromagnetic simulators (e.g., FDTD, PWE) should be pursued. This would enable the automatic extraction of coupling coefficients from physical PC designs, creating a seamless pipeline from nanophotonic structure to device-level performance prediction.

Development of a Dynamic PMC Model: A future dynamic model would replace static power generation with time-dependent variables for carrier density, gain, and photon generation. Operating with small time steps (~10^{-13} s) and incorporating wavelength dependence, this model would unlock the study of dynamic phenomena such as modulation response, transient behaviour, and nonlinear dynamics, positioning the PMC framework as a uniquely powerful

tool for exploring complex laser physics.

8.2 Exploration and Validation of Novel PCSEL Designs

The insights gained from this thesis, particularly through the application of the current PMC model, directly inform several promising device designs that require further investigation.

PCSELs with Selectable Boundary Mirrors: Based on the findings in Chapter 4, a logical next step is to design a PCSEL with independently controllable perimeter mirrors. This could enable dynamic modification of the beam shape and central position, introducing elements of beam steering.

Empirical Validation of the Dual-Contact Design: The dual-contact PCSEL concept proposed in Chapter 6 offers a theoretically compelling path to higher Power Conversion Efficiency (PCE). Future work must focus on its empirical validation: using the PMC model to predict performance, guiding the device design with current-spreading simulations, and fabricating devices for direct comparison with conventional single-contact PCSELs.

Mode Control via Multi-Element Contacts: Exploring multiple, independently biased contacts could enable precise control over the current density distribution, opening new avenues for advanced mode control and stable single-mode operation.

8.3 Industrial Considerations and Pareto Optimization

Finally, moving from laboratory prototypes to commercially viable devices necessitate a focus on practical trade-offs.

Balancing Performance with Fabrication Complexity: Future research should systematically evaluate the cost-benefit ratio of advanced designs. The primary indicator should be the Power Conversion Efficiency (PCE), and efforts must be directed towards solutions that offer significant performance improvements without a prohibitive increase in process complexity or cost.

8.4 Summary

In conclusion, the PMC model serves not only as a tool for analysing existing PCSELs but also as a springboard for future innovation. The planned, staged enhancement of the model, combined with the exploration of novel device architectures, paves the way for the next generation of high-performance, efficiently manufactured PCSELs.

Appendix Material A: Example of transition from Coupling Coefficient to Optical Scattering Probability

In this thesis, the relationship between device-level optical loss and microscopic coupling coefficients is established by converting these coefficients into probabilities of optical power scattering among photonic crystals (PCs). This appendix provides the definitions of the coupling coefficients and an illustrative example of how to calculate the corresponding probability.

The coupling coefficients quantify the strength of coupling between waves propagating in a square-lattice distributed feedback (DFB) structure (PC) [Sakai 2006]. Conceptually, their definition can be likened to absorption coefficients, which describe the rate at which the intensity of electromagnetic radiation diminishes as it travels through a medium. These coefficients, typically denoted by α and expressed in units of inverse length (e.g., cm^{-1}), are used here in a similar form.

Below is an example demonstrating the conversion from a coupling coefficient in cm^{-1} to a probability of scattering.

Assuming in a PC grating with period of 0.48 um, a 1D coupling coefficient, α has a value of 1000 cm^{-1}:

$$\alpha = 1000\ cm^{-1} \qquad equation\ App.A.1$$

This macroscopically, represents a reduction of optical intensity from 1 to 1/e, microscopically, a reduction of the quantity of photons drops to 1/e. According to the definition here, a percentage, P is used to represent this reduction:

$$P = 1 - \frac{1}{e} \sim = 0.632 \qquad equation\ App.A.2$$

Which means, in this case, the optical power reduces by ~63% in 1000 cm. I then introduce the period of PC to the calculation. Then the number of reduction periods, N is:

$$N = \frac{\frac{1}{1000\ cm^{-1}} \times 10^4}{0.48\ um} \sim = 20.8 \qquad equation\ App.A.3$$

Which means the reduction described above happening in 20.8 period. Then apply the percentage to the number of periods, the reduction probability of each period of the corresponding coupling coefficient, P_α is described as:

$$P_\alpha = \frac{P}{N} \sim = 3\% \qquad equation\ App.A.4$$

In conclusion, the probability of 1D coupling is ~3% per period. And it is ready for the PMC model to use its statistic method for loss calculations.

References

[1]. T. Sakai and S. Noda, "Coupled-wave theory for photonic crystal waveguides," Opt. Express, vol. 14, no. 20, pp. 9460-9466, 2006.

[2]. T. Sakai, E. Miyai, and S. Noda, "Coupled-wave model for square-lattice photonic crystal lasers with transverse-electric polarization," IEEE J. Quantum Electron., vol. 43, no. 11, pp. 1179-1186, 2007.

Appendix Material B: C Code of Probabilistic Markov Chain Model

This Appendix describes the structure of the C code implementation for the probabilistic Markov chain model. The program is organized into several header files, each serving a distinct purpose:

Main Program: Controls the overall flow and includes all necessary header files. This is the primary file that users may modify according to their needs.

Markov Chain Header: Contains the core algorithm discussed in this thesis. While only one function is provided here, this file is intended as the primary location for users to add their own custom functions.

Basic Functions Header: Includes all supporting functions except the Markov chain implementation. As this file provides fundamental infrastructure, modifications are not recommended.

Constants Header: Defines all constants used throughout the program.

A simplified version of this code has been made available on GitHub:

https://github.com/Jingzhao-Liu/Probabilistic-Markov-Chains-Modelling-Quarter

Main Program

```
/*this script is for difference in one device, using left bot quarter of device in sim
will support function:
1: charge and uncharge area (W) with extra quantum well absorption
2: size of PC and contact defined as
//1: square PC & circle contact;
//2: square PC & square contact;
//3: circle PC & circle contact;
//4: square PC & square contact with a absorptive interface
//5: square PC & square contact with a grating absorption area
*/
#include "constants.h"
#include "basic functions.h"
#include "Markov chain.h"

int main()
{
	/// <set parameters>
	Period = 0.48;//unit:um
	MK1D = 1; //multiple of K1D
	MK2D = 1;//multiple of K2D
	char str[] = { "Change me.csv" };//Define file name
	K1D = 468; //unit:cm-1
```

```
K2D_p = 186.5;
K2D_m = 186.5;
Krad = 8;
Ki = 3;
extra_internal = 0;
refl = 0.0;//0-1
timestep = 20000;
int W[] = {400};
int contact[] = { 100,200,300,400,500,600,700,800,900,1000 };
int function_choice =2;
//1: square PC & circle contact;
//2: square PC & square contact;
//3: circle PC & circle contact;
//4: square PC & square contact with a absorptive interface
/// <returns></returns>


K1D = K1D * MK1D;
K2D_p = K2D_p * MK2D;
K2D_m = K2D_m * MK2D;
Initialize();
fout.open(str);
fout << "size_c,size_w,power_v,power_i,power_p,injection,loss_p,loss_i\n";
int number_i = sizeof(contact) / sizeof(contact[0]);
int number_j = sizeof(W) / sizeof(W[0]);
typedef void (*FuncPtr)(int, int, int);
FuncPtr selected_function;
switch (function_choice)
{
	case 1:
	{
		selected_function = Q_S_C;
		break;
	}
	case 2:
	{
		selected_function = Q_S_S;
		break;
	}
	case 3:
	{
		selected_function = Q_C_C;
		break;
	}
	case 4:
	{
		selected_function = Q_S_S_with_interface;
		break;
	}
	case 5:
	{
		selected_function = Q_S_S_with_grating;
		break;
	}
	default:
	{
		cout << "Invalid choice!" << endl;
		return -1;
	}
}
for (int i = 0; i < number_i; i++)
{
```

```
		for (int j = 0; j < number_j; j++)
		{
			selected_function(contact[i], timestep, W[j]);//(fixed
area,timestep,unpumped W )
			cout << "contact = " << contact[i] << ", W = " << W[j] << ",
complete" << endl;
		}
	}
	fout.close();
	return 0;
}
```

Basic Functions Header

```
#ifndef BASIC FUNCTIONS_H
#define BASIC FUNCTIONS_H
#include "constants.h"

/* these 2 funchtions convert Kappas into probability(K to P) */
double Transfer(double K)
{
	return (1 / K) * pow(10, 4);
}
double Calculate_Percent(double K)
{
	double Total_Period = K / Period;
	return P / Total_Period;
}
/* these functions are optical power calculation in each direcation */
double Calculate_Energy_N(double N_in, double S_in, double W_in, double E_in)
{
	return S_in * Pforward + W_in * P2D_m + E_in * P2D_p + N_in * P1D;
}
double Calculate_Energy_S(double N_in, double S_in, double W_in, double E_in)
{
	return N_in * Pforward + W_in * P2D_p + E_in * P2D_m + S_in * P1D;
}
double Calculate_Energy_W(double N_in, double S_in, double W_in, double E_in)
{
	return E_in * Pforward + N_in * P2D_m + S_in * P2D_p + W_in * P1D;
}
double Calculate_Energy_E(double N_in, double S_in, double W_in, double E_in)
{
	return W_in * Pforward + N_in * P2D_p + S_in * P2D_m + E_in * P1D;
}
double Calculate_Energy_Vertical(double N_in, double S_in, double W_in, double E_in)
{
	return (N_in + S_in + W_in + E_in) * Prad;
}
double Calculate_Energy_Internal(double N_in, double S_in, double W_in, double E_in)
{
	return Internal_out = (N_in + S_in + W_in + E_in) * Pi;
}
double remove_internal_loss(double input)
{
	return input * (1 - Pi);
}
double remove_internal_lossex(double input)
{
	return input * (1 - Pi2);
}
```

```
/* these functions are for different internal loss in one device */
double Calculate_Energy_N2(double N_in, double S_in, double W_in, double E_in)
{
	return S_in * Pforward2 + W_in * P2D_m + E_in * P2D_p + N_in * P1D;
}
double Calculate_Energy_S2(double N_in, double S_in, double W_in, double E_in)
{
	return N_in * Pforward2 + W_in * P2D_p + E_in * P2D_m + S_in * P1D;
}
double Calculate_Energy_W2(double N_in, double S_in, double W_in, double E_in)
{
	return E_in * Pforward2 + N_in * P2D_m + S_in * P2D_p + W_in * P1D;
}
double Calculate_Energy_E2(double N_in, double S_in, double W_in, double E_in)
{
	return W_in * Pforward2 + N_in * P2D_p + S_in * P2D_m + E_in * P1D;
}
double Calculate_Energy_Vertical2(double N_in, double S_in, double W_in, double E_in)
{
	return (N_in + S_in + W_in + E_in) * Prad;
}
double Calculate_Energy_Internal2(double N_in, double S_in, double W_in, double E_in)
{
	return (N_in + S_in + W_in + E_in) * Pi2;
}
void Initialize()
{

	N_in = 1;
	S_in = 1;
	W_in = 1;
	E_in = 1;

	alpha_flag = 0.0;
	alpha_parameter = Krad;
	P = 1 - exp(-1);
	K1D = Transfer(K1D);
	K2D_p = Transfer(K2D_p);
	K2D_m = Transfer(K2D_m);
	Krad = Transfer(Krad);
	Ki2 = Transfer(Ki + extra_internal);
	Ki = Transfer(Ki);
	Pi = Calculate_Percent(Ki);
	Pi2 = Calculate_Percent(Ki2);
	P1D = Calculate_Percent(K1D);
	P2D_p = Calculate_Percent(K2D_p);
	P2D_m = Calculate_Percent(K2D_m);
	Prad = Calculate_Percent(Krad);
	Pforward = 1.0 - (P1D + P2D_m + P2D_p + Prad);
	Pforward2 = 1.0 - (P1D + P2D_m + P2D_p + Prad);
	cout << "Pf = " << Pforward << endl;
	cout << "Pf2 = " << Pforward2 << endl;
	cout << "P1D = " << P1D << endl;
	cout << "P2D_p = " << P2D_p << endl;
	cout << "P2D_m = " << P2D_m << endl;
	cout << "Prad = " << Prad << endl;
	cout << "Pi = " << Pi << endl;
	cout << "Pi2 = " << Pi2 << endl;
}
#endif
```

Constants Header

```
#pragma once

#ifndef CONSTANTS_H
#define CONSTANTS_H
#include <stdio.h>
#include <math.h>
#include <string.h>
#include <stdlib.h>
#include <iostream>
#include <fstream>
#include <iomanip>
#include <vector>
#include <map>
#include <ctime>
#include <atlstr.h>
using namespace std;
const int MAX_PC_SIZE = 8000000;
const int PC_COLS = 15;
double PC_NOW[MAX_PC_SIZE][PC_COLS] = { 0 }; // Power state for current time-step
double PC_PRE[MAX_PC_SIZE][PC_COLS] = { 0 }; // Power state for previous time-step

double Period = 1.0; // You should set it based on your system
double Energy = 0.0;
double P = 0.0;
double K1D = 0.0, K2D_p = 0.0, K2D_m = 0.0, Krad = 0.0, Ki = 0.0, Ki2 = 0.0;
double refl = 1.0; // Reflection coefficient (set 1.0 if perfect reflection)
float chargerate = 1.0; // 1.0 means 100% charging
int fixed_area = 0;
double extra_internal = 0.0;
double MK1D, MK2D = 0;
int PC_Total;
int Order;
int timestep;

double N_in;
double S_in;
double W_in;
double E_in;
double N_out = 0, S_out = 0, W_out = 0, E_out = 0;
double Vertical_out = 0, Internal_out = 0;
double Total_Period, P1D, P2D_p, P2D_m, Prad, Pi, Pforward, Pforward2, Pi2;
double alpha_para, alpha_int ,alpha_flag, alpha_parameter;
double mode_data[490000];
#endif
```

Markov Chain Header

```
#pragma once
#ifndef MARKOV CHAIN_H
#define MARKOV CHAIN_H
#include "constants.h"
#include "basic functions.h"

ofstream fout;
ofstream val;
//Quarter PC array_Shape of PC array_Shape of contact
void Q_S_C(int ord, int ts, int fa) //contact size - timestep - unpumped width
{
	cout << "Q_S_C function called with contact: " << ord << ", timestep: " << ts
<< ", W: " << fa << endl;
```

```
	int size_cont = ord;
	int rad = ord / 2;
	ord = ord + fa * 2; // size + W

	bool Even_odd = ord % 2;   //Judge the order number is Even or Odd
	int TimeStep, PC_Counter, LINE = 0;
	Order = ord / 2; //quarter - size + W
	PC_Total = Order * Order;
	PC_Counter = PC_Total;
	double Output_Total = 0;
	double Ver_Total = 0;
	double Int_Total = 0;

	memset(PC_NOW, 0, sizeof(PC_NOW));
	memset(PC_PRE, 0, sizeof(PC_PRE));
	bool TimeOut = true;

	/* timestep loop  */
	for (TimeStep = 0; (TimeOut); TimeStep++)
	{

		for (PC_Counter = 0; (PC_Counter < PC_Total); PC_Counter++)
		{
			double loss = 0;
			double hold = 0;
			double dis_to_centre = 0;

			PC_NOW[PC_Counter][0] = TimeStep;
			PC_NOW[PC_Counter][1] = PC_Counter;

			dis_to_centre = sqrt((Order - 1 - PC_Counter / Order) * (Order -
1 - PC_Counter / Order) + (Order - 1 - PC_Counter % Order) * (Order - 1 - PC_Counter %
Order));//distance to centre
			bool dir[] = { 1, 1, 1, 1 ,1 ,1, 1 };   //N-S-W-E-in or out
contact-south loss-west loss identifiers
			/*locate the pc - on the edge of unpumped ring or not*/



		/* Locate the pc - if on edges*/
			if (PC_Counter / Order == 0)  // At the bottom line
			{
				dir[1] = 0;
			}
			if ((PC_Counter / Order) == (Order - 1))  //At the top line
			{
				dir[0] = 0;  //Mirror Method
			}
			if (PC_Counter % Order == 0)       //At the leftmost line
			{
				dir[2] = 0;
			}
			if ((PC_Counter % Order) == (Order - 1))  //At the rightmost line
			{
				dir[3] = 0;  //Mirror Method
			}

			/*locate the pc - inside or outside of contact*/
			if (dis_to_centre <= (Order))
			{
				dir[4] = 0;//inside
			}
```

```
                        /*locate the pc - if having south & west loss*/

                        if (dir[1] == 0)
                        {
                                dir[5] = 0;
                        }
                        if (dir[2] == 0)
                        {
                                dir[6] = 0;
                        }
                        //update input data

                        if (dir[0] == 0)
                        {
                                PC_NOW[PC_Counter][2] = PC_PRE[PC_Counter][6];    //Nin =
Nout (Mirror)
                        }
                        else
                        {
                                PC_NOW[PC_Counter][2] = PC_PRE[PC_Counter + Order][7];
//Nin = Nout (Mirror)
                        }
                        if (dir[1] == 0)
                        {
                                PC_NOW[PC_Counter][3] = PC_PRE[PC_Counter][7] * refl;
                        }
                        else
                        {
                                PC_NOW[PC_Counter][3] = PC_PRE[PC_Counter - Order][6];
                        }
                        if (dir[2] == 0)
                        {
                                PC_NOW[PC_Counter][4] = PC_PRE[PC_Counter][8] * refl;
                        }
                        else
                        {
                                PC_NOW[PC_Counter][4] = PC_PRE[PC_Counter - 1][9];
                        }
                        if (dir[3] == 0)
                        {
                                PC_NOW[PC_Counter][5] = PC_PRE[PC_Counter][9];    //Ein =
Eout (Mirror)
                        }
                        else
                        {
                                PC_NOW[PC_Counter][5] = PC_PRE[PC_Counter + 1][8];    //Ein
= Eout (Mirror)
                        }


                        /* caluculate in-plane energy transfer*/
                        /* charged area is inner and uncharged area is outer*/
                        /* function 1: charged area*/
                        /* function 2: cancel energy injection of uncharged area*/

                        if (dir[4] == 0)//charged
                        {
                                PC_NOW[PC_Counter][10] =
Calculate_Energy_Vertical(PC_NOW[PC_Counter][2], PC_NOW[PC_Counter][3],
PC_NOW[PC_Counter][4], PC_NOW[PC_Counter][5]);
```

```
                        PC_NOW[PC_Counter][6] =
Calculate_Energy_N(PC_NOW[PC_Counter][2], PC_NOW[PC_Counter][3],
PC_NOW[PC_Counter][4], PC_NOW[PC_Counter][5]) + 1;
                        PC_NOW[PC_Counter][7] =
Calculate_Energy_S(PC_NOW[PC_Counter][2], PC_NOW[PC_Counter][3],
PC_NOW[PC_Counter][4], PC_NOW[PC_Counter][5]) + 1;
                        PC_NOW[PC_Counter][8] =
Calculate_Energy_W(PC_NOW[PC_Counter][2], PC_NOW[PC_Counter][3],
PC_NOW[PC_Counter][4], PC_NOW[PC_Counter][5]) + 1;
                        PC_NOW[PC_Counter][9] =
Calculate_Energy_E(PC_NOW[PC_Counter][2], PC_NOW[PC_Counter][3],
PC_NOW[PC_Counter][4], PC_NOW[PC_Counter][5]) + 1;
                        PC_NOW[PC_Counter][11] =
Calculate_Energy_Internal(PC_NOW[PC_Counter][6], PC_NOW[PC_Counter][7],
PC_NOW[PC_Counter][8], PC_NOW[PC_Counter][9]);
                        PC_NOW[PC_Counter][6] =
remove_internal_loss(PC_NOW[PC_Counter][6]);
                        PC_NOW[PC_Counter][7] =
remove_internal_loss(PC_NOW[PC_Counter][7]);
                        PC_NOW[PC_Counter][8] =
remove_internal_loss(PC_NOW[PC_Counter][8]);
                        PC_NOW[PC_Counter][9] =
remove_internal_loss(PC_NOW[PC_Counter][9]);
                }
                else
                {
                        PC_NOW[PC_Counter][10] =
Calculate_Energy_Vertical(PC_NOW[PC_Counter][2], PC_NOW[PC_Counter][3],
PC_NOW[PC_Counter][4], PC_NOW[PC_Counter][5]);
                        PC_NOW[PC_Counter][6] =
Calculate_Energy_N2(PC_NOW[PC_Counter][2], PC_NOW[PC_Counter][3],
PC_NOW[PC_Counter][4], PC_NOW[PC_Counter][5]);
                        PC_NOW[PC_Counter][7] =
Calculate_Energy_S2(PC_NOW[PC_Counter][2], PC_NOW[PC_Counter][3],
PC_NOW[PC_Counter][4], PC_NOW[PC_Counter][5]);
                        PC_NOW[PC_Counter][8] =
Calculate_Energy_W2(PC_NOW[PC_Counter][2], PC_NOW[PC_Counter][3],
PC_NOW[PC_Counter][4], PC_NOW[PC_Counter][5]);
                        PC_NOW[PC_Counter][9] =
Calculate_Energy_E2(PC_NOW[PC_Counter][2], PC_NOW[PC_Counter][3],
PC_NOW[PC_Counter][4], PC_NOW[PC_Counter][5]);
                        PC_NOW[PC_Counter][11] =
Calculate_Energy_Internal2(PC_NOW[PC_Counter][6], PC_NOW[PC_Counter][7],
PC_NOW[PC_Counter][8], PC_NOW[PC_Counter][9]);
                        PC_NOW[PC_Counter][6] =
remove_internal_lossex(PC_NOW[PC_Counter][6]);
                        PC_NOW[PC_Counter][7] =
remove_internal_lossex(PC_NOW[PC_Counter][7]);
                        PC_NOW[PC_Counter][8] =
remove_internal_lossex(PC_NOW[PC_Counter][8]);
                        PC_NOW[PC_Counter][9] =
remove_internal_lossex(PC_NOW[PC_Counter][9]);
                }
                /* calculate in-plane loss here*/
                if (dir[5] == 0)//south loss
                {
                        loss = loss + PC_NOW[PC_Counter][7] * (1 - refl);
                }
                if (dir[6] == 0)//west loss
                {
                        loss = loss + PC_NOW[PC_Counter][8] * (1 - refl);
                }
```

```
                    Ver_Total = Ver_Total + PC_NOW[PC_Counter][10];  //Calculate
total vertical loss (x4)
                    Int_Total = Int_Total + PC_NOW[PC_Counter][11];  //Calculate
total internal loss (x4)
                    Output_Total = Output_Total + loss;  //Calculate total in-plane
loss (x4)
             }

             ///
////////////////////////////////////////////////////////////////////////////////
////////////////////////////////////////////////////////////////////////////////
//////////////////////////////////////////////////////
             /*loss record function*/
             if (TimeStep == ts)
             {
                    double z;
                    z = TimeStep;
                    fout << size_cont << "," << fa << ",";
                    alpha_para = alpha_parameter * Output_Total / Ver_Total;
                    alpha_int = alpha_parameter * Int_Total / Ver_Total;
                    fout << setprecision(12) << Ver_Total << "," << setprecision(12)
<< Int_Total << "," << setprecision(12) << Output_Total << "," << setprecision(12) <<
z << "," << setprecision(12) << alpha_para << "," << alpha_int << "," << "\r";//
                    cout << "a// = " << alpha_para << ", ai = " << alpha_int << ",
timestep = " << TimeStep << endl;
                    TimeOut = 0;

             }
             ///
////////////////////////////////////////////////////////////////////////////////
////////////////////////////////////////////////////////////////////////////////
////////////////////////////////////////////////////////////////////////////////
//////////////////////////////////////////////////////
             /*mode data record function
             if (TimeStep == ts)
             {
                    alpha_para = alpha_parameter * Output_Total / Ver_Total;
                    printf("%2.9f \n", alpha_para);
                    for (int j = 0, k = 0; j < Order; j++)
                    {
                           for (int i = 0; i < Order; i++, k++)
                           {
                                  fout << PC_NOW[k][10] << ",";
                           }
                           fout << "\n";
                    }
                    TimeOut = 0;

             }*/


             /* Prepare for timestep jump */
             for (PC_Counter = 0; PC_Counter < PC_Total; PC_Counter++)
             {
                    for (int i = 0; i < 15; i++)
                    {
                           PC_PRE[PC_Counter][i] = PC_NOW[PC_Counter][i];
                           PC_NOW[PC_Counter][i] = 0;
                    }

             }
```

```
	}
}

void Q_S_S(int ord, int ts, int fa) //contact size - timestep - unpumped width
{
	cout << "Q_S_S function called with contact: " << ord << ", timestep: " << ts
<< ", W: " << fa << endl;
	int size_cont = ord;
	ord = ord + fa * 2; // size + W

	bool Even_odd = ord % 2;   //Judge the order number is Even or Odd
	int TimeStep, PC_Counter, LINE = 0;
	Order = ord / 2; //quarter - size + W
	PC_Total = Order * Order;
	PC_Counter = PC_Total;
	double Output_Total = 0;
	double Ver_Total = 0;
	double Int_Total = 0;

	memset(PC_NOW, 0, sizeof(PC_NOW));
	memset(PC_PRE, 0, sizeof(PC_PRE));
	bool TimeOut = true;

	/* timestep loop  */
	for (TimeStep = 0; (TimeOut); TimeStep++)
	{
		for (PC_Counter = 0; (PC_Counter < PC_Total); PC_Counter++)
		{
			PC_NOW[PC_Counter][0] = TimeStep;
			PC_NOW[PC_Counter][1] = PC_Counter;

			bool dir[] = { 1, 1, 1, 1 ,1 ,1, 1 };   //N-S-W-E-in or out
contact-south loss-west loss identifiers
			/*locate the pc - on the edge of unpumped ring or not*/



		/* Locate the pc - if on edges*/
			if (PC_Counter / Order == 0)  // At the bottom line
			{
				dir[1] = 0;
			}
			if ((PC_Counter / Order) == (Order - 1))  //At the top line
			{
				dir[0] = 0;  //Mirror Method
			}
			if (PC_Counter % Order == 0)       //At the leftmost line
			{
				dir[2] = 0;
			}
			if ((PC_Counter % Order) == (Order - 1))  //At the rightmost line
			{
				dir[3] = 0;  //Mirror Method
			}

			/*locate the pc - inside or outside of contact*/
			if ((PC_Counter / Order) >= fa && (PC_Counter % Order) >= fa)
			{
				dir[4] = 0;//inside
			}
```

```
                        /*locate the pc - if having south & west loss*/

                        if (dir[1] == 0)
                        {
                                dir[5] = 0;
                        }
                        if (dir[2] == 0)
                        {
                                dir[6] = 0;
                        }

                        //update input data
                        if (dir[0] == 0)
                        {
                                PC_NOW[PC_Counter][2] = PC_PRE[PC_Counter][6];    //Nin =
Nout (Mirror)
                        }
                        else
                        {
                                PC_NOW[PC_Counter][2] = PC_PRE[PC_Counter + Order][7];
//Nin = Nout (Mirror)
                        }
                        if (dir[1] == 0)
                        {
                                PC_NOW[PC_Counter][3] = PC_PRE[PC_Counter][7] * refl;
                        }
                        else
                        {
                                PC_NOW[PC_Counter][3] = PC_PRE[PC_Counter - Order][6];
                        }
                        if (dir[2] == 0)
                        {
                                PC_NOW[PC_Counter][4] = PC_PRE[PC_Counter][8] * refl;
                        }
                        else
                        {
                                PC_NOW[PC_Counter][4] = PC_PRE[PC_Counter - 1][9];
                        }
                        if (dir[3] == 0)
                        {
                                PC_NOW[PC_Counter][5] = PC_PRE[PC_Counter][9];    //Ein =
Eout (Mirror)
                        }
                        else
                        {
                                PC_NOW[PC_Counter][5] = PC_PRE[PC_Counter + 1][8];    //Ein
= Eout (Mirror)
                        }


                        /* caluculate in-plane energy transfer*/
                        /* charged area is inner and uncharged area is outer*/
                        /* function 1: charged area*/
                        /* function 2: cancel energy injection of uncharged area*/

                        if (dir[4] == 0)//charged
                        {
                                PC_NOW[PC_Counter][10] =
Calculate_Energy_Vertical(PC_NOW[PC_Counter][2], PC_NOW[PC_Counter][3],
PC_NOW[PC_Counter][4], PC_NOW[PC_Counter][5]);
```

```
                        PC_NOW[PC_Counter][6] =
Calculate_Energy_N(PC_NOW[PC_Counter][2], PC_NOW[PC_Counter][3],
PC_NOW[PC_Counter][4], PC_NOW[PC_Counter][5]) + 1;
                        PC_NOW[PC_Counter][7] =
Calculate_Energy_S(PC_NOW[PC_Counter][2], PC_NOW[PC_Counter][3],
PC_NOW[PC_Counter][4], PC_NOW[PC_Counter][5]) + 1;
                        PC_NOW[PC_Counter][8] =
Calculate_Energy_W(PC_NOW[PC_Counter][2], PC_NOW[PC_Counter][3],
PC_NOW[PC_Counter][4], PC_NOW[PC_Counter][5]) + 1;
                        PC_NOW[PC_Counter][9] =
Calculate_Energy_E(PC_NOW[PC_Counter][2], PC_NOW[PC_Counter][3],
PC_NOW[PC_Counter][4], PC_NOW[PC_Counter][5]) + 1;
                        PC_NOW[PC_Counter][11] =
Calculate_Energy_Internal(PC_NOW[PC_Counter][6], PC_NOW[PC_Counter][7],
PC_NOW[PC_Counter][8], PC_NOW[PC_Counter][9]);
                        PC_NOW[PC_Counter][6] =
remove_internal_loss(PC_NOW[PC_Counter][6]);
                        PC_NOW[PC_Counter][7] =
remove_internal_loss(PC_NOW[PC_Counter][7]);
                        PC_NOW[PC_Counter][8] =
remove_internal_loss(PC_NOW[PC_Counter][8]);
                        PC_NOW[PC_Counter][9] =
remove_internal_loss(PC_NOW[PC_Counter][9]);
                }
                else
                {
                        PC_NOW[PC_Counter][10] =
Calculate_Energy_Vertical(PC_NOW[PC_Counter][2], PC_NOW[PC_Counter][3],
PC_NOW[PC_Counter][4], PC_NOW[PC_Counter][5]);
                        PC_NOW[PC_Counter][6] =
Calculate_Energy_N2(PC_NOW[PC_Counter][2], PC_NOW[PC_Counter][3],
PC_NOW[PC_Counter][4], PC_NOW[PC_Counter][5]);
                        PC_NOW[PC_Counter][7] =
Calculate_Energy_S2(PC_NOW[PC_Counter][2], PC_NOW[PC_Counter][3],
PC_NOW[PC_Counter][4], PC_NOW[PC_Counter][5]);
                        PC_NOW[PC_Counter][8] =
Calculate_Energy_W2(PC_NOW[PC_Counter][2], PC_NOW[PC_Counter][3],
PC_NOW[PC_Counter][4], PC_NOW[PC_Counter][5]);
                        PC_NOW[PC_Counter][9] =
Calculate_Energy_E2(PC_NOW[PC_Counter][2], PC_NOW[PC_Counter][3],
PC_NOW[PC_Counter][4], PC_NOW[PC_Counter][5]);
                        PC_NOW[PC_Counter][11] =
Calculate_Energy_Internal2(PC_NOW[PC_Counter][6], PC_NOW[PC_Counter][7],
PC_NOW[PC_Counter][8], PC_NOW[PC_Counter][9]);
                        PC_NOW[PC_Counter][6] =
remove_internal_lossex(PC_NOW[PC_Counter][6]);
                        PC_NOW[PC_Counter][7] =
remove_internal_lossex(PC_NOW[PC_Counter][7]);
                        PC_NOW[PC_Counter][8] =
remove_internal_lossex(PC_NOW[PC_Counter][8]);
                        PC_NOW[PC_Counter][9] =
remove_internal_lossex(PC_NOW[PC_Counter][9]);
                }

                /* calculate in-plane loss here*/
                if (dir[5] == 0)//south loss
                {
                        Output_Total = Output_Total + PC_NOW[PC_Counter][7] * (1 -
refl);
                }
                if (dir[6] == 0)//west loss
                {
```

```
                        Output_Total = Output_Total + PC_NOW[PC_Counter][8] * (1 -
refl);
                }

                Ver_Total = Ver_Total + PC_NOW[PC_Counter][10];  //Calculate
total vertical loss (x4)
                Int_Total = Int_Total + PC_NOW[PC_Counter][11];  //Calculate
total internal loss (x4)
        }

        ///
////////////////////////////////////////////////////////////////////////////////
////////////////////////////////////////////////////////////////////////////////
//////////////////////////////////////////////////////
        /*loss record function*/
        if (TimeStep == ts)
        {
                double z;
                z = TimeStep;
                fout << size_cont << "," << fa << ",";
                alpha_para = alpha_parameter * Output_Total / Ver_Total;
                alpha_int = alpha_parameter * Int_Total / Ver_Total;
                fout << setprecision(12) << Ver_Total << "," << setprecision(12)
<< Int_Total << "," << setprecision(12) << Output_Total << "," << setprecision(12) <<
z << "," << setprecision(12) << alpha_para << "," << alpha_int << "," << "\r";//
                cout << "a// = " << alpha_para << ", ai = " << alpha_int << ",
timestep = " << TimeStep << endl;
                TimeOut = 0;

        }
        ///
////////////////////////////////////////////////////////////////////////////////
////////////////////////////////////////////////////////////////////////////////
////////////////////////////////////////////////////////////////////////////////
//////////////////////////////////////////////////////
        /*mode data record function*/
        /*if (TimeStep == ts)
        {
                alpha_para = alpha_parameter * Output_Total / Ver_Total;
                printf("%2.9f \n", alpha_para);
                for (int j = 0, k = 0; j < Order; j++)
                {
                        for (int i = 0; i < Order; i++, k++)
                        {
                                fout << PC_NOW[k][10] << ",";
                        }
                        fout << "\n";
                }
                TimeOut = 0;

        }*/


        /* Prepare for timestep jump */
        for (PC_Counter = 0; PC_Counter < PC_Total; PC_Counter++)
        {
                for (int i = 0; i < 15; i++)
                {
                        PC_PRE[PC_Counter][i] = PC_NOW[PC_Counter][i];
                        PC_NOW[PC_Counter][i] = 0;
                }
```

```
                }
        }
}
```